# Corrosion Resistance and Formability of Ultra-thin Plasma Polymer Films on Galvanised Steel

Dissertation

Zur Erlangung des akademischen Grades eines
Doktors der Naturwissenschaften (Dr. rer. nat.)
der Fakultät für Naturwissenschaften der
Universität Paderborn

vorgelegt im Juni 2009 von

Dipl.-Phys. Tobias Titz

Die vorliegende Arbeit wurde angefertigt am
Max-Planck Institut für Eisenforschung GmbH
in Düsseldorf

Referent: Prof. Dr.-Ing. G. Grundmeier
Department Chemie
Fachgebiet für Technische und Makromolekulare Chemie
der Universität Paderborn

Korreferent: Prof. Dr. C. Schmidt
Department Chemie
Fachgebiet für Physikalische Chemie und Makromolekulare Chemie
der Universität Paderborn

´

Tag der mündlichen Prüfung: 2. Juli 2009

# Danksagung – Acknowledgement

Die vorliegende Arbeit wurde während meiner Tätigkeit als wissenschaftlicher Angestellter der Max-Planck-Institut für Eisenforschung GmbH in Düsseldorf angefertigt.
An erster Stelle möchte ich mich bei meinem Doktorvater Herrn Prof. Dr.-Ing. G. Grundmeier sehr herzlich bedanken für die Vergabe meines jederzeit spannenden Themas, für die intensive und konstruktive Betreuung meiner Arbeit und die Möglichkeit, meine wissenschaftlichen Ergebnisse auf verschiedenen Konferenzen und Tagungen zu präsentieren.
Frau Prof. Dr. C. Schmidt danke ich sehr herzlich für die freundliche Übernahme des Koreferats.
Herrn Prof. Dr. M. Stratmann gilt mein Dank für die Möglichkeit der Durchführung meiner experimentellen Arbeiten am MPIE in der Abteilung Grenzflächen und Oberflächentechnik. Allen Mitarbeitern der Abteilung danke ich sehr herzlich für die angenehme Atmosphäre und die stete Hilfsbereitschaft bei allen Anliegen.
Der Firma OCAS danke ich für die Bereitstellung der finanziellen Mittel sowie Herrn Dr. F. Hörzenberger und Frau K. Van den Bergh für die zahlreichen und anregenden Diskussionen während der Projekttreffen.
Ein ganz ganz herzliches Dankeschön geht an Fr. P. Ebbinghaus, Dr. N. Fink, Dr. M. Giza, Dr. P. Keil, G. Klimow, Dr. I. Klüppel, Ö. Ozcan, R. Posner, Dr. J. Raacke, M. Santa, Dr. M. Valtiner, R. Vlasak und Dr. K. Wapner und vielen anderen, die meine Zeit am MPIE mit interessanten Messungen und Diskussionen sowie zahlreichen Anekdoten einfach unvergesslich gemacht haben.

Mein besonderer Dank gilt meiner gesamten Familie sowie allen Freunden für ihr Verständnis und ihre tatkräftig Unterstützung.
Bei meiner geliebten Frau Jolante werde ich mich niemals genug für ihr Verständnis, ihre Unterstützung und ihre unermüdliche Geduld bedanken können. Unserem Sonnschein Sophie Amelie danke ich vor allem für ihr bezauberndes Gemüt, das sonnige Lächeln und vor allem für ihren gesunden Schlaf während des Schreibens meiner Dissertation.

# Index

# Symbols and abbreviations

Latin symbols

| | |
|---|---|
| a | edge size of hexagonal cell |
| $a_{Zn^+}$ | $Zn^+$ activity |
| A | surface area |
| $A_0$ | initial sample cross-sectional area |
| c | height of hexagonal cell |
| C | capacitance |
| $C_C$ | coating capacitance |
| $C_{DL}$ | double layer capacitance |
| CE | counter electrode |
| d | film thickness |
| D | spring constant |
| E | applied voltage |
| $E_{corr}$ | electrode potential |
| $E_g$ | band gap |
| f | frequency |
| F | Faraday constant |
| $F_{ext}$ | external force |
| I | applied current |
| $I_{AC}$ | alternating current |
| l | final gauge length |
| $l_0$ | initial gauge length |
| P | applied load |
| R | universal gas constant |

| | |
|---|---|
| $R_C$ | ohmic resistor |
| $R_{Ct}$ | pore resistance |
| $R_e$ | elastic limit |
| $R_{ohm}$ | ohmic resistance |
| $R_M$ | ultimate tensile strength |
| $R_U$ | uncompensated electrolyte resistance |
| RE | reference electrode |
| $U_{ext}$ | applied external voltage |
| $W_{Ref}$ | work function of reference metal |
| WE | working electrode |
| Z | complex impedance |

Greek symbols

| | |
|---|---|
| $\varepsilon_0$ | dielectric vacuum constant |
| $\varepsilon_{½}$ | half-cell potential of reference metal |
| $\varepsilon_r$ | dielectric material constant |
| $\varepsilon_t$ | technical deformation |
| $\theta$ | phase |
| $\mu_e$ | chemical potential |
| $\sigma$ | true stress |
| $\varphi_i$ | forming degree (i=1, 2, 3) |
| $\chi_{El}$ | surface dipole potential of electrolyte |
| $\chi_{Pol}$ | surface dipole potential of polymer surface |
| $\omega$ | radial frequency |
| $\Delta$ | phase difference |
| $\Delta l$ | elongation |
| $\Delta\Phi$ | Galvani potential difference |
| $\Delta\Phi_D$ | Galvani potential difference (Donnan potential) |
| $\Delta\Psi$ | Volta potential difference |
| $\Theta_{film}$ | film surface area |
| $\Psi$ | amplitude ratio |

Abbreviations

| | |
|---|---|
| AFM | atomic force microscopy |
| AES | scanning Auger electron spectroscopy |
| CV | cyclic voltammetry |
| EBSD | electron backscattered diffraction |
| EIS | electrochemical impedance spectroscopy |
| FT-IRRAS | Fourier transformed infrared reflection absorption spectroscopy |
| hcp | hexagonal closed-packed |
| HDG | hot-dip galvanised steel |
| HMDSO | hexamethyldisiloxane |
| HR-SKP | height-regulated scanning Kelvin probe |
| MCT | mercury cadmium telluride |
| PE-CVD | plasma enhanced chemical vapour deposition |
| PET | polyethylene terephthalate |
| SE | spectroscopic ellipsometry |
| SEM | scanning electron microscopy |
| SHE | standard hydrogen electrode |
| SKP | scanning Kelvin probe |
| SKP-FM | scanning Kelvin probe force microscopy |
| TEOS | tetramethoxysilane |
| THF | Tetrahydrofuran |
| XPS | x-ray photoelectron spectroscopy |

# 1 State of research and motivation

Corrosion resistant polymer/zinc interfaces are of high importance for organically coated or adhesively bonded galvanised steel substrates [1-4]. Moreover, zinc oxides are applied in the construction of photovoltaic cells and also in this case have to be protected by thin films [5, 6]. Plasma technology has become an interesting and environmentally friendly dry process at atmospheric or reduced pressures to modify oxides and oxide covered metal surfaces [7-9].

In the past, several studies concerning the corrosion resistance of metal substrates covered with thin plasma polymer films were carried out [10-13]. However, the mechanism of corrosion protection of organically coated plasma modified surfaces is still poorly understood.

Grundmeier et al. showed that a plasma oxidation of iron oxide films on iron leads to a change in their electronic properties [14]. However, the highly oxidised state of the passive film was not stable and changed again in humid atmospheres to the state which is determined by the oxygen reduction kinetics at the outer oxide surface. This process is also determined by the kinetics of the metal dissolution into the passive film at the metal/oxide interface.

Barranco et al. showed that for cathodically deposited plasma polymer films the interfacial electrode potential on iron could be effectively shifted cathodically which indicate a strong inhibition of interfacial oxygen reduction kinetics [15]. However, a reductive plasma treatment had to be followed by a sufficiently thick plasma polymer film deposition to prevent the plasma polymer/metal interface from re-oxidation. Based on this work electrochemical methods could be established for an improved understanding of how plasma modifications influence the corrosion mechanism of thin film coated metals.

From the viewpoint of thin film engineering, it is the aim to achieve functional properties at extremely low thickness values. With regard to interfacial corrosive de-adhesion of polymer coated zinc and iron substrates, the interfacial oxygen reduction kinetics should be strongly inhibited by the respective plasma polymer film [15].

Forming of corrosion protected metal sheets is one of the most important applications in many industries for economic reasons. The formation of forming induced defects is not only limited on defects in the protective inorganic [16-19] or organic [20] layers but also on substrate defects [21-24]. The formation of defects in brittle films on ductile substrates has been intensively studied both experimentally and theoretically [17, 25]. Usually multiple sequential crack formation is observed for more or less brittle films on ductile or high elongation substrates. By increasing the strain the number of cracks increases as well. This observation is explained by the so-called shear lag approximation presented in detail by Wojciechowski and Mendolia [16, 17].

Depending on the applied stress and strain different defect mechanism can be observed on pure zinc coated steel sheets [21-23]. Slip, twinning and cracking are the major deformation modes on zinc grains depending on the applied stress. Due to the hcp structure of zinc, basal slip is the easiest deformation mode in zinc and is therefore the predominant defect mode [26-28]. Twinning can be found on zinc grains if compressive and tension stress is applied simultaneously [21].

As it is well known from literature ceramic films can only be formed for less than 1% elongation. Plasma polymer films are intended to follow the deformation of the substrate due to their high cross-linking during plasma deposition [9-11, 29]. B. Baumert et al. showed that plasma polymer films on steel show substrate induced defects for high forming degrees [24].

The aim of the present work is to investigate the corrosion protection of ultra-thin barrier plasma polymer films on a complex alloy surface. Therefore, the investigation focuses on hot-dip galvanised steel substrates with an aluminium zinc alloy coating.

Low-pressure plasma polymerization coatings are used as they are formed by an economically advantageous dry process which uses a minimum amount of energy and substances compared to wet chemical corrosion protection coatings.

This work focuses especially on the understanding of the corrosion protection, film thickness dependence and the influence of the formability of these ultra-thin plasma polymer films.

The correlation of nanoscopic defect structures and macroscopic performance of the corrosion protective system should be evaluated by electrochemical analysis and corrosion studies of the organically coated composites in humid and corrosive environments.

# 2 Fundamentals

## 2.1 Corrosion and corrosion protection of galvanised steel

Zinc and zinc alloy coatings on steel are some of the commercially most used methods to protect steel components which are exposed to corrosive environments. The use of galvanisation techniques like hot-dip galvanising to deposit protective zinc coatings are well established since centuries [30].

Zinc coatings protect the underlying steel in several ways. As a barrier layer, the zinc coating separates the steel from the corrosive environment. Zinc itself acts as a sacrificial anode to galvanically protect the underlying steel at defects, scratches and cut edges of the zinc coating [30-32].

However, because of new requirements of the industry, additional protective coatings are necessary to increase the corrosion protection. Besides the conventional surface treatments for reactive metals like wet chemical phosphatisation, atmospheric and vacuum plasma deposition of inorganic coatings offer an environmentally friendly alternative [8-10, 12, 13, 24, 33-35].

### 2.1.1 Degradation of organically coated zinc substrates

For intact organic coatings the metal surface is effectively protected against corrosion. If a polymer/metal composite is exposed to environments with high water activites, the interfacial adhesion force between the metal surface and the organic coating is lowered. This happens because of the strongly negative Gibbs energy of the adsorption of water molecules on the oxide or hydroxide covered metallic surface according to

$$H_2O_{(g)} + Me_xO_yOH_z \rightarrow H_2O_{(aq)} \cdots Me_xO_yOH_z \quad (1)$$

In any case water molecules are able to penetrate through the polymer to the interface and adsorb at the polymer/oxide interface. Here, the water molecules adsorb immediately at free adsorption sites and lead to a displacement of physisorbed organic functionalities. In most cases the adhesion forces of the molecules are still high enough that the coating adheres. A very detailed description of the adhesion and de-adhesion mechanisms at polymer/metal interfaces is published in the review by Grundmeier and Stratmann [36].

The de-adhesion of the polymer from the metallic or inorganic substrate can be described by the picture of breaking bonds at the interface. This can occur by chemical displacement reactions (e.g. physisorbed water molecules), by mechanical force or by chemical reactions which alter the chemical bonds at the interface. Organically coated metals like iron or zinc degrade at the interface by the oxygen reduction process [37-40]. During oxygen reduction a strong alkaline electrolyte is formed which can stabilise or destabilise the metal oxide. The delamination of the organic coating originates only from the bond breaking within the organic coating interface. Intermediate radicals such as $H_2O^-$, $OH$ and $O_2^-$ are formed during oxygen reduction and participate in the degradation of the organic coating. Wroblowa [39] proposed an initial step of the reaction mechanism for the oxidative degradation of the polymer as follows

$$O_2^- + R-H \rightarrow R^\bullet + H_2O^- \tag{2}$$

with the subsequent reactions:

$$R^\bullet + O_2 \rightarrow ROO^\bullet \tag{3}$$

$$ROO^\bullet + R-H \rightarrow ROOH + R^\bullet \tag{4}$$

Additionally to the chemical reaction of the oxygen reduction products the change of the pH at the interface due to fact that zinc oxide is not stable in alkaline environments can contribute to the delamination process [41].

If a defect occurs in the polymer coating and ions and water molecules can directly access the bare zinc or iron surface electrochemical reactions will take place at the metal electrolyte interface. Due to these reactions delamination of the organic polymer coating will occur and the intact substrate/polymer interface will be replaced by two new interfaces substrate/electrolyte and electrolyte/polymer. The electrochemical reactions will therefore expand from the defect below the organic coating and the change in the electrochemical reactivity of this interface will be rejected in a local change of the free electrode potential as it

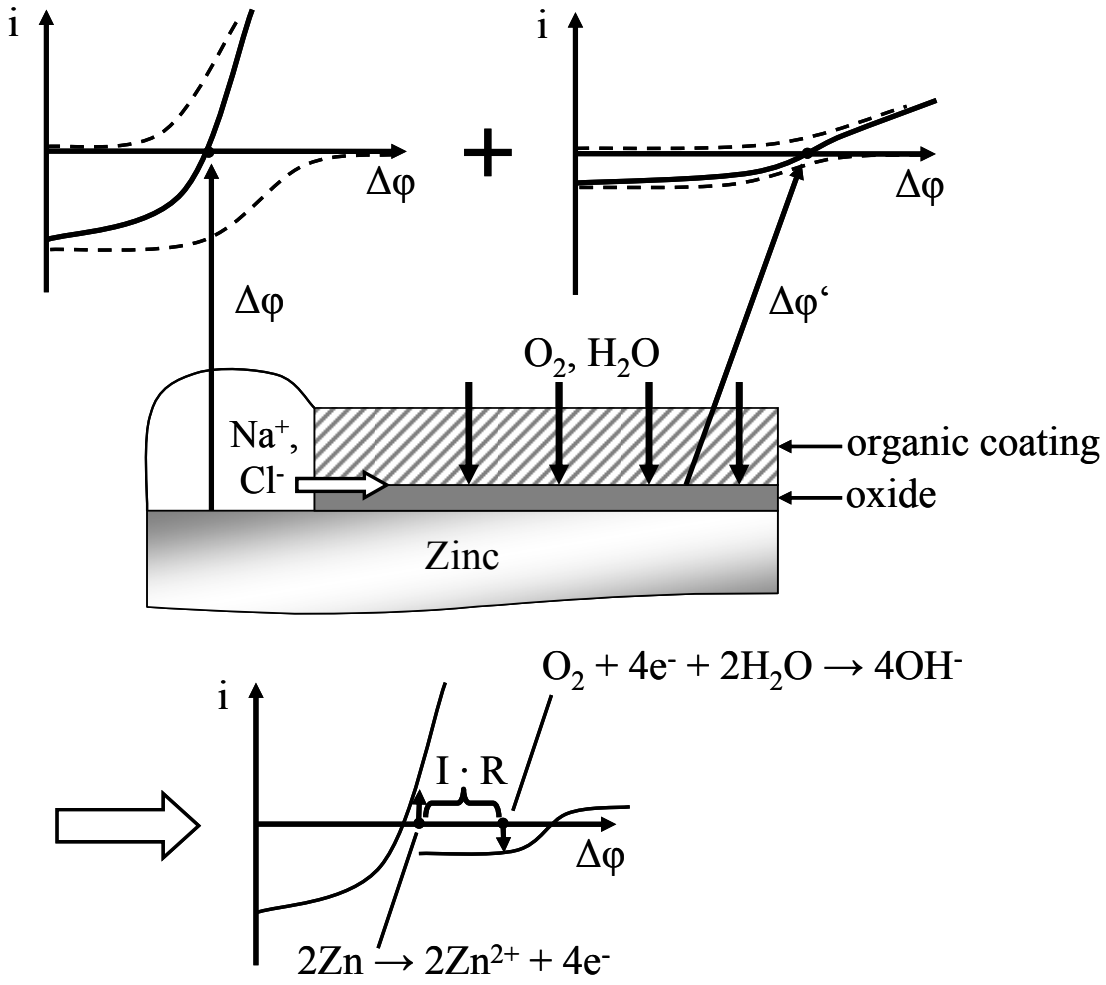


*Figure 1: Principle schematic of the corrosion model explaining the formation of a galvanic element on zinc. Central picture: cross-section with defect filled with electrolyte ($Na^+$ ,$Cl^-$ ions) and an intact oxide/organic coating interface. Polarization curves at the defect, the intact interface and the result after galvanic coupling of both elements for zinc (in accordance to [40]).*

is shown in Figure 1. The resulting principle schematic of the corrosion model is comprehensively summarized by Fürbeth et al. for galvanised steel and for steel by Leng et al. [40, 41].

Due to the metallic substrate, a galvanic element can be formed between the defect with the electrolyte and the intact interface of the polymer coating and the zinc surface. Zinc dissolution occurs at the defect area when the metal is in contact with the electrolyte. At the intact interface oxygen reduction of molecular oxygen in the presence of water molecules occur. The rate of the metal dissolution is limited as the same amount of electrons has to be provided by the oxygen reduction at the intact interface. Within this galvanic element cations

have to be transported from the local anode (defect) to the local cathode (delaminated area). If the oxygen reduction is reduced by a barrier layer in top of the zinc oxide, the metal dissolution and also the delamination is effectively inhibited.

### 2.1.2 Corrosion protection of zinc by thin plasma polymer films

Plasma polymerisation, as a process technology for corrosion resistant thin film deposition has been explored during the last 20 years [7, 42]. Recent studies reveal the good corrosion protection properties of organosilicon based plasma polymers on steel substrates and the crucial influence of the pre-treatment process on the stability of the resulting interface [13, 34]. The pre-treatments for trimethylsilane based films consist of an oxidative step ($O_2$-plasma) to remove organic contaminations from the substrate and a second reductive step ($Ar/H_2$-plasma) to remove the metal oxide layer. While the successive application of both steps provides the best corrosion protection of various plasma treatments for steel in combination with a cathodic electrocoat, little is known about the chemical structure of the interface. Yasuda and van Ooij in particular have shown that the deposition of plasma polymers on steel and galvanised steel might even substitute the chromatation process [13, 34, 43, 44].

Very little knowledge is gained about the corrosion protection of these coatings when stress is applied on the coated steel substrates. Most studies focus on the formation of defects in the plasma polymer coating during forming, but no structure-relation between corrosion protection and crack formation was studied in detail [24, 45].

### 2.1.3 The Kelvin probe – a unique tool for in-situ corrosion studies

The Kelvin probe (KP) is a unique tool for corrosion studies and can be used in vacuum, corrosive environments like electrolytes and high humidity and also in combination with atomic force microscopy [40, 41, 46-48]. Stratmann et al. studied polymer coated metals on iron and zinc as the Kelvin probe can measure the Volta potential at the buried interface between the coating and the metal surface [36, 40, 41, 46, 47]. The principle measurement set-up is shown in Figure 2. If two metals are brought into contact, the Fermi level of both equalizes. In case of differing work functions of both metals, charging of one material in respect to the other materials occurs. By using a capacitor and a vibrating needle as shown in the schematic, the charge transfer can be measured as the formed capacitor (needle surface to metal surface) is loaded and unloaded periodically.

By applying an external voltage to the capacitor, the charge transfer can be zeroed. In this case, the applied external voltage is identical to the Volta potential difference between the two metals. The Volta potential difference directly correlates with the Fermi level difference. If one Fermi level is known or the value can be calibrated, than the missing Fermi level of the unknown material can be calculated.

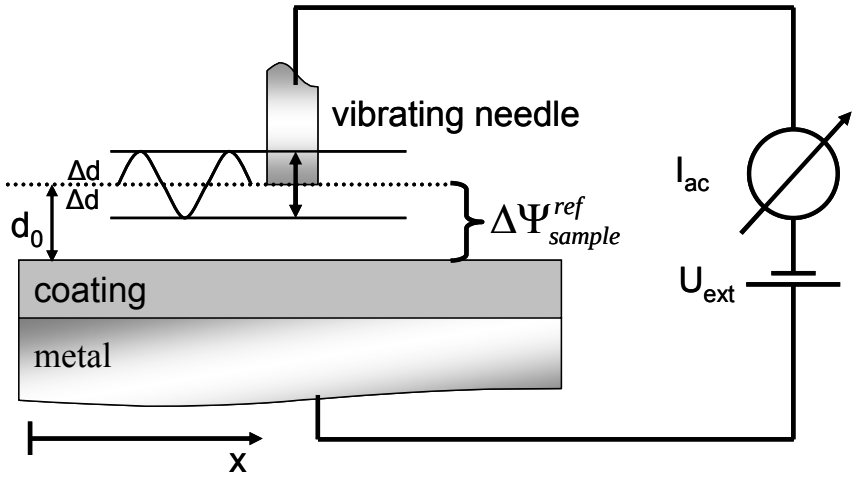


*Figure 2: Schematic of the measurements of electrochemical potentials at buried interfaces with the Kelvin probe*

The article from Grundmeier and Stratmann summarizes the theoretical basis of the Kelvin probe [36]. The work function of a metal is defined as the work to remove an electron from the metal to a point far away from the surface. Under high vacuum conditions with clean surfaces the work function of the metals is well defined.

If the metal is covered with aqueous electrolytes or organic polymers, additional interfaces have to be passed and the measured Volta potential difference is changed by the additional potential differences across the interfaces. The identical behaviour can be found for the electrode potential which is determined by the potential difference across the electrified interface. Therefore, a simple relation exists between the Volta potential difference $\Delta\Psi_{Pol}^{Ref}$ and the electrode potential $E_{Corr}$ of the buried interface. For liquid phases covering one metal surface, the following expression can be used

$$E_{Corr} = \left\{ \frac{W_{Ref}}{F} - \chi_{El} - \varepsilon_{1/2}^{Ref} \right\} + \Delta\Psi_{Pol}^{Ref} \tag{5}$$

where F is the Faraday constant, $W_{Ref}$ the work function of the reference metal, $\chi_{El}$ the surface dipole potential of the electrolyte and $\varepsilon_{1/2}^{Ref}$ is the half-cell potential of the reference metal. If less oriented polymers with small dipole moments are used, a similar expression can be used

$$E_{Corr} = \left\{ \frac{W_{Ref}}{F} - \chi_{Pol} - \varepsilon_{1/2}^{Ref} \right\} + \Delta\Psi_{Pol}^{Ref} \tag{6}$$

with the surface dipole $\chi_{Pol}$ of the polymer surface. In this case, the Kelvin probe monitors the buried interface without touching the surface. For reactive metals, the metal/electrolyte interface is not stable. However, the metal surface is covered by a thin native oxide layer. Therefore, the Volta potential difference must be expressed by the sum of the potential differences over all interfaces:

$$\Delta\Psi_{Pol}^{Ref} = \Delta\Phi_{Ox}^{Ref} + \Delta\Phi_{Ox} + \Delta\Phi_{Pol}^{Ox} - \frac{1}{F}\mu_e^{Me} - \frac{W_{Ref}}{F} + \chi_{Pol} \tag{7}$$

whereas $\Delta\Phi$ is the respective Galvani potential difference and $\mu_e$ is the chemical potential of the electron in the metal. By replacing the Galvani potential across the oxide layer by the corresponding change in chemical composition, then the Volta potential difference represents

the oxidation level within the oxide at the metal/polymer interface, as e.g. for an oxide covered iron interface:

$$\Delta\Psi_{Pol}^{Ref} = -\frac{\Delta\mu^{0}_{Fe^{3+}/Fe^{2+}}}{F} + \Delta\Phi_{Pol}^{Ox} - \frac{W_{Ref}}{F} + \chi_{Pol} + \frac{RT}{F}\ln\left[\frac{Fe^{3+}}{Fe^{2+}}\right] \tag{8}$$

During de-adhesion an additional liquid phase is formed between the substrate and the organic phase. Then the metal/electrolyte interface can be treated as a conventional electrochemical interface but with an additional Galvani Potential difference $\Delta\Phi_D$ (Donnan potential):

$$E_{Corr} = \frac{W_{Ref}}{F} - \chi_{Pol} - \varepsilon_{1/2}^{Ref} + \Delta\Phi_D + \Delta\Psi_{Pol}^{Ref} \tag{9}$$

Therefore, the Volta potential difference allows the measurement of the corrosion potential at the buried interface between metal and polymer only if the Donnan potential is know or small. Simple lacquers for corrosion protection have only some fixed ionic groups and as their concentration is very small, the Donnan potential can be neglected.

## 2.2 Cold plasmas

### 2.2.1 Plasma modification of metal surfaces

Plasma processing is well known in industry and science as many applications like film deposition, etching or surface modifications use a quasi neutral gas to modify surfaces [8, 42]. The physical properties of plasmas are mainly influenced by the amount of free charge carriers, free electrons and ionized atoms or molecules. As conventional plasmas are macroscopically quasi neutral by comparing the amount of positive and negative charge carriers, the movement of the charge carrier is limited due to Coulomb forces.

Different types of plasmas can be distinguished, isothermal and low temperature (cold) plasmas. In the case of the cold plasmas, the temperature of the electrons and therefore their kinetic energy is much higher than the temperature of the positive charge carriers. In this case the ionisation of the plasma occurs due to free electrons with high energy which are powered by an external energy field. Low temperature plasmas have the advantage that the substrate material is only moderately heated during plasma interaction in comparison to isothermal plasmas with high ion energies of the activated plasma species.

Nevertheless the formation and modifications of thin oxide films by low temperature plasmas is used by several groups to tailor the surface reactivity of metal oxides. Grundmeier et al. have studied e.g. the modification of native oxide films on iron and zinc by oxidizing and reducing plasmas to adjust the surface chemistry [14, 15, 49]. The consequences of low temperature plasma modification of zinc oxide surfaces based on the work of Grundmeier et al. will be discussed in detail in chapter 5.1.3.

### 2.2.2 Plasma polymerization of organosilanes

The plasma polymerization of organosilane precursors under various conditions is a topic that has received a great deal of attention by many researchers in recent years and has been extensively reported in various literatures. A first summarizing article about plasma polymerizations in glow discharges was published by Yasuda in 1981 summarizing the work of different authors, which have described plasma polymer films as by-products of phenomena associated with electric discharge in the early 20th century. By recognition of various advantages of plasma polymer films more and more work was focused on the deposition and characterization of these films. However many authors, especially those trying to deposit $SiO_2$ like films, didn't classify the plasma polymerised siloxane films as organically modified ceramics despite the presence of carbon and hydrogen.

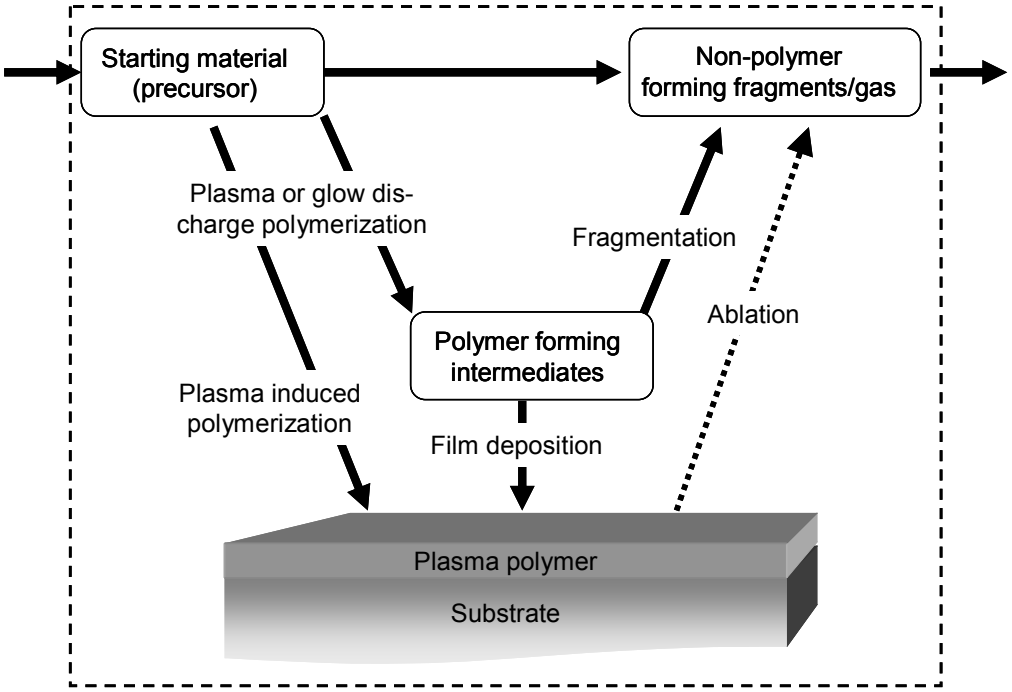


*Figure 3: Schematic representation of the plasma polymerization mechanism according to Yasuda [8].*

The plasma deposition processes can be separated into two classes, direct and remote plasma deposition by using different power supplies and experimental set-ups. When an organosilane precursor is introduced into the plasma zone, it is ionized and fragmented by high-energy electrons and ions inside the plasma. At low pressure and therefore a long mean free path, ionized molecular fragments and ions are more likely to collide with the chamber walls then with other gas phase species and hence adsorb and react on surfaces within the reactor to grow thin films of similar chemical composition and structure in comparison with the injected precursor monomer. The schematic film forming processes are shown in Figure 3.

This plasma polymerization process has been used to deposit hybrid films from a variety of organosilane precursors with applications ranging from corrosion protection [50-52], biomedical films for implants [53], barrier coatings for packaging [54-56] to dielectric layers in integrated electronic circuits [57].

For the deposition of organically modified ceramics, the most popular precursors are hexamethyldisiloxane (HMDSO, see Figure 4) and tetramethoxysilane (TEOS) often in combination with oxygen and/or a variety of dopants. The chemical and physical properties of the resulting films depend strongly on the process parameters, such as the way of coupling the power into the gas, injection of the precursor and the amount of oxidants.

Coatings produced from siloxane-based precursors have the general composition Si$O_xC_yH_z$ where $x \leq 2$ and $y$ and $z$ can vary up to the stoichiometry of the used precursor.

The chemistry of the siloxane plasma process is complicated by the wide variety of compounds formed by both carbon and silicon. However, some general observations can be made.

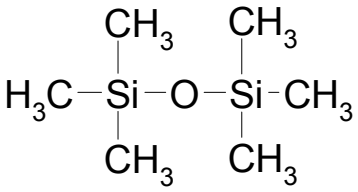

*Figure 4: Chemical structure of HMDSO.*

Plasma polymers are generally characterized by an extremely tight and three-dimensional network. At relatively low discharge power and without addition of oxygen the deposited films generally have a similar elemental composition as the precursor. Frascassi et al. showed for higher discharge power that the concentration specific molecular groups (e.g. C-H, C-O) and the functionality of is different while the elemental composition is still identical to that of the precursor [58].

Several studies compared the film composition to process parameters and precursors [13, 59-63]. The addition of oxygen to the siloxane plasma to deposit $SiO_x$-like films further complicates the plasma chemistry and has been also observed in films even when no gaseous oxygen was directly added to the plasma. Many authors have attributed the oxygen to irremovable water molecules which are adsorbed on the surface of the chamber and the substrate surface. However, the hydroscopic nature of the precursor itself can be the source for oxygen which is incorporated in the deposited film.

Molecular oxygen in the plasma zone is readily fragmented by the plasma state and forms highly reactive atomic oxygen and ozone which react with the siloxane precursor. At low oxygen concentrations, the atomic oxygen highly increases the film deposition rate of the plasma but also steadily etches the deposited film surface and by removing carbon and retards the deposition rate at the film surface. Increasing the fraction of oxygen in the plasma zone, the resulting deposited films change their composition from being similar to the precursor to $SiO_2$-like films. However, high purity $SiO_2$ films are difficult to obtain as the film network strongly depend on the process parameters. As the $SiO_2$ films are deposited from small particles with nanometre size, voids inside the coating cannot be avoided without using high energy ion bombardment or high substrate temperatures.

## 2.3 Forming of coated metals

### 2.3.1 Fundamentals of forming of metal sheets

The theoretical descriptions of metals based on the view that metal atoms are orientated regularly and form a closed packed lattice. In the ideal case single crystals are formed. In most cases technical materials are polycrystalline materials. During cooling of the metal different orientated single crystals (grains) are formed. The sizes of these grains depend on the cooling rate and the composition of the metal or alloy. During forming of metals by an

external force atoms are moved against each other on an atomistic length scale. Macroscopically the metal is deformed either reversible and elastic or irreversible and plastic. To plastically deform a polycrystalline material the direct stress must be higher than on a single crystalline material. This is based on the fact, that the applied stress on an individual grain can also change neighbouring grains with their individual stress levels [64, 65].

From a technical point of view, the mechanical properties of metal sheets are evaluated by so-called elongation-strain diagrams. An extensive introduction of sheet metal forming is given by Marciniak et al. and Lange and Döge et al. [66-68]. The elongation of a sample is recorded versus the applied strain. By normalizing the measured strain with the cross-sectional area of the sample the so-called engineering stress-strain curve is calculated. Thereby the material properties are independent of the initial dimensions of the sample. To overcome the fact, that the strain is always measured on the original sample length, the study of the forming process is based on the true stress and true strain measurement.

For metal forming a constant volume of the test sample can be assumed and therefore the true stress is defined as

$$\sigma = \frac{P}{A_0}\frac{l}{l_0} \tag{10}$$

where $A_0$ is the initial sample cross-sectional area and $l_0$ is the initial gauge length of the sample. $l$ defines the final gauge length and P is the applied load.
The deformation degree of a sample is normally written as technical deformation $\varepsilon_t$ given in percent. A second definition for the forming degree is the logarithmic forming degree $\varphi$, which change is defined as the length change $dl$ of the actual length $l$ of the test specimen:

$$d\varphi = \frac{dl}{l} \tag{11}$$

For very small strains, the strain increment is very similar to the engineering strain, but for larger strains there is a significant difference. If the straining process continues uniformly in one direction till $l_1$ is reached, as it does in the tensile test, the strain increment can be integrated to represent the true strain:

$$\varphi = \int d\varphi = \int_{l_0}^{l_1} \frac{dl}{l} = \ln\frac{l}{l_0} \tag{12}$$

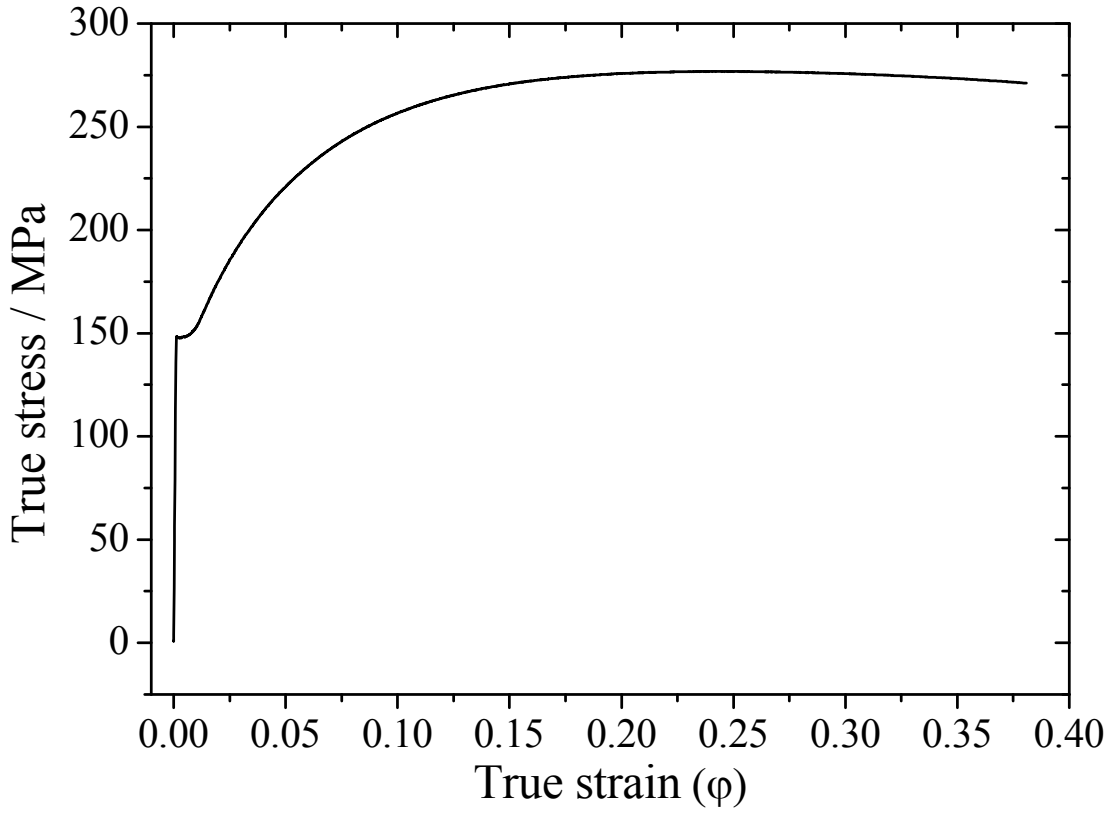


*Figure 5: True stress-strain diagram of a tensile tested HDG steel versus logarithmic deformation degree.*

The use of the logarithmic forming degree has the advantage, that forming steps can easily be summed up. The typical true stress versus true strain diagram of the used HDG steel is shown in Figure 5.

Comparing the derived stress – strain curves, the forming of metal sheets can be divided in different mechanism. Depending on the external applied force reversible, elastic and irreversible plastic deformation takes place.

The elastic tension of the metal sheet is described by the Hook's straight where the material behaves like a spring and returns to the original form according to Hook's law with the applied external force $F_{ext}$, the spring constant $D$ and the elongation $\Delta l$ :

$$F_{ext} = D \cdot \Delta l \tag{13}$$

As most metals do not show a defined elastic limit, typically the elastic limit for metals is below 0.2% elongation of the initial length of the test specimen. This point at the end of the Hook's straight is called elastic limit $R_e$. From this point the plastic deformation starts and the material will be formed irreversible.

The maximum true stress is called the ultimate tensile strength $R_M$ and is calculated as

$$R_M = \frac{\max P}{A_0} \tag{14}$$

Until $R_M$ the sample will be formed without constricting and this region is called uniform strain as the sample keeps its shape. Beyond $R_M$ the sample constricts in the central part till further forming will break the sample in this area.

The forming of metal sheets can be done in different ways depending of the form of the sample and the tooling machine. Four major groups can be separated uniaxial, biaxial, plane strain and deep drawing. The forming process can be described by three individual forming degrees $\varphi_{1,2,3}$, which are parallel to the direction in space. $\varphi_1$ represents the major strain with the largest change of the dimension of the test specimen. $\varphi_2$ indicates the change of the width of the metal sheet and $\varphi_3$ represents the change of the sheet thickness.

For all forming mechanisms the volume of the specimen is constant during forming and therefore the sum of the three forming degrees is zero:

$$\varphi_1 + \varphi_2 + \varphi_3 = 0 \tag{15}$$

All forming operations related to this thesis are done during tensile testing. Therefore, all samples were formed by uniaxial deformation of the metal samples. This means, that the samples were elongated in the direction of $\varphi_1$, whereas the width of the samples ($\varphi_2$) decreases. The correlation between the major and minor strains is given in equation 16.

$$\varphi_1 = -2\varphi_2 \tag{16}$$

The comparison of the uniaxial forming and further forming operations like plane strain, deep drawing and biaxial forming is shown in the forming limit diagram in Figure 6.

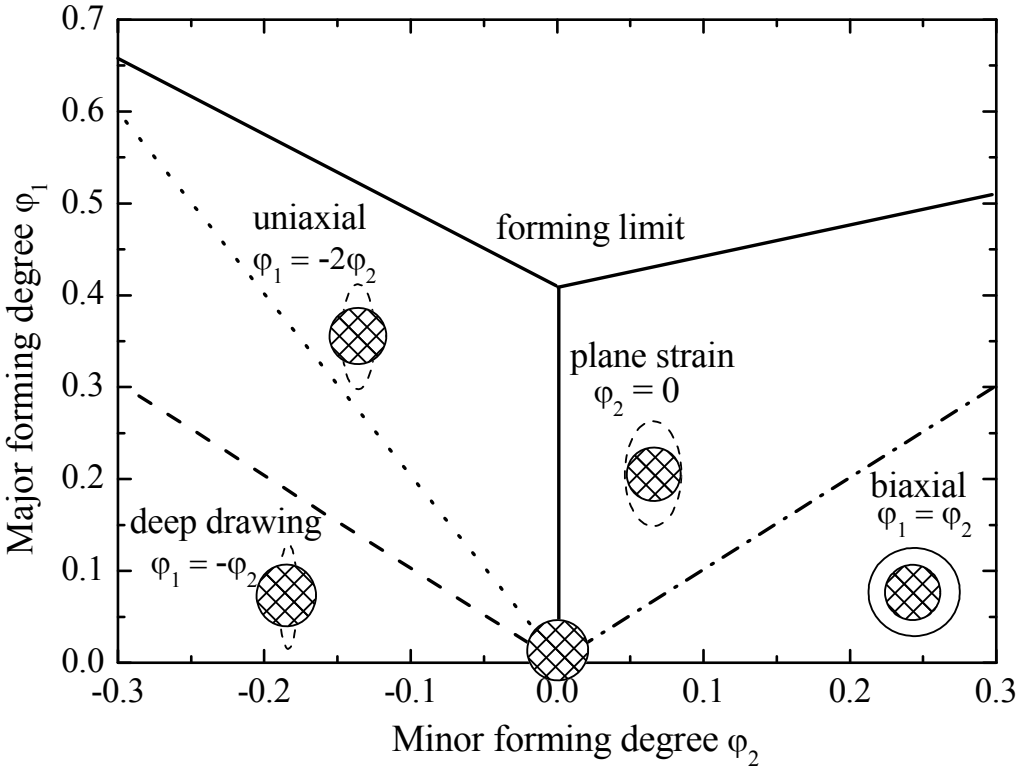


*Figure 6: Forming limiting diagram for sheet metal forming indicating the major forming modes (according to [66]).*

### 2.3.2 Forming of zinc and zinc coated metals

Macroscopically the forming of metal sheets was described above. On an atomistic level, the deformation of the polycrystalline zinc can be understood on closer examination of the deformation behaviour of single crystals [67, 68].

In the case of small deformations, the applied stress leads to a linear translation of the lattice which shows elastic behaviour due to Hook's law (Figure 7). Releasing the applied stress the atoms are forced to return to their origin position.

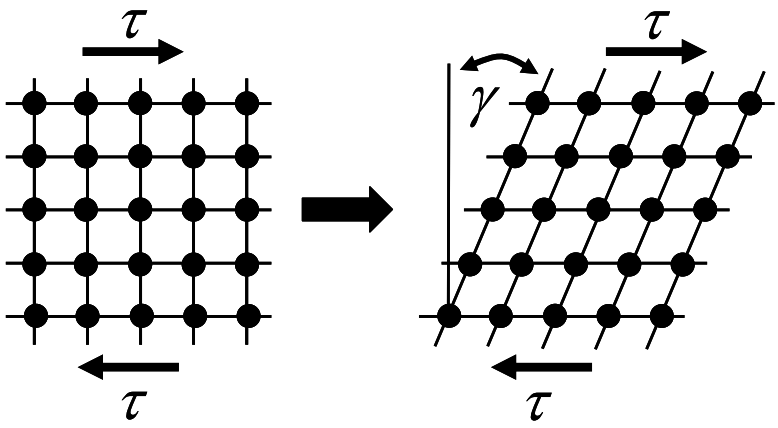


*Figure 7: Elastic deformation of a crystal lattice due to shear stress $\tau$ for an angle $\gamma$ [68].*

If the applied stress is larger than the elastic part the crystal is plastically deformed. Hexagonal close-packed (hcp) metal single crystals, e.g. zinc crystals, are characterized by the ratio (c/a) where c and a are the height and the edge size of the hexagonal cell, respectively. They are also known to exhibit a very anisotropic mechanical behaviour like elasticity and plasticity. For zinc, c/a = 1:856 > 1:633 which is the value for the maximal density of hcp metals. Therefore, basal slip is the easiest deformation mode in zinc [27, 28]. Non-basal slip, twinning and strain relaxation at grain boundaries have been experimentally observed for zinc [21, 69].

For zinc, twinning is favoured by compression parallel and tension normal to the c-axis. The formation of twins is shown in Figure 8. They appear along the twin plane, where a part of the lattice will be transformed into a mirror image. Thus, unlike slip, twinning is very dependent on the sense of the stress applied on the crystal [27]. One effect of twinning is that grains unfavourably oriented for slip will be reoriented into a more favourable position.

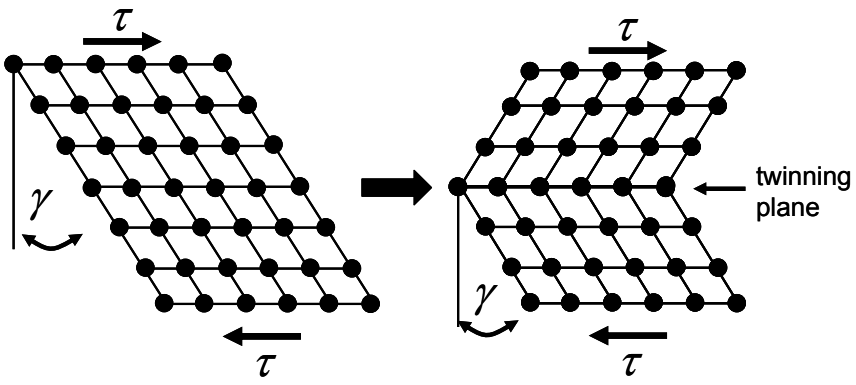


*Figure 8: Formation of twins due to shear stress $\tau$ [68].*

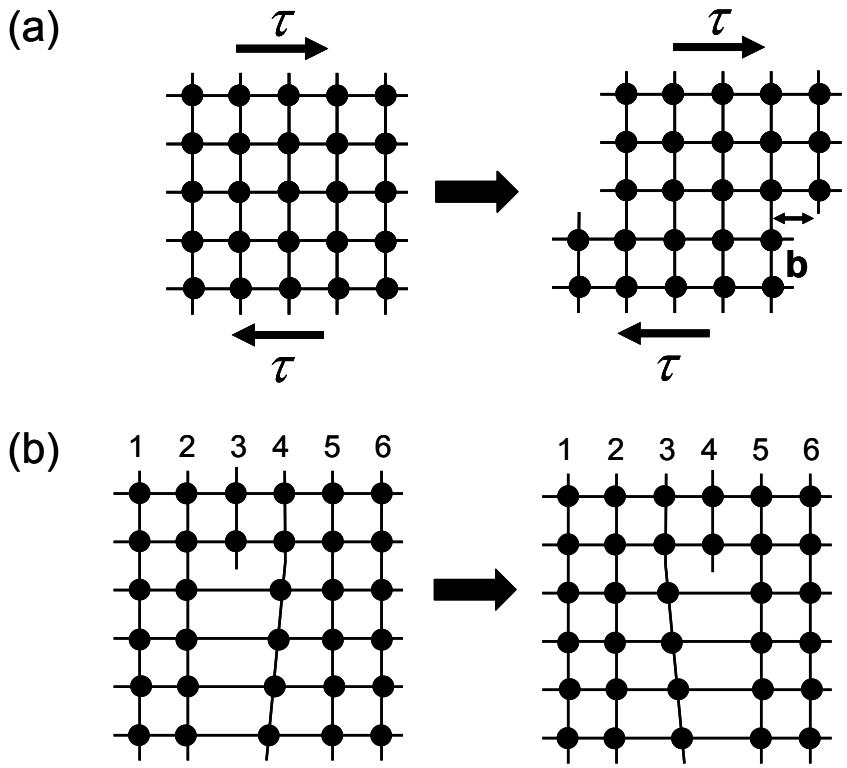


*Figure 9: (a) Fixed sliding along the sliding plane for a length of the lattice constant b due to shear stress $\tau$ for a perfect crystal. (b) Single dislocation for a none ideal crystal with the migration of defects between different lattice planes [68].*

Plastic deformation by sliding is separated in two mechanisms as shown in Figure 9. Fixed sliding can be found on ideal crystals if all atoms from one lattice plane are moved simultaneously against the atoms from the neighbouring lattice plane. In technical metals defects inside the lattice plane allows the migration between the lattice planes. Typically atomic surface steps are caused by single dislocations within the crystals [70].

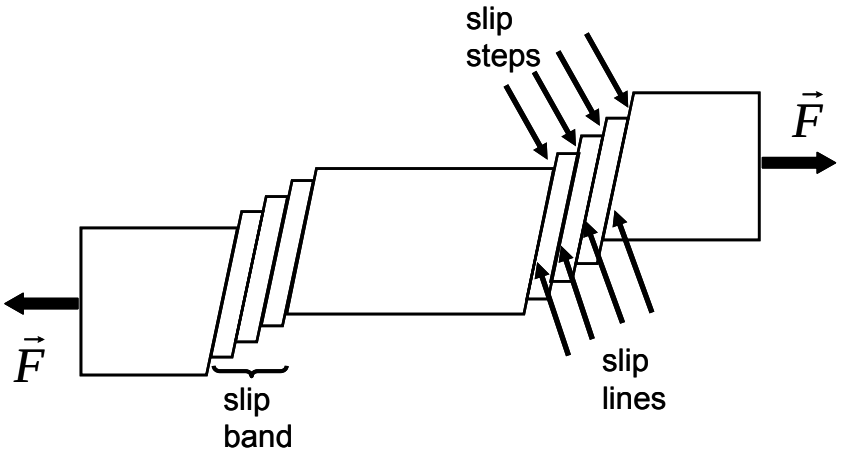


*Figure 10: Schematic picture of plastic deformation by large crystallographic slip steps created by a set of collectively gliding dislocations [68].*

Figure 10 shows the schematic picture of plastic deformation which can be found on zinc crystals. Atomic slip steps are caused by single dislocations leaving the bulk, larger crystallographic slip steps (so-called slip bands) created by sets of collectively gliding dislocations on parallel or identical glide planes [70].

In most cases technical samples are polycrystalline materials, which are formed from single crystals, also called grains, with different crystallographic orientation. The applied stress for the plastic deformation of polycrystals with different grain orientations must be higher than the stress of the individual singe grains. A single grain cannot be formed individually as long as the critical stress in the neighbouring grains is high enough to also plastically form the neighbouring grains. Therefore, the deformation of neighbouring grains show identical forming behaviour at the grain boundaries [68, 71].

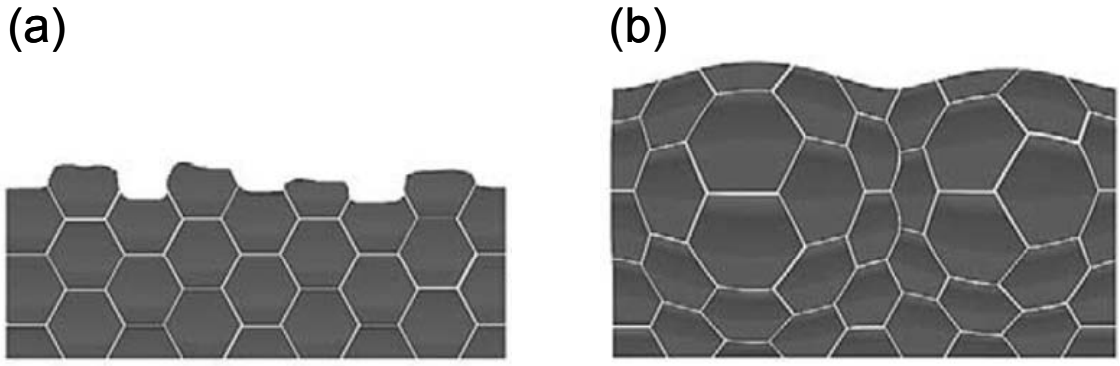


*Figure 11: (a) Orange peel phenomena. (b) Ridging and roping phenomena. [70]*

Besides the nanoscopic defects on the single grains, macroscopic phenomena occur during forming which is described in detail by Raabe et al. [70]. The grain-scale roughening in homophase alloys can be grouped into orange peel and banding phenomena which are illustrated in Figure 11. Both are characterized by the out-of-plane displacement fields (negative or positive), which roughly map the grain shape of the material. Orange peel occurs when different crystals produce individual out-of-plane grain-scale surface displacements due to their different orientation factors and the resulting shape changes. Banding is commonly referred to as ridging or roping. It occurs in the form of banded surface undulations.

### 2.3.3 Forming of plasma polymer films

The mechanical behaviour of thin films on metallic or deformable substrates was studied intensively in several publications [17-19, 72]. Most of the works focused on the formation and the propagation of cracks in the coatings on ductile or deformable substrates and were studied experimentally e.g. for zirconia thin films on stainless steel or inorganic films on polymeric substrates like SiOx films on PET.

In the case of thin ductile films on elastic substrates the crack formation and the crack propagation can be described within the framework by the so-called shear lag approximation explained in detail by Wojciechowski and Mendolia [17]. Usually, multiple sequential crack formation in the coating for these cases is observed with an increase of the number of cracks with increasing strain (see Figure 12). If a certain crack density is reached further strain results only in an opening of the cracks but the number of cracks stays constant. The formation of equidistant cracks in the coating is based on the non-localised distribution of strain over the coating. For metallic surfaces this behaviour is limited on small forming degrees as the plastic deformation of the substrate cannot be neglected for larger strains.

The mechanical behaviour of the coating strongly depends on the adhesion between the coating and the substrate surface. In the case of weak adhesion or strong intrinsic stress inside the coating, the coating will delaminate easily if further stress is applied due to straining of the sample. In the case of strong adhesion of the coating during forming, the surface defects as described in the previous chapter like atomic slip steps caused by single dislocations leaving the bulk, larger slip bands created by collectively gliding dislocations, surface twins and macroscopic phenomena like orange peel and ridging and roping have strong impact on the behaviour of the coating.

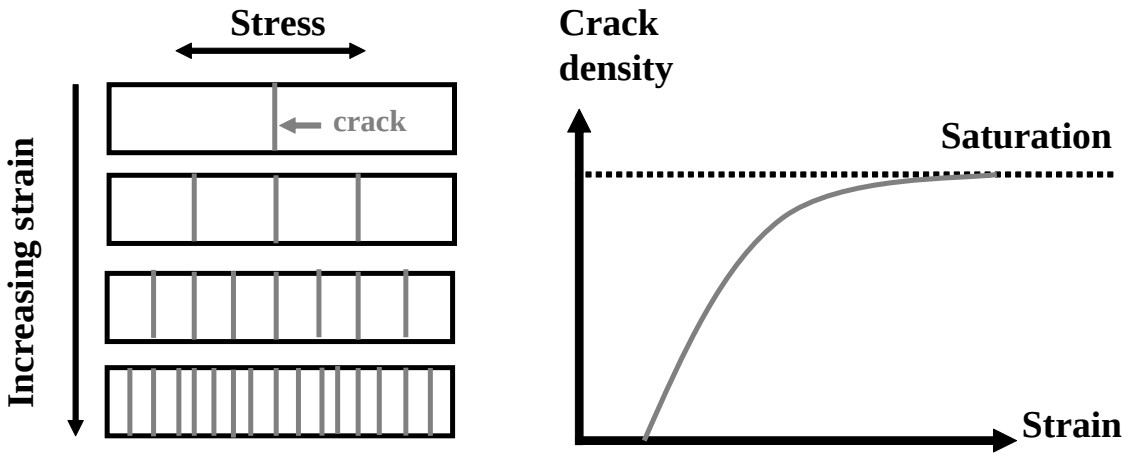


*Figure 12: Schematic picture of sequential or so-called mode-I crack formation during uniaxial forming [17].*

Kirk and Pilliar reported about slip planes emerging the surface of TiN coatings on steel [72]. All cracks in the TiN coating were observed to be located near the slip bands.
Baumert et al. reported similar behaviour of the forming of thin plasma polymer films on electrolytically galvanised and chemically polished steel [24].

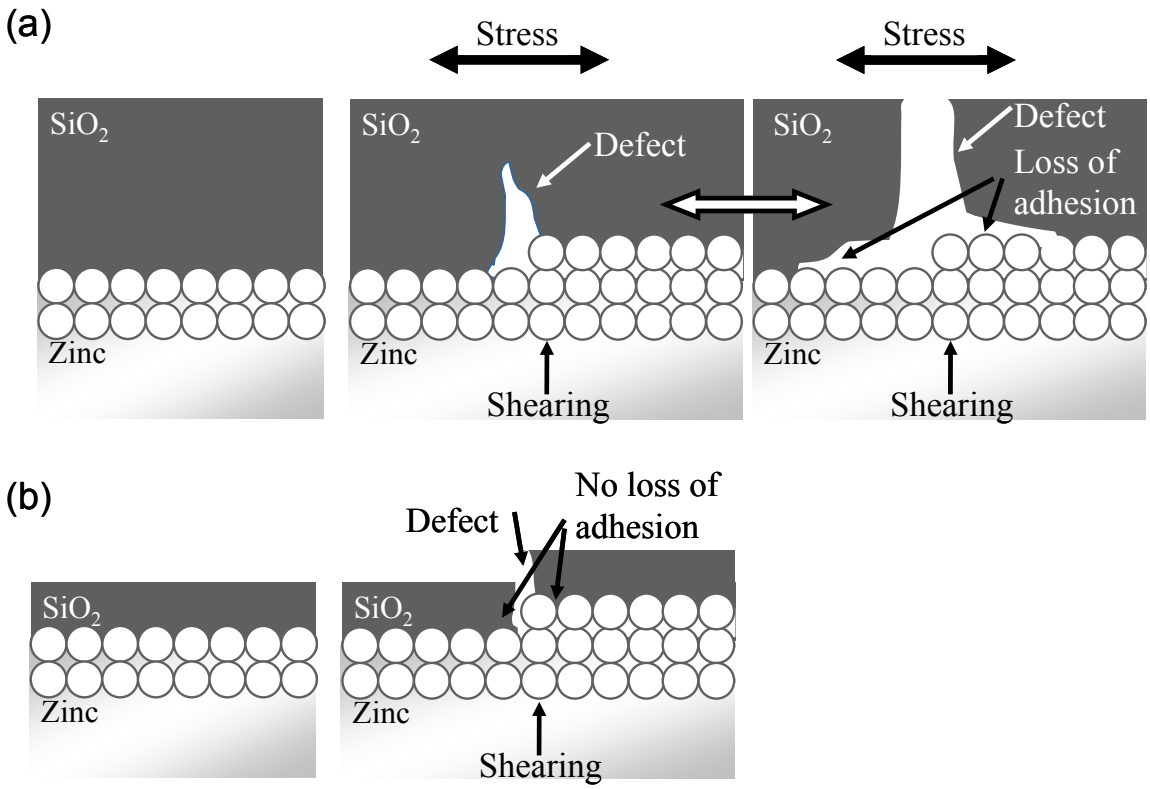


*Figure 13: Substrate induced crack formation in $SiO_2$ coatings for (a) thick $SiO_2$ coatings and (b) for ultra-thin coatings (20-50 nm) according to [24].*

They reported, that unlike the multiple sequential cracking with equidistant cracks for thin coatings on strained substrates, most of the cracks within the $SiC_xO_y$-like coating are observed near to slip bands of the steel. On the slip bands, however, the crack morphology is quite similar to the usual multiple cracking on deformable substrates. For thicker coatings (e.g. thickness > 100nm) the localized strain and stress concentrations within the coating seem to be dissipated beyond the slip bands. Figure 13 shows the substrate induced cracks, whereas the stress within the thick coating can be dissipated over defects in the substrate without formation of cracks within the plasma polymer coating. On fine gliding grains real transverse crack formation is observed. However, at high film thickness values the complete de-adhesion of the $SiO_x$-like coating can be observed.

# 3 Experimental measurement techniques

## 3.1 Electrochemical measurement techniques

### 3.1.1 In-situ and scanning Kelvin probe

Height regulated scanning Kelvin probe (HR-SKP) measurements were performed for corrosion studies by using a self-designed height regulated probe which is described explicitly in [73, 74]. The samples were measured in a cleaned gas atmosphere by using air with 95% relative humidity. A plane-ended, electrochemical etched Ni/Cr cylindrical wire (diameter approximately 80 μm) was used for the scanning of the sample surface in x, y and z direction. The calibration of the NiCr probe was done by measuring and referring to $Cu/CuSO_4$. For corrosive de-adhesion studies, the defect area was filled with 0.5M NaCl solution.

The work function of the samples in vacuum was detected in-situ by means of a Kelvin probe in the plasma cell described in Chapter 4.2.1. A heat treated graphite needle (Staedler 2B marsmicro) of 0.5 mm diameter was used for the in-situ vacuum measurements during each plasma treatment step. The graphite tip was measured versus HOPG as reference as described in [75]. For in-situ Volta potential relaxation measurements by switching from dry to humidified air a plane-ended, electrochemical etched Ni/Cr cylindrical wire (diameter approximately 500μm) was used.

All potentials measured by the KP and the HR-SKP are given with respect to standard hydrogen electrode (SHE).

### 3.1.2 Electrochemical impedance spectroscopy

Electrochemical impedance spectroscopy (EIS) is a very common technique used in material and surface science to investigate the barrier properties of films e.g. organic coatings on metallic substrates [11, 15, 76]. To test the barrier properties of a coating the electrochemical impedance is measured by applying a sinusoidal potential excitation with a small amplitude over a range of frequencies to an electrochemical cell. The frequency dependent current answer of the electrochemical cell is described by the complex impedance, which also takes into account the phase shift of the current answer and the applied potential.

If the interface can be described by an ideal resistor, no phase shift takes place and the impedance is identical with the ohmic law, where E is the applied voltage, I the applied current and $R_{ohm}$ the ohmic resistance.

$$E = R_{ohm} \cdot I \tag{17}$$

In non-ideal systems, the complex impedance measurements can distinguish between ohmic parts (e.g. interface and electrolyte resistance) and capacitive parts (e.g. double layer capacitance or coating capacitance) by simulating the system as a network of resistors and capacitors. The complex impedance is described by the capacitance and the radial frequency $\omega$:

$$| Z |= \frac{1}{i\omega C} \tag{18}$$

The capacitance of a perfect barrier coating can be described by a plate condenser. The condenser consists of two plates formed by the surface or the electrode and the electrolyte. Between these two plates the coatings exists as a dielectric. The capacity C of the condenser is proportional to the plate area A, the dielectric constant of the vacuum $\varepsilon_0$, the dielectric constant of the material between the plates $\varepsilon_r$ and inverse proportional to the thickness of the coating d.

$$C = \frac{\varepsilon_0 \cdot \varepsilon_r \cdot A}{d} \tag{19}$$

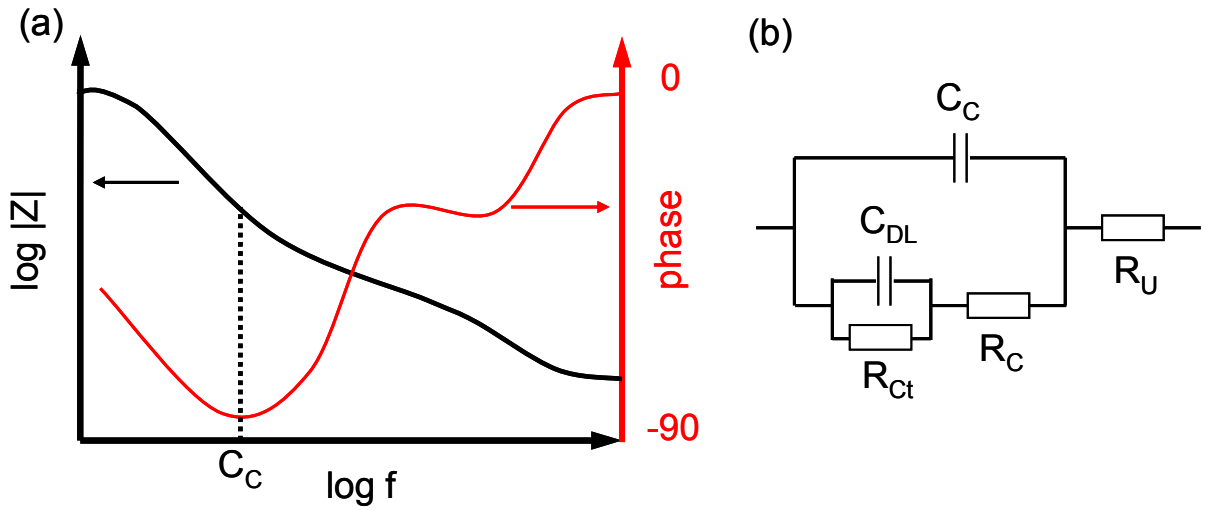


*Figure 14: (a) Bode plot and (b) equivalent circuit of a non ideal barrier coating in contact with an electrolyte.*

Figure 14 shows the Bode plot and the respective equivalent circuit for a non ideal barrier coating. Defects occur by pores within the barrier coating and the electrolyte is able to penetrate the coating and reaches the surface of the metal electrode. The penetrating electrolyte is reflected similar to the uncompensated electrolyte resistance $R_U$ and by an ohmic resistor $R_C$ of the coating which is connected in parallel with the coating capacitance $C_C$. If the electrolyte has reached the metal surface, the system can be described by a normal metal electrode equivalent circuit with the pore resistance $R_{Ct}$ and the double layer capacitance $C_{DL}$. The coating capacitance can be distinguished from other capacitive parts, as the phase is quite close to -90° for ideal barrier systems.

The electrochemical measurements were performed using a Zahner IM6d potentiostat (Zahner-Elektrik Gmbh & CoKG, Kronach, Germany). A three electrode setup with the working electrode comprising of a reproducible, exposed area of 2.26 $cm^2$, a platinum counter electrode and a saturated Ag/AgCl reference electrode (+198mV versus SHE) was used. All electrochemical experiments were carried out in quiescent borate buffer solution (0.05M $Na_2B_4O_7 \cdot 10H_2O$ + 0.05M $Na_2SO_4$ + 0.2M $H_3BO_3$) prepared using millipore water with pH 8.3 at 22 ± 1°C. The electrochemical impedance spectra were measured, at open circuit potential, in the range of 0.1 Hz up to 100 kHz with 10 points per decade and with an amplitude of 10 mV rms, using the above described three electrode set-up.

### 3.1.3 Cyclic voltammetry

Cyclic voltammetry (CV) can be described as a potentiodynamic electrochemical measurement as described in detail in [77]. The working electrode potential is ramped linearly versus time and the flowing current density is measured. This ramping is known as the experiment's scan rate.

If a material can be reduced by the electrolyte, than the current density will increase as the ramped potential reaches the reduction potential of the material, but decreases as the concentration of the material is depleted close to the electrode surface. If the redox couple is reversible than the former reduced material can be reoxidized when the oxidation potential is reached. For ideal systems the current densities between the oxidation and reduction process are equal and the oxidation and reduction peaks in the voltage versus current density plot have a similar shape. The amount of charge which is transferred to the electrolyte when the material is reduced or oxidized is directly proportional to the surface area which is in contact with the electrolyte. If parts of the surface are covered with a barrier film which cannot be oxidized or reduced at potentials when the metal substrate can be oxidized or reduced, than the protected area can be directly calculated by the difference of the charge transfer on an unprotected and a partially protected surface [78, 79].

Cyclic voltammograms were obtained with a Zahner IM6d potentiostat and the same set-up as described above over a voltage range of -750 to -1150 $mV_{SHE}$ at ambient temperature and a scan rate of 50 mV/s.

Cyclovoltammetry was also measured in-situ during forming by a unique combination of a tensile testing device with a home-made three electrode electrochemical micro capillary cell [80]. The layout of the bone shaped tensile samples and the setup of the in-situ cyclovoltammetry measurements is described in Chapter 4.3.2. All ex-situ and in-situ CV measurements were carried out in quiescent borate buffer solution (0.05M $Na_2B_4O_7 \cdot 10H_2O$ + 0.05M $Na_2SO_4$ + 0.2M $H_3BO_3$) prepared using distilled water with pH 8.3 at 22 ± 1°C. The cyclic voltammograms were obtained over a voltage range of -525 to -1275 $mV_{SHE}$ at ambient temperature and a scan rate of 100 mV/s with a gold reference electrode.

## 3.2 Spectroscopic measurement techniques

### 3.2.1 Infrared spectroscopy

Fourier transformed infrared reflection absorption spectroscopy (FT-IRRAS) in combination with polarization modulation can be used for the characterization of thin films or monolayers on metallic or highly doped semiconducting surfaces. The advantage of this method is the high surface sensitivity due to the grazing angle of incidence and the surface selection rule and that the modulated reflectivity is independent of the isotropic adsorption from gas or bulk water. Therefore, the interfering effects of gas or bulk water and carbon dioxide in the beam path can be eliminated [49, 81].

The infrared spectra were measured between 4000 and 750 $cm^{-1}$ by means of a Biorad Excalibur 3000 (Digilab, Randolph, USA) equipped with a mercury cadmium telluride detector (MCT) cooled with liquid nitrogen. Each spectrum represents a co-addition of 256 or 512 scans at a resolution of 4.0 $cm^{-1}$. The spectra were water and baseline corrected using the Digilab resolution pro software package (version 4.0). The infrared beam was transmitted through ZnSe windows on the sample in the plasma cell and reflected under 80°. A discrete polarization modulation was used to enhance surface sensitivity and reduce gas phase absorption of residual water and carbon dioxide in the optical path [49]. The set-up is described in detail in chapter 4.2.1.

### 3.2.2 X-ray photoelectron spectroscopy

X-ray photoelectron spectroscopy (XPS) is a surface analysis technique to quantitatively measure the elemental composition, chemical and electronic state of the elements which can be found at the outermost 1 to 10 nm of the material. The primary excitation is accomplished by the irradiation of the surface by a source of monochromatic X-rays. The X-rays leads to the photoionisation of the atoms and the response of the atoms (photoemission) is detected by measuring the energy spectra of the emitted photoelectrons. The presence of peaks at particular binding energies therefore indicates the presence of a specific element in the sample under study. Furthermore, the intensities of the peaks are related to the concentration of the element within the sample region. The exact binding energy of the electrons depends not only upon the level from the photoemission, but also on the formal oxidation state of the atoms and the local chemical and physical environment. Therefore, small variations in the former

parameters result in a shift of the binding energy, the so-called chemical shift. These chemical shifts can be corrected by literature values, e.g. by comparing the binding energy of the C1s peak of the aliphatic groups with literature values of 285 eV. In combination with a sputter gun, depth profiling of the sample is possible with the determination of the elements and also with the binding state by using fitting algorithms [82].

XPS-spectra were measured by means of a Quantum 2000 ESCA Microprobe (Physical Electronics Inc., Chanhassen, USA) with a take-out angle of 45° and a spot size of 100 µm using monochromatic Al Kα-radiation. The element spectra were obtained by using a pass energy of 23.5 eV and an energy resolution of 0.2 eV. Sputtering was performed by ion beam sputtering with an ion beam of 2 kV on a 2 x 2 $mm^2$ spot. The sputter rate was 2.6 nm/min as calibrated with a $SiO_2$ standard sample. For data evaluation CASA XPS (version 2.3.12) was used.

### 3.2.3 Spectroscopic ellipsometry

Spectroscopic ellipsometry (SE) is widely used as standard for measuring the thickness and the optical constants of thin films. The key feature of ellipsometry is that it measures the change in polarized light upon light reflection on a surface or interface. Under certain conditions, linearly polarized light is reflected from a sample and the elliptically polarized light is analyzed. The amplitude ratio $\Psi$ and the phase difference $\Delta$ between the p- and s-polarized light waves are measured and fitted by a certain model which can describe the theoretical film system. From the fitting results, the thickness and the complex refractive indices can be determined [83].

A spectroscopic ellipsometer SE 800 from Sentech (Berlin, Germany) was used for ellipsometry measurements. The samples were measured at three different angle of incidence (50°, 60° and 70°) for a spectral range of 300 nm to 820 nm. The measurements were evaluated with SpectraRay 2 from Sentech. Therefore, a Cauchy-layer model was used to fit the ellipsometry data.

## 3.3 Microscopic techniques

### 3.3.1 Force microscopy

Atomic force microscopy (AFM) was developed to image surfaces in three dimensions on nanoscopic scales. A laser beam deflection system is used to detect the bending of the cantilever when the tip, which is located on the front of the cantilever spring, interacts with the sample surface by mechanical, magnetical or electrical forces. Scanning Kelvin probe force microscopy (SKP-FM) combines the high-resolution of force microscopy with the Kelvin probe technique to determine the potential or work function distribution of the sample surface. In a first step the sample surface is determined in contact mode. With the topographical information the cantilever is than moved over the surface with a certain distance. The potential or work function of the surface is than measured by analysis of the modulated voltage signal which is applied on the capacitor which is formed by the tip and the sample surface [48].

Surface topography and Kelvin probe potential mappings were investigated by means of AFM with a NanoWizard® AFM from JPK Instruments AG (Berlin, Germany). Measurements were carried out in tapping or contact mode for SKP-FM by using silicon sensors (NHC, obtained from NanoWorld, k=285 kHz, typical tip radius less than 10 nm). AFM topography and SKP-FM images were measured in dry nitrogen atmosphere with a typical tip-to-surface distance of 50 nm for the SKP-FM measurements.

### 3.3.2 Scanning electron and Auger microscopy

The scanning electron microscope (SEM) allows the study of morphology, composition and crystallography of conductive or metallised surfaces by scanning the surface with a high energy beam of electrons[78]. The resolution of a SEM is much higher in comparison to light microscopy as the wavelength of the electrons is much smaller than the wavelength used for optical microscopy. The most common mode used for imaging is detecting the secondary electrons which are ejected due to inelastic scattering with the beam electrons [84]. By using the backscattered electrons from the elastic scattered beam electrons, electron backscattered diffraction (EBSD) can be measured. EBSD is used to examine the crystallographic orientation of crystalline or polycrystalline materials [85].

SEM pictures were obtained on a Leo 1550 VP (Leo Elektronenmikroskopie GmbH, Oberkochen, Germany) for different forming degrees of the samples. SEM pictures were taken with an annular inlens SE detector, typical acceleration voltages between 2 and 5 kV and a working distance of 10 mm. The crystallographic orientation of the zinc grains was measured with a TSL EBSD analyzer by measuring the electron back scatter diffraction (EBSD) patterns and evaluation of the resulting Kikuchi lines.

Scanning Auger electron spectroscopy (AES) surface mappings were measured with a PHI 700 Scanning Auger Nanoprobe (Physical Electronics Inc., Chanhassen, USA). In comparison to SEM the subsequent relaxation of the ionized atoms leads to the emission of Auger electrons which are characteristic of the elements present in this part of the sample [84].

# 4 Experimental set-up and sample treatment

## 4.1 Materials

### 4.1.1 Used substrate material

Hot-dip galvanised steel sheets (HDG) were used as samples of technical interest. The interstitial free HDG steel (steel type DX54D, sheet thickness 0.85 mm) was supplied by OCAS N.V. (Zelzate, Belgium) in the non skin passed state, i.e. without being temper rolled after the application of the zinc coating. The thickness of the zinc coating (alloy composition: Zn + <0.3% Al) after hot-dip galvanising was 7 µm.

Additionally pure zinc foil (99.99%, Goodfellow, Bad Nauheim, Germany) with a thickness of 3 mm and a size of 50 x 50 $mm^2$ was used especially for the plasma modification of zinc surfaces.

Polished and solvent cleaned silicon wafers were used for thickness control measurements by spectroscopic ellipsometry.

### 4.1.2 Substrate cleaning and pre-treatment

Smaller samples were cut from the supplied material in a size of 12 x 4 $cm^2$ for the HR-SKP measurements. For the forming experiments with the miniature tensile testing device samples (2 x 5.1 $cm^2$) were cut in a bone like shape. All samples were cleaned in three different solvents in an ultra-sonic bath for 20 minutes to ensure complete removal of any oils or surface contaminations. As solvents Tetrahydrofuran (THF), iso-propanol and ethanol with analytical grade (Merck KGaA, Darmstadt, Germany) were used. After every solvent treatment the samples were dried under flow of dry nitrogen. Subsequently, the samples were cleaned by an additional alkaline cleaning step to remove the aluminium oxyhydroxide surface layer.

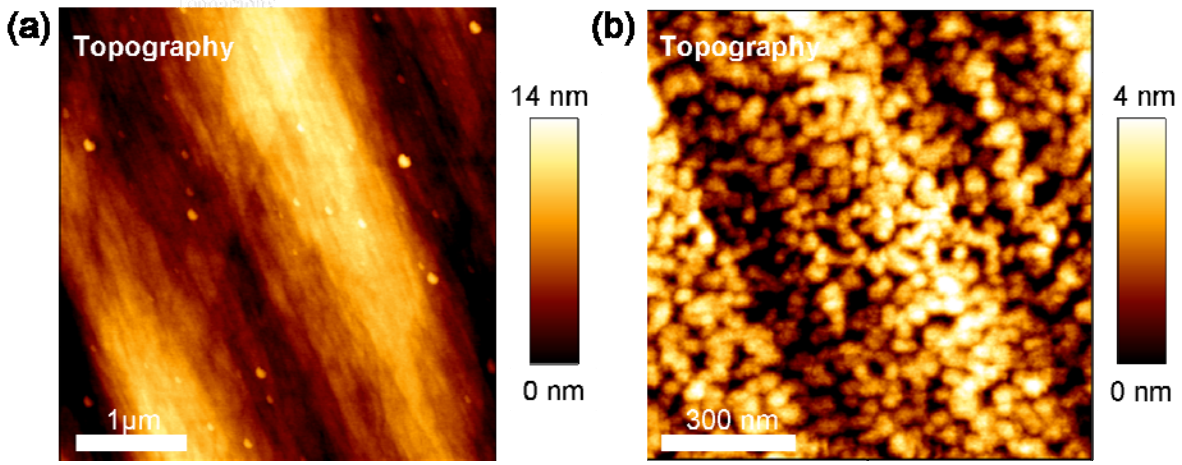


*Figure 15: AFM topography of (a) solvent cleaned HDG and (b) after alkaline cleaning of HDG.*

The samples were immersed for 30 seconds in a magnetically stirred aqueous solution of 30 g/l Ridoline 1570, 3 g/l Ridosol (Henkel KGaA, Düsseldorf, Germany) at 55 °C. Finally, samples were rinsed thoroughly with purified water and immediately dried in a stream of dry nitrogen.

*Table 1: Atomic percent of the surface composition after cleaning steps measured by XPS.*

| | Zn | O | Al | C |
|---|---|---|---|---|
| Solvent cleaned | 16 % | 49 % | 14 % | 21 % |
| 5 s alkaline cleaned | 31 % | 47 % | 8 % | 14 % |
| 30 s alkaline cleaned | 33 % | 46 % | <0.1 % | 21 % |

The topography of the surface before and after alkaline cleaning is shown in Figure 15. The surface of the solvent cleaned sample shows a large scale waviness due to the drying process during hot-dip galvanising. The alkaline cleaning, which is an etching of the aluminium surface layer leads to nanoscopic roughening of the surface. The waviness of the surface is still present after alkaline cleaning. Table 1 shows the atomic concentration for the different cleaning steps with the reduction of the aluminium concentration due to the alkaline cleaning.

### 4.1.3 Application of organic top coat

For the corrosive de-adhesion studies obtained by HR-SKP, a styrene/n-butylacrylate latex binder from BASF AG (BASF AG, Ludwigshafen, Germany) with a particle size of 140 nm was bar coated on the samples (film thickness 2 µm) and dried for 12 hours at 100 °C. This

water-based coating is free from pigments or additives. The organic coating was applied after forming of the $SiO_2$ coated samples to avoid additional effects from forming induced defects of the organic coating.

## 4.2 Plasma modification

### 4.2.1 In-situ plasma treatment of metal surfaces

For the in-situ studies of the plasma surface modification and thin film deposition by low-temperature plasmas a special plasma cell was used. The set-up of the cell is shown in Figure 16 and was described and published in detail by Raacke et al. [75]. The chamber is equipped with a sample holder which can be moved by a linear stage between the plasma modification position and the FT-IRRAS and Kelvin probe (KP) measurement position. Different configurations of the electrodes allow the generation of low-pressure direct or remote plasmas.

The chamber was evacuated to a base pressure of $10^{-4}$ mbar before plasma treatment of the samples by using rotary vane pump in combination with a turbo molecular pump. A liquid nitrogen cooling trap was used during polymer plasma deposition to protect the pumping system. In this work the remote plasma was generated by using a commercial high voltage power supply with a frequency of 30.7 kHz and an adjustable voltage.

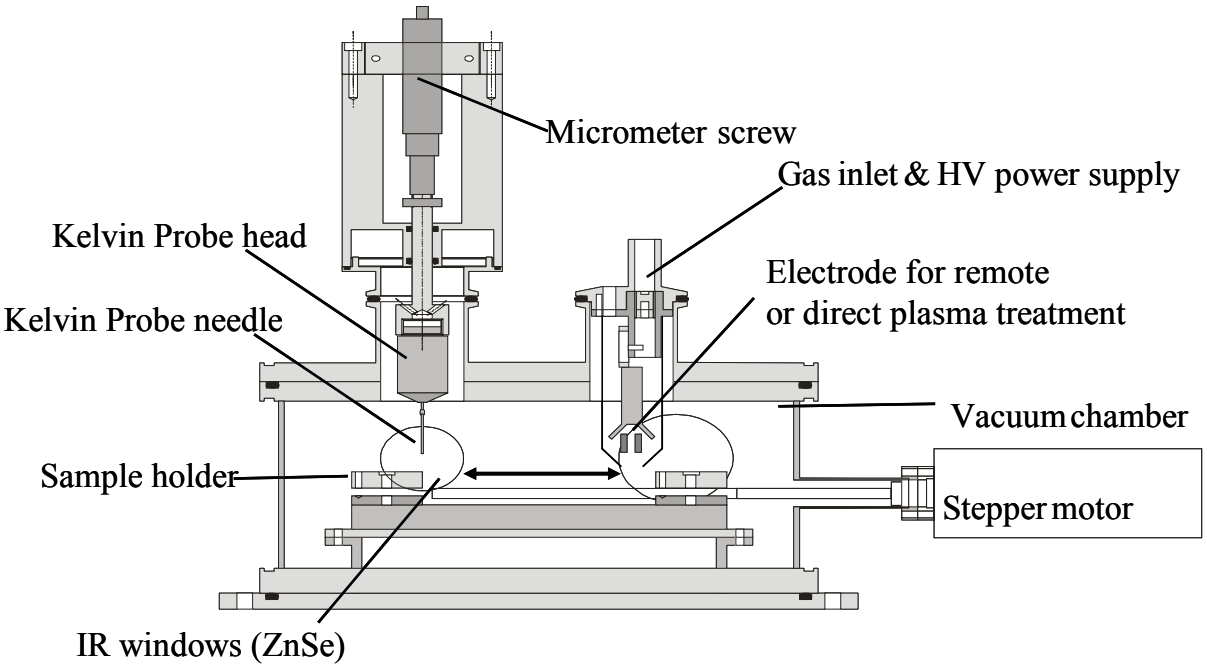


*Figure 16: Experimental set-up for the plasma modification of metal surfaces and the in-situ measurement of FT-IRRAS and work function by a vacuum Kelvin probe.*

The samples were moved through the modification area of the remote plasma in an argon/hydrogen plasma (1.5 sccm flow, 5:1 argon/hydrogen (purities 5.0/5.0), p = 0.3 mbar, 30 V) or an oxygen plasma (with 1.5 sccm $O_2$ (purity 4.5), p = 0.3 mbar, 30 V) within 6 minutes. After this oxygen plasma cleaning the optional $SiO_2$ film deposition was performed in a mixture of oxygen and hexamethyldisiloxane (HMDSO, $(CH_3)_3SiOSi(CH_3)_3$) from Fluka (purity 99.5 %) with a flow ratio of 20:1 (p = 0.3 mbar, 30 V) and different deposition times for varying film thickness values (typical deposition rate 0.5 nm/s). FT-IRRAS and KP measurements were performed before and after each plasma treatment step to correlate the surface chemistry with the chemical composition and the electronic structure.

### 4.2.2 PE-CVD film deposition

Besides the in-situ measurement described above, ultra-thin plasma polymer films were deposited by plasma enhanced chemical vapour deposition (PE-CVD). A plasma chamber from Roth & Rau (Hohenstein-Ernstthal, Germany) was used with a linear microwave plasma source and this enables the film deposition on samples up to DIN A4 in size. The chamber is shown in Figure 17 and described in detail elsewhere [86].

Before film deposition the chamber was pumped down to a base pressure below $10^{-3}$ mbar by using a roots pump and flushing the chamber three times with argon. The samples were moved with a constant speed through the plasma zone and cleaned by an oxygen plasma (400 W, 80 sccm/min $O_2$, v = 2 mm/s) at a pressure of 0.2 mbar. Immediately after this cleaning and activation step, the plasma polymer was deposited from a gas mixture of oxygen and HMDSO with a flow ratio of 20:1 (100 sccm : 5 sccm, p = 0.2 mbar, 300 W).

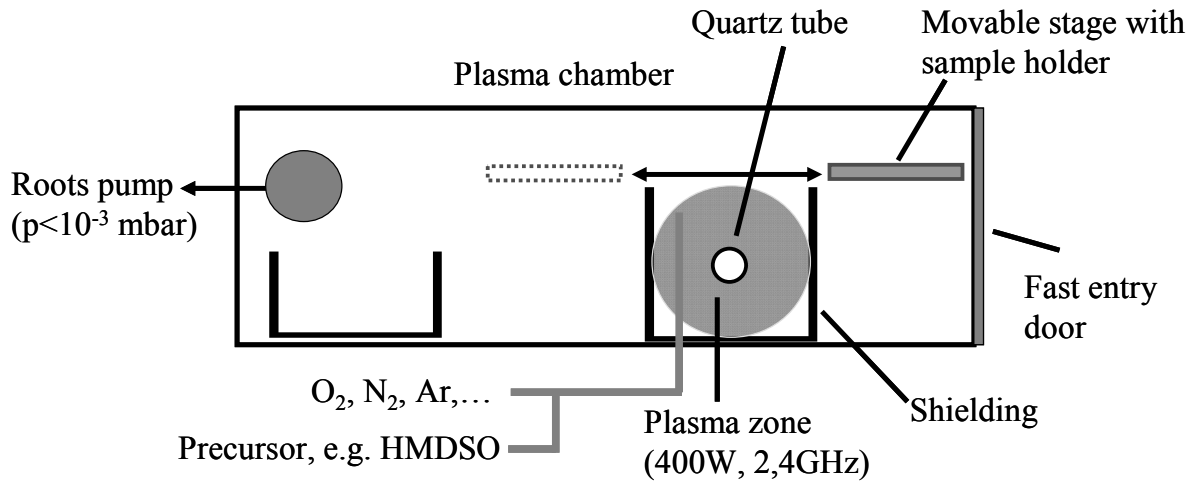


*Figure 17: Experimental set-up for large area PE-CVD.*

The substrates were moved through the plasma zone at a constant speed of 15, 5, 2 and 1 mm/s to obtain film thickness values of 10, 30, 50 and 100 nm. The thickness of the films was controlled with measurements on the samples as well as on silicon wafers by means of UV–VIS spectral ellipsometry (SE 800, Sentech, Berlin, Germany). The silicon wafers were attached near to the steel substrates during film deposition.

## 4.3 Forming of samples

### 4.3.1 Miniature tensile forming device

A custom built linear tensile testing device from Kammrath & Weise (Dortmund, Germany) with dog-bone shaped specimens (51 x 20 $mm^2$) was used for uniaxial straining along the long axis of the samples. The tensile forming device allows the uniaxial forming of samples with a maximum load of 5 kN. The clamps of the sample holder are electrical insulated and allow thereby electrochemical measurements without special shielding.

In this work, the forming degree for strained samples is given as the major strain $\varphi$ in a range of 0.00 to 0.25 which is directly correlated to the technical deformation usually expressed in percent.

### 4.3.2 In-situ cyclic voltammetry and forming set-up

A unique system for measuring impedance of organic coating on zinc coating steel during tensile forming was published by Klüppel et al [80]. This system allows the formability analysis of organic coatings on coated metal substrates during each separate forming step. In this work cyclic voltammetric measurements were used to follow the change of the unprotected zinc area during forming by adapting this set-up as shown in Figure 18.

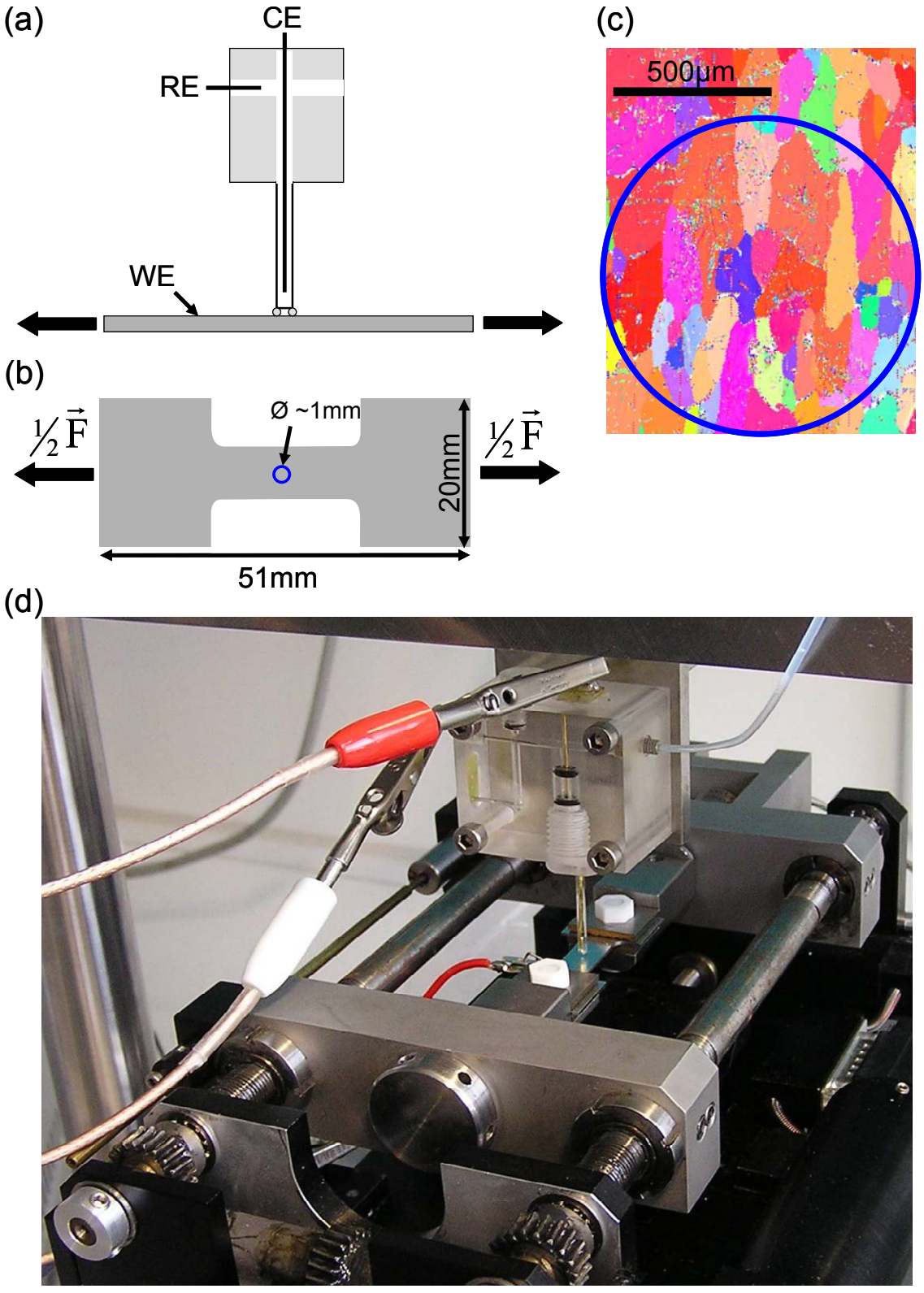


*Figure 18: Schematic set-up of the micro-capillary cell for in-situ cyclic voltammetry measurements during forming. (a) Side view of the sample with capillary cell. (b) Top view of the sample with central measurement spot. (c) Averaging of different grain sizes and grain. (d) Experimental set-up.*

A unique combination of the tensile testing device with a home-made three electrode electrochemical micro capillary cell with an Au-counter (CE) and Au-pseudo reference electrode (RE) was used. The sample as working electrode (WE) is clamped by an electrical insulated mounting in the tensile testing device. A 1 mm in diameter glass capillary was positioned in the middle of the forming area and filled with borate buffer solution. The glass capillary is many times larger than the typical grain size. This allows the measurement to be independent from different grain sizes and texture orientations as the results are averaged over many grains. A flexible silicon ring served as sealing and stayed in contact with the substrate surface during forming. This procedure ensured that always nearly the same sample area was electrochemically investigated; the contact pressure of the glass capillary on the surface is measured and controlled by a force gauge.

### 4.3.3 Tensile forming device for ex-situ experiments

Most experimental set-ups require a certain minimum size of the substrate material. For EIS, ex-situ CV and HR-SKP measurements larger substrates (120 x 40 $mm^2$) were uniaxially strained along the long axis on a Z100 from Zwick & Roell (Ulm, Germany). The resulting strain values and observed surface defects are comparable to the results obtained by the miniature tensile testing device.

# 5 Corrosion resistance of plasma modified HDG steel

In the past, several studies concerning the corrosion resistance of metal substrates covered with thin plasma polymer films were carried out [10-13]. However, the mechanism of corrosion protection of organically coated plasma modified surfaces is still poorly understood. Grundmeier et al. showed that a plasma oxidation of iron oxides on iron leads to change in the electronic properties [14]. However, the highly oxidised state of the passive film is not stable and changed again in humid atmospheres to the state which is determined by the oxygen reduction kinetics at the outer oxide surface. This process is also determined by the kinetics of the metal dissolution into the passive film at the metal/oxide interface.

Barranco et al. showed that for cathodically deposited plasma polymer films the interfacial electrode potential on iron could be effectively lowered which indicates a strong inhibition of interfacial oxygen reduction kinetics [15]. However, a reductive plasma treatment had to be followed by a sufficiently thick plasma polymer film deposition to prevent the plasma polymer/metal interface from re-oxidation. Based on this work electrochemical methods could be established for an improved understanding how plasma modifications influence the corrosion mechanism of thin film coated metals.

From the viewpoint of thin film engineering, it is the aim to achieve functional properties at extremely low thickness values. With regard to interfacial corrosive de-adhesion of polymer coated zinc and iron substrates, the interfacial oxygen reduction kinetics should be strongly inhibited by the respective plasma polymer film [15].

Therefore, the aim of this chapter is to show the modification of the passive film on zinc by ultra-thin barrier plasma polymer films and to correlate the structure and physical properties of the surface layer with the inhibition of the interfacial oxygen reduction kinetics in humid and corrosive environments.

## 5.1 Stability and chemical composition of oxygen plasma modified zinc surfaces

### 5.1.1 In-situ FT-IR analysis during plasma treatment

Pre-cleaned zinc coatings were argon/hydrogen and oxygen plasma treated. The corresponding in-situ FT-IRRAS difference spectra are shown in Figure 19. All peak assignments are listed in Table 2. After the $Ar/H_2$ plasma treatment, a removal of zinc-oxyhydroxides, carbonates, adsorbed hydrocarbons and surface hydroxyls could be detected as indicated by the negative peaks in the difference spectra. [35, 87].

*Table 2: Assignment of the FT-IRRAS peaks of the plasma modified zinc surface.*

| Wavenumber ($cm^{-1}$) | Group | Assignment | Ref. |
|---|---|---|---|
| 945 | Zn-OH | δ(OH) | [35, 87] |
| 1170 | Zn-OH | ν (Zn-OH) | [35, 87] |
| 1440-1475 | $CH_2$, $CH_3$ | $\delta(CH_x)$ | [88] |
| 1450 | $R\text{-}COO^-$ | $\nu_s(R\text{-}COO^-)$ | [35, 87] |
| 1570 | $R\text{-}COO^-$ | $\nu_{as}(R\text{-}COO^-)$ | [35, 87] |
| 1600 | $H_2O$ | $\delta(H_2O)$ | [87, 89] |
| 2850-2900 | $CH_2$, $CH_3$ | $\nu_{as,s}(CH_x)$ | [88] |
| 3300 | $H_2O$ | $\nu_s(OH)$ | [87, 89] |
| 3520 | $H_2O$ | $\nu_{as}(OH)$ | [87, 89] |

The subsequent oxygen plasma results in a measurable growth of the zinc-oxyhydroxide peak at 1170 $cm^{-1}$ with the composition $Zn(OH)_\delta O_{(2-\delta)/2}$ and further removal of surface hydrocarbons ($CH_x$). An increase in the surface hydroxyl density was not observed [35].

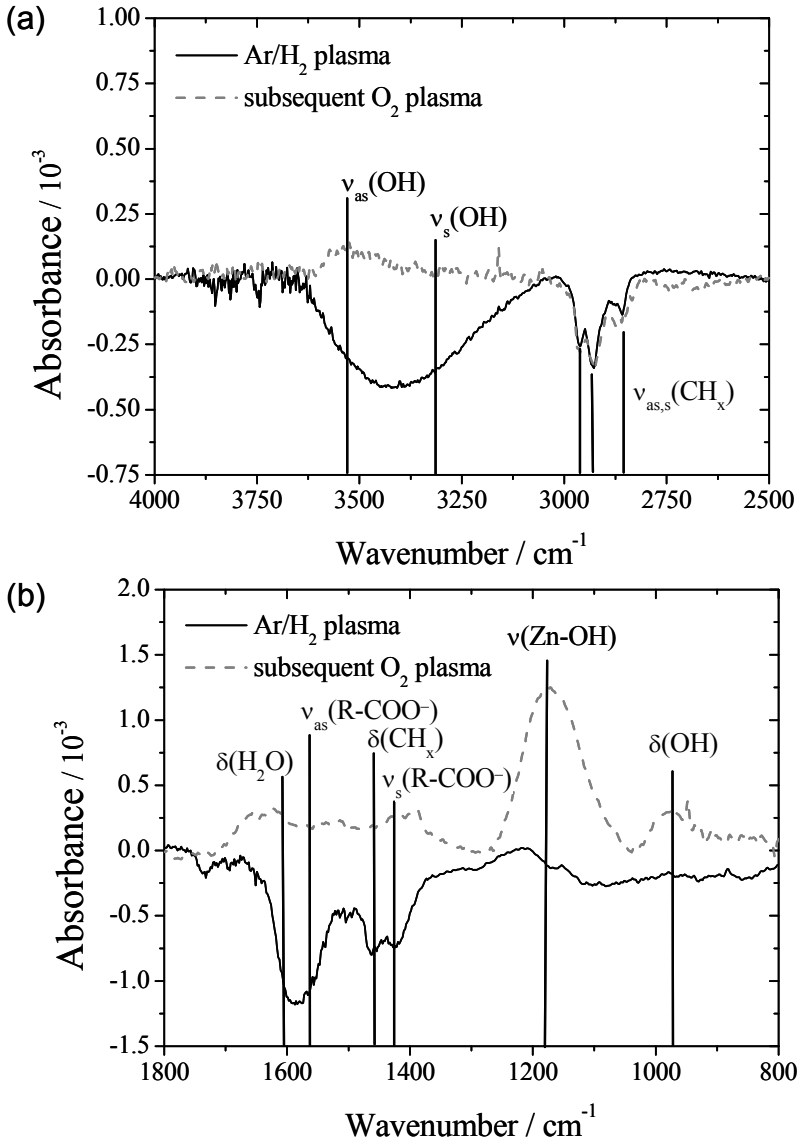


*Figure 19: In-situ FT-IRRAS difference spectra after Ar/$H_2$-plasma (reference: state before Ar/$H_2$-plasma) and subsequent $O_2$-plasma modification (reference: state after Ar/$H_2$-plasma) of alkaline cleaned hot-dip galvanised (HDG) steel. (a) 4000 - 2500 $cm^{-1}$ and (b) 1800 – 800 $cm^{-1}$.*

### 5.1.2 Chemical surface change after plasma treatment

Changes in the chemical composition of the passive film were observed by means of XPS sputter profiling. Sputter profiles of the Zn2p and O1s peaks for the alkaline cleaned HDG sample before and after oxygen plasma treatment are shown in Figure 20. The Zn2p and O1s peaks were fitted to calculate the different amounts of oxidized and metallic zinc as well as the different amounts of zinc hydroxide and oxide of the passive surface layer. The results indicate a thickening of the zinc hydroxide/oxide passive film due to the oxygen plasma

treatment in comparison to the non-plasma treated surface. The growth of the oxide thickness is most probably due to the increased density of adsorbed surface hydroxides and occurs via the high field mechanism [90]. Electrons are transferred from the zinc/zinc oxide interface to the outer zinc oxide surface and reduce the adsorbed oxygen atoms or hydroxyls. Zn ions are formed at the oxide/zinc interface and migrate to the surface to neutralize the adsorbed negative hydroxide ions.

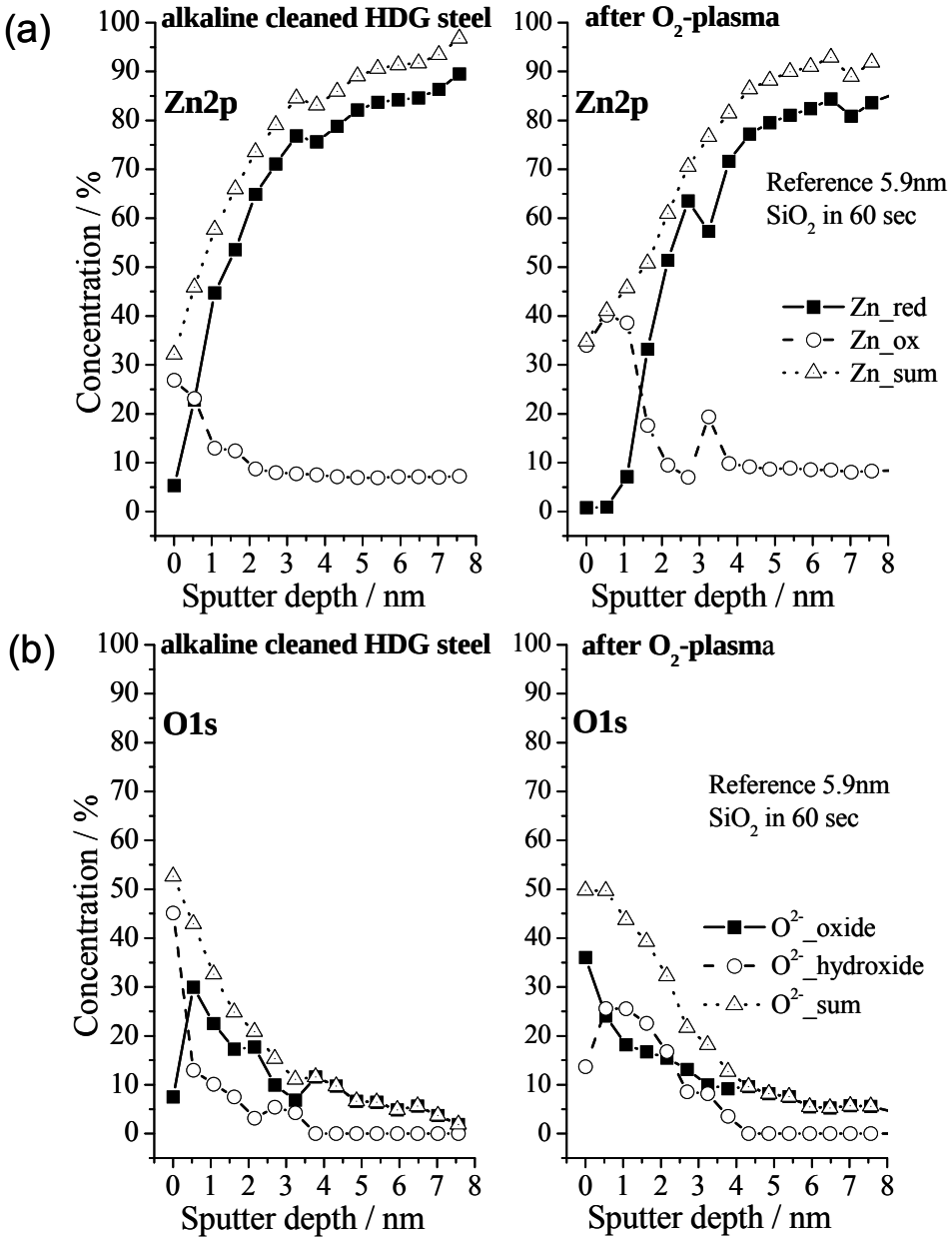


*Figure 20: Ex-situ XPS analysis of thickness change of oxide layer after oxygen plasma treatment.*

### 5.1.3 Influence of plasma treatment on Volta potential

In Figure 21 the change in the Volta potential of the argon/hydrogen cleaned and oxygen plasma modified surface in comparison to the untreated HDG surface is illustrated as it was measured in-situ at $10^{-4}$ mbar by means of the Kelvin probe. The reduction of the zinc surface by the argon/hydrogen plasma shifts the potential more cathodic (-150 mV). A very strong anodic shift of +600 mV after oxygen plasma treatment can be observed.

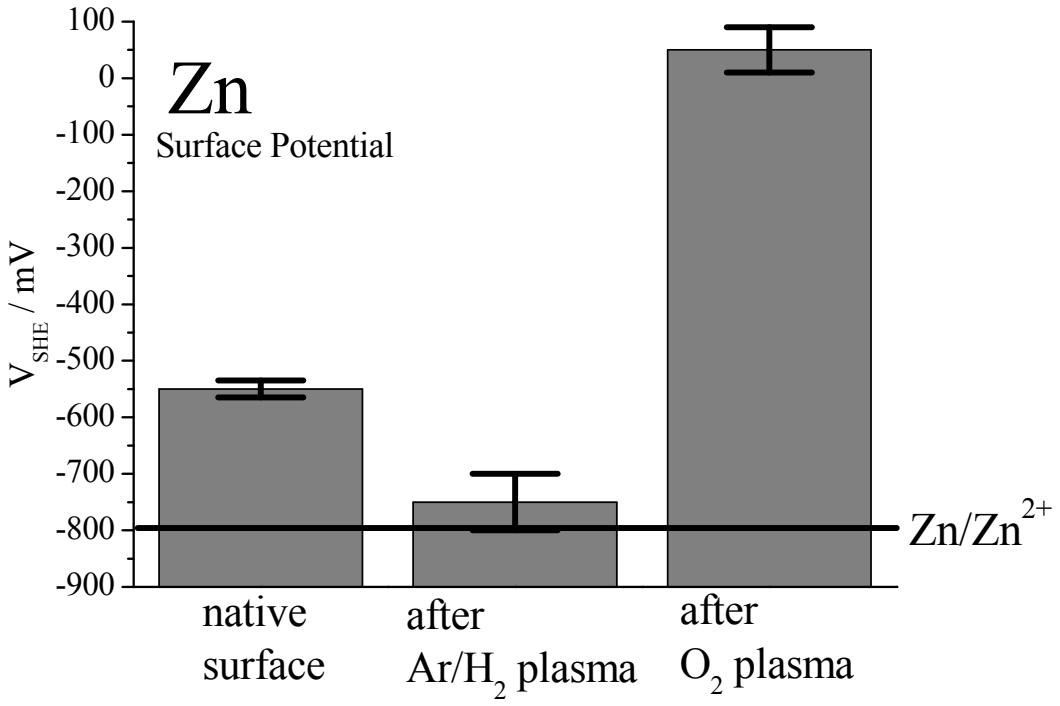


*Figure 21: Mean surface potentials of a HDG surface after alkaline cleaning, argon/hydrogen-plasma treatment and after oxygen plasma treatment measured in vacuum by means of Kelvin probe.*

The formation of the insulating zinc oxide passive films by the oxygen plasma treatment results in a further oxidation of Zn and $Zn^{+}$ donor states to $Zn^{2+}$ in the passive film as shown in Figure 22.

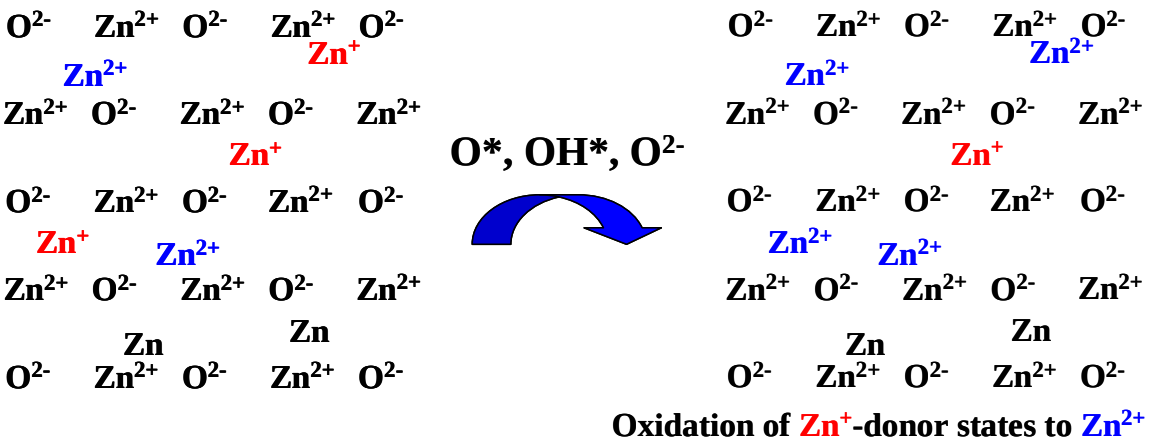


*Figure 22: Schematic lattice structure of zinc oxide for the oxidation of interstitial Zn+ ions due to plasma oxidation.*

This further oxidation leads to the observed anodic shift of the Volta potential according to the interpretation of plasma oxidation of iron surfaces by Grundmeier and Stratmann [14]. Equation 20 suggests an increase of the Volta potential difference between the non-modified and plasma modified state due to the lowering of the $Zn^+$-density in the passive film.

$$\Delta\left(\Delta\Psi_{Ox}^{Ref}\right) = \frac{RT}{F} \cdot \ln\left(\frac{a_{Zn^+}(\text{native surface})}{a_{Zn^+}(\text{plasma ox.})}\right) \tag{20}$$

$\left(\Delta\Psi_{Ox}^{Ref}\right)$ is the Volta potential difference between the vibrating reference electrode and the oxide surface and $a_{Zn^+}$ is the $Zn^+$ activity respectively in the native or plasma oxidized zinc oxide surface.

The corresponding chemical reaction can be described as follows:

$$Zn_{ZnO}^{+} + OH^{\bullet}{}_{ads} \rightarrow Zn_{ZnO}^{2+} + OH_{ads}^{-} \tag{21}$$

The change of the surface potential due to a change in the surface dipole density and orientation is neglected in this consideration since the surface of the passive film is anyhow hydroxide terminated as shown by XPS measurements [1].

### 5.1.4 Stability of zinc surfaces after plasma modification

The electronic properties of the passive film after plasma modification strongly change in humid atmospheres. Figure 23 shows the Volta potential transient of an oxygen plasma treated zinc surface in humidified air (95% r.h.). The Volta potential shifts cathodically within minutes due to the change of the electronic properties of the passive layer. The adsorbed ultra-thin electrolyte layer promotes the dissolution of Zn ions into the aqueous phase.

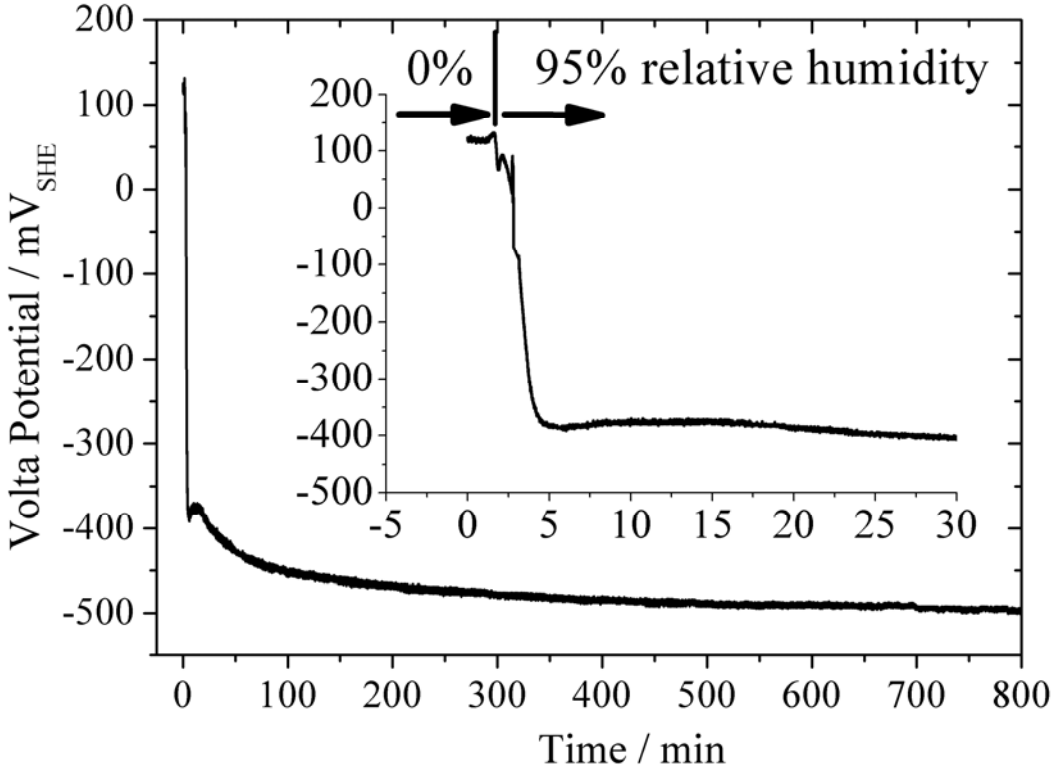


*Figure 23: In-situ Kelvin probe measurement of the relaxation of the Volta potential after oxygen plasma measured in dry air and switching from 0 to 95% relative humidity.*

The increased electric field in the passive film then leads to a further oxidation of Zn to $Zn^+$ at the oxide/metal interface. The passive film thereby readjusts its chemical composition to the state which is given under the condition of atmospheric conditions with lower oxygen activity in comparison to the oxygen plasma.

These results show that zinc oxide films with low donor densities prepared by oxygen plasma treatment cannot be stabilised in the presence of atmospheric water activities.

## 5.2 Deposition of ultra-thin plasma polymer films

Since highly oxidised zinc oxides are reduced again in humid atmospheres leading to increased donor densities, an insulating film is required to inhibit the transfer of electrons to surface adsorbed oxygen molecules.

This concept takes into account that the donor density of the oxide and thereby its electronic conductivity is high and that the insulating properties of the oxide/plasma polymer are

provided by the ultra-thin plasma polymer film. These ultra-thin $SiO_2$-like plasma polymer films there are well known due to their barrier properties [50, 52, 86].

### 5.2.1 In-situ FT-IR analysis after plasma deposition

Figure 24a and b show a FT-IRRAS spectrum of a $SiO_2$-like film after 20 s film deposition from a mixture of HMDSO and oxygen. Both regions show the carbon free deposition of the films indicated by the negative vibration band for $CH_{2,3}$ at 2850-2900 $cm^{-1}$ as the negative peaks for $CH_{2,3}$ occur due to the removal of organic contaminations on the reference sample. The asymmetric Si-O-Si stretching vibration with the main peak at 1232 $cm^{-1}$ is a mixture of transverse optical and different longitudinal optical modes which originate from the angle of incidence of the polarized laser light. Silica-like structures are represented by the Si-O-Si peak at 1170 $cm^{-1}$ and a small shoulder at 1070 $cm^{-1}$. The free dangling OH-groups can be attributed to the peak at 3600 $cm^{-1}$ whereas water which is adsorbed at the surface and incorporated in voids of the film during plasma deposition gives rise to the broad absorption at 3300 and 3520 $cm^{-1}$ [91].
All peaks assignments are listed in Table 3.

*Table 3: Assignment of the FT-IRRAS peaks after deposition of $SiO_2$-like film.*

| Wavenumber ($cm^{-1}$) | Group | Assignment | Ref. |
|---|---|---|---|
| 820 | Si-O-Si | δ(Si-O-Si) | [52] |
| 921 | Si-OH | $\nu_s$(Si-OH) | [52, 62] |
| 1070 | Si-OH | $\nu_{as}$(Si-OH) | [62] |
| 1170 | Si-O-Si | $\nu_{as}$(Si-O-Si) | [52] |
| 1232 | Si-O-Si | $\nu_{as}$(Si-O-Si) | [52, 62] |
| 2850-2900 | $CH_2$, $CH_3$ | $\nu_{as,s}(CH_x)$ | [88] |
| 3300 | $H_2O$ | $\nu_s$(OH) | [87, 89] |
| 3520 | $H_2O$ | $\nu_{as}$(OH) | [87, 89] |
| 3600 | Si-OH | ν(OH) | [91] |

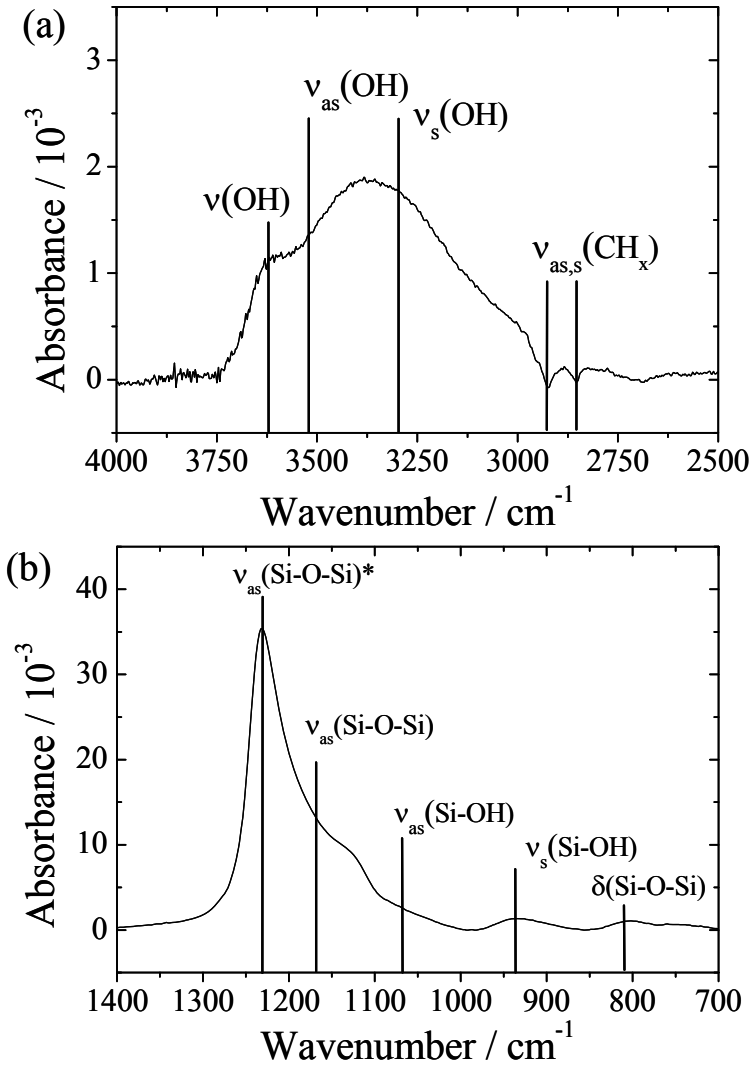


*Figure 24: FT-IRRAS difference spectrum of an ultra-thin insulating $SiO_2$-like film on an alkaline cleaned HDG after oxygen plasma cleaning and film deposition for two wavenumber regions: (a) 4000 - 2500 $cm^{-1}$ and (b) 1400 - 700 $cm^{-1}$ (reference: state after alkaline cleaning).*

### 5.2.2 Chemical composition of plasma polymer films

The XPS depth profiling in Figure 25 shows in detail, that the chemical composition of such inorganic plasma deposited films differs from pure $SiO_2$ layers. The oxygen excess which can be observed over the whole layer thickness can be explained by the formation of OH-dangling groups and the adsorption of water molecules at the outer film surface and at interfaces within the film due to the network structure with voids and defects. The depth profile also proofs the carbon free film deposition as well as the existence of the zinc oxide/hydroxide layer between the zinc and the $SiO_2$-like film.

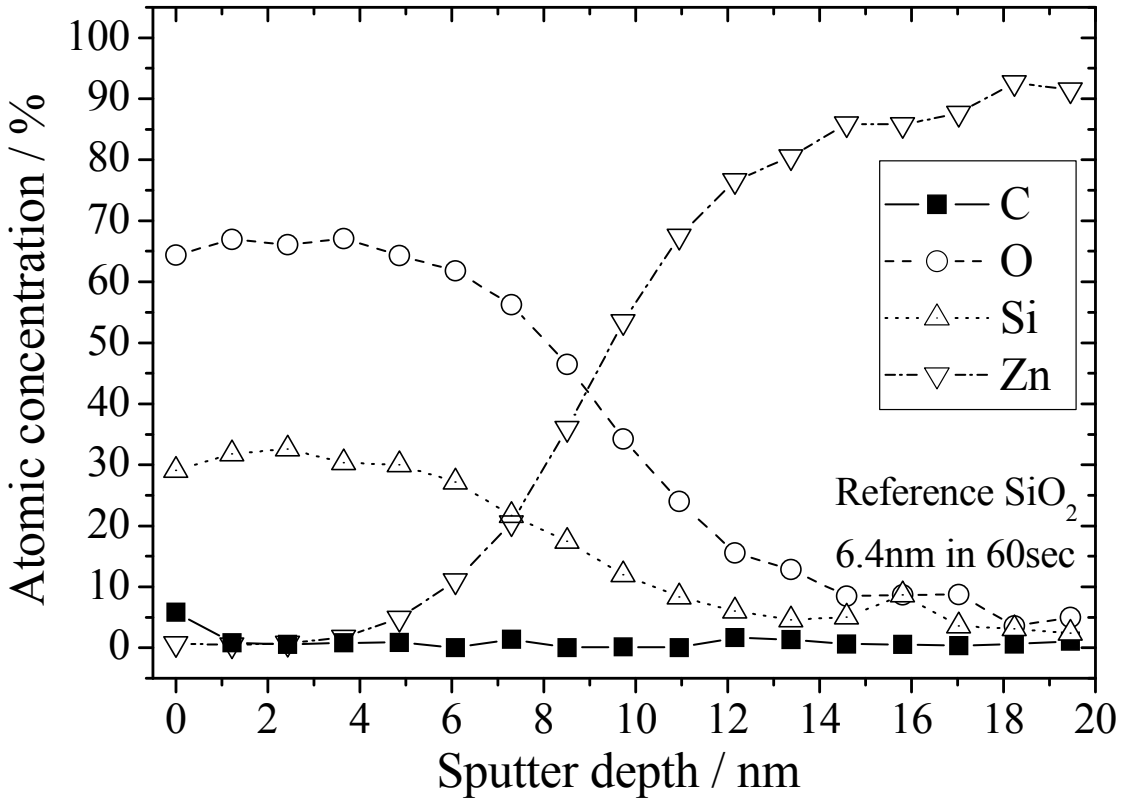


*Figure 25: XPS sputter profile of a 10 nm thin $SiO_2$ film on alkaline cleaned HDG.*

### 5.2.3 Change of surface structures after film deposition

To get information on the film morphology AFM images were measured on selected single grains of the Zn-alloy after the alkaline cleaning (Figure 26a) and after deposition of a 10 nm $SiO_2$-like film (Figure 26b). The wavy structure (nanometre scale) on the alkaline cleaned HDG steel is formed during the cooling process after the hot-dip galvanising process [1]. The alkaline cleaning results in the removal of the surface aluminium layer and leads to etch grooves with nanometre depth [1]. The deposited 10 nm thin $SiO_2$-like film perfectly imitates and covers these etch grooves and moreover partly levels the original wavy structure. However, nanometre and sub-nanometre sized defects within the $SiO_2$-like film cannot be observed by such an AFM-measurement.

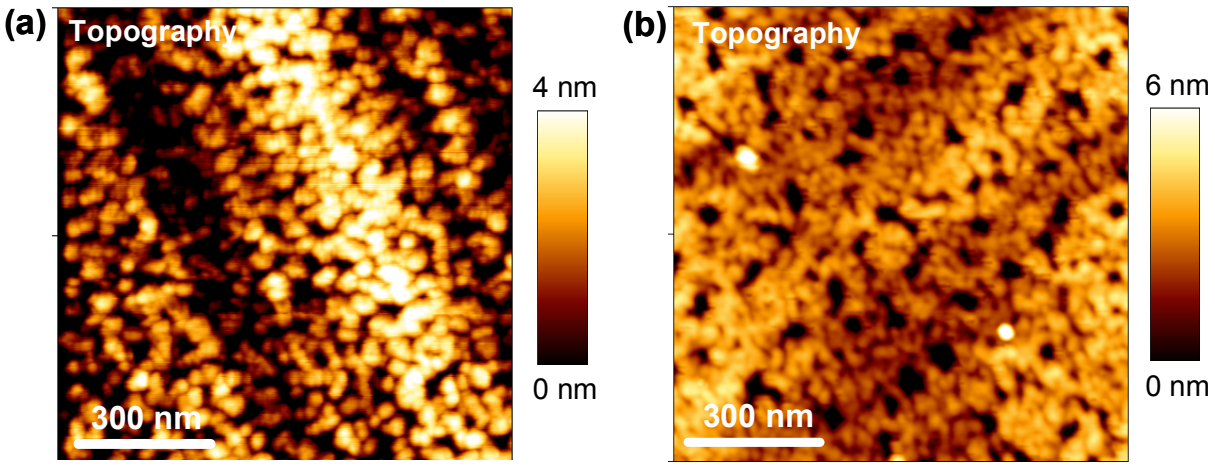


*Figure 26: AFM measurements of the topography of (a) an alkaline cleaned HDG surface and (b) the same surface covered with a 10 nm thin $SiO_2$ film.*

## 5.3 Barrier properties of $SiO_2$-like films for different film thickness values

While the FT-IRRAS, XPS and AFM measurements reveal the composition and morphology of the $SiO_2$-like film, the barrier properties of this ultra-thin layer has to be proven by electrochemical methods as it not possible to detect nanosized defects in the layer directly with spectroscopic and microscopic measurements.

### 5.3.1 Surface coverage for different film thickness values

Hence, additional electrochemical measurements were carried out to determine the ratio between covered and uncovered surface. Cyclic voltammetry (CV) allows the measurement of the Zn oxidation and reduction current densities which can be related to the coverage of the oxidised zinc surface [78, 79]. Results of the corresponding CV measurements are shown in Figure 27 for a bare oxide covered zinc surface, as well as for three different film thickness values of the $SiO_2$-like film. For the bare zinc surface the area of the Zn reduction peak (-1.04 V versus SHE) and the Zn oxidation peak (-0.80 V versus SHE) are clearly visible. Already a 10 nm thin $SiO_2$-like film inhibits the zinc reduction and oxidation almost completely as it can be seen in the inset of Figure 27 (small inset: y-axis magnified by 2 orders of magnitude). The cyclic voltammograms could be repeated several times without a measurable increase in the measured current densities. The resulting current densities are further reduced with increased film thickness which shows that small defects at 10 nm film thickness are diminishing at film thickness of several ten nanometres.

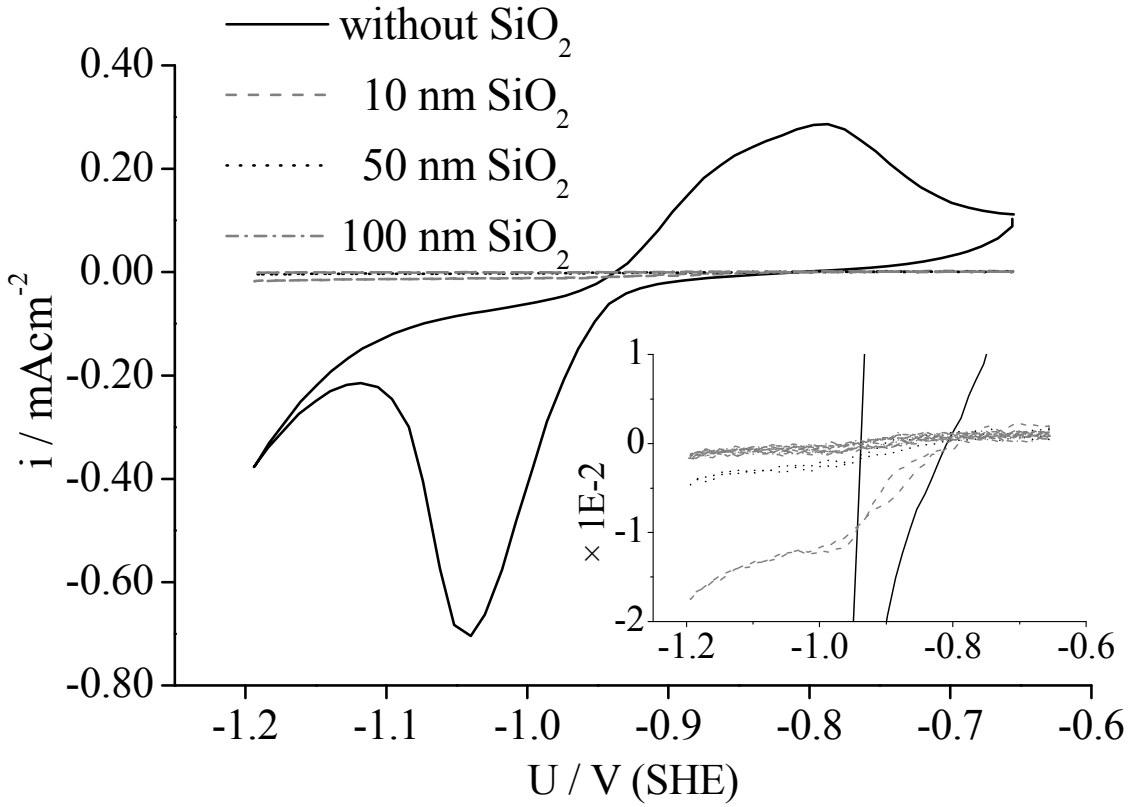


*Figure 27: Cyclic voltammograms on alkaline cleaned HDG (continuous line) and with plasma polymers on top with thickness values of 10 (dashed line), 50 (doted line) and 100 nm (dashed-doted line).*

For the plasma polymer film covered surfaces no CV peak analysis could be performed. However, the estimated uncovered area is below 0.5% already at 10 nm film thickness.

The non-vanishing slope of the curve for the 10 nm thin film in the cathodic region shows that very low oxygen and hydrogen reduction current densities are still possible in nanoscopic pinholes. However, in comparison to the bare oxide covered zinc surface the electron transfer reactions are significantly inhibited.

### 5.3.2 Barrier properties - pore and film resistance

Electrochemical impedance spectroscopy (EIS) measurements proved the existence of nanoscopic pores in the deposited films as shown in Figure 28a and b. For ultra-thin film coated surfaces, two different time constants can be observed at 10 and 5000 Hz. The decrease of the film capacitance values with increasing film thickness confirms the barrier properties of the insulating films. The pore resistance below 1 Hz is increasing with film thickness, but even the value for the 10 nm film is one order of magnitude higher than for the

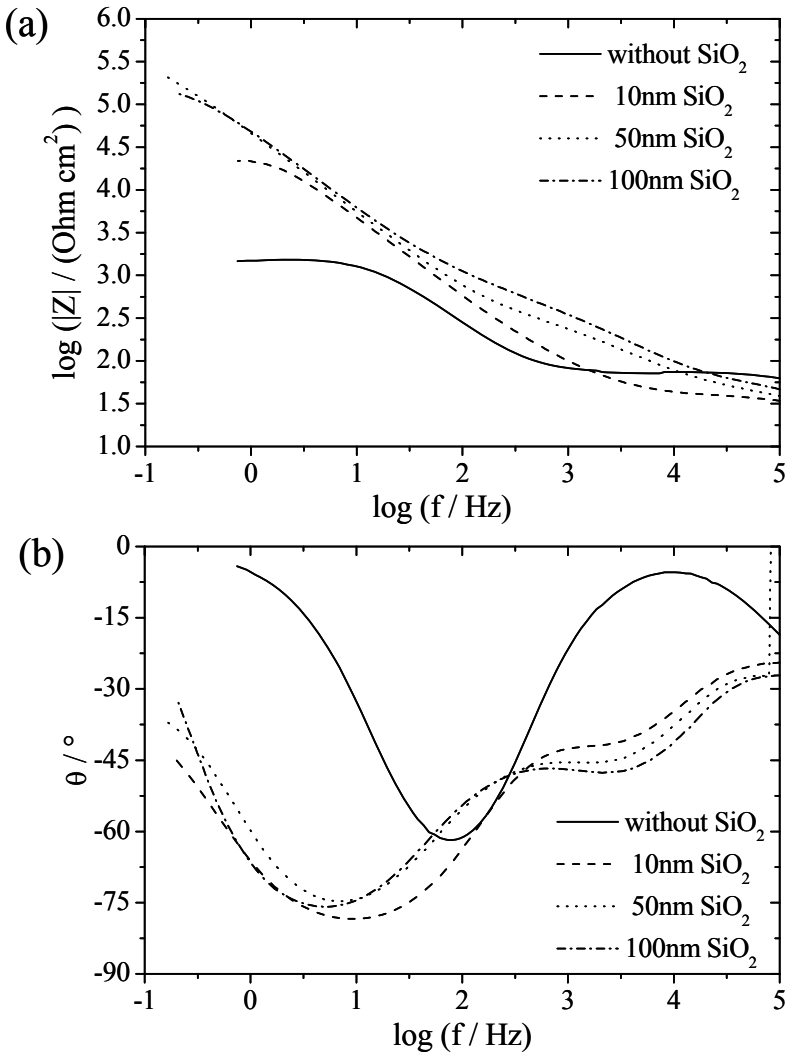


*Figure 28: Electrochemical impedance spectroscopy on alkaline cleaned HDG and with plasma polymers on top with thickness values of 10, 50 and 100 nm: (a) impedance and (b) phase.*

uncovered HDG steel which indicates that these ultra-thin films form an efficient barrier for the aqueous electrolyte. For all films the existence of nanoscopic pinholes were confirmed by EIS measurements as the phase $\vartheta$ would be around ~|90°| for perfect barrier coatings and the impedance curve could be expressed by a straight line of slope -1 in the log(|Z|)/log(f) plot. However, for the application as interfacial films between the metal and an organic coating these few pinholes are not influencing the corrosion resistance.

## 5.4 Influence of intact $SiO_2$-like films on unformed zinc surfaces

Klimow et al. observed a correlation between the inhibition of the oxygen reduction at the interface and the cathodic shift of the surface potential on conversion chemistry treated zinc surfaces of galvanised steel [2]. This result could be also connected to a decreased progress of cathodic de-adhesion processes at the interface. To reveal, if similar mechanisms are effective for $SiO_2$-like plasma deposited ultra-thin layers, the influence of $SiO_2$-plasma polymers on the interfacial ion transport kinetics and their effects on the interface potential has been investigated by the SKP.

### 5.4.1 Kelvin probe analysis in vacuum and humid atmospheres

In Figure 29 the change in the Volta potentials directly after film deposition, previous oxygen plasma cleaning and the untreated HDG surface are shown as measured in-situ by means of the Kelvin probe in vacuum. A strong anodic shift after the oxygen plasma treatment of +600 mV was observed and assigned to the oxidation of the interstitial Zn and $Zn^+$ donor states to $Zn^{2+}$ [14].

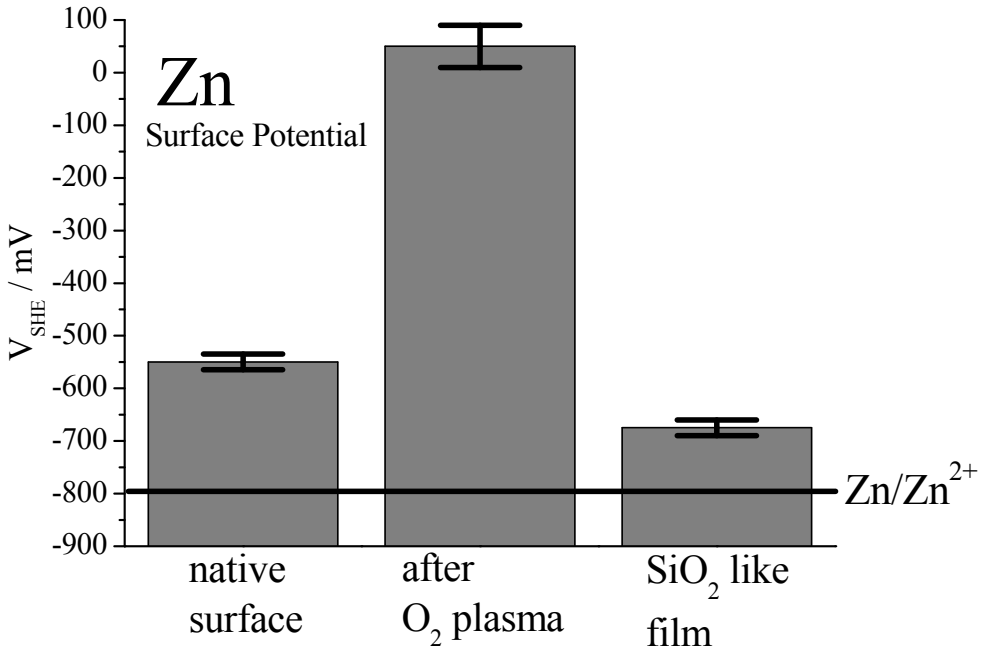


*Figure 29: Mean surface potentials of a HDG surface after alkaline cleaning, oxygen plasma treatment and 10 nm $SiO_2$ film deposition measured in-situ in vacuum by means of Kelvin probe.*

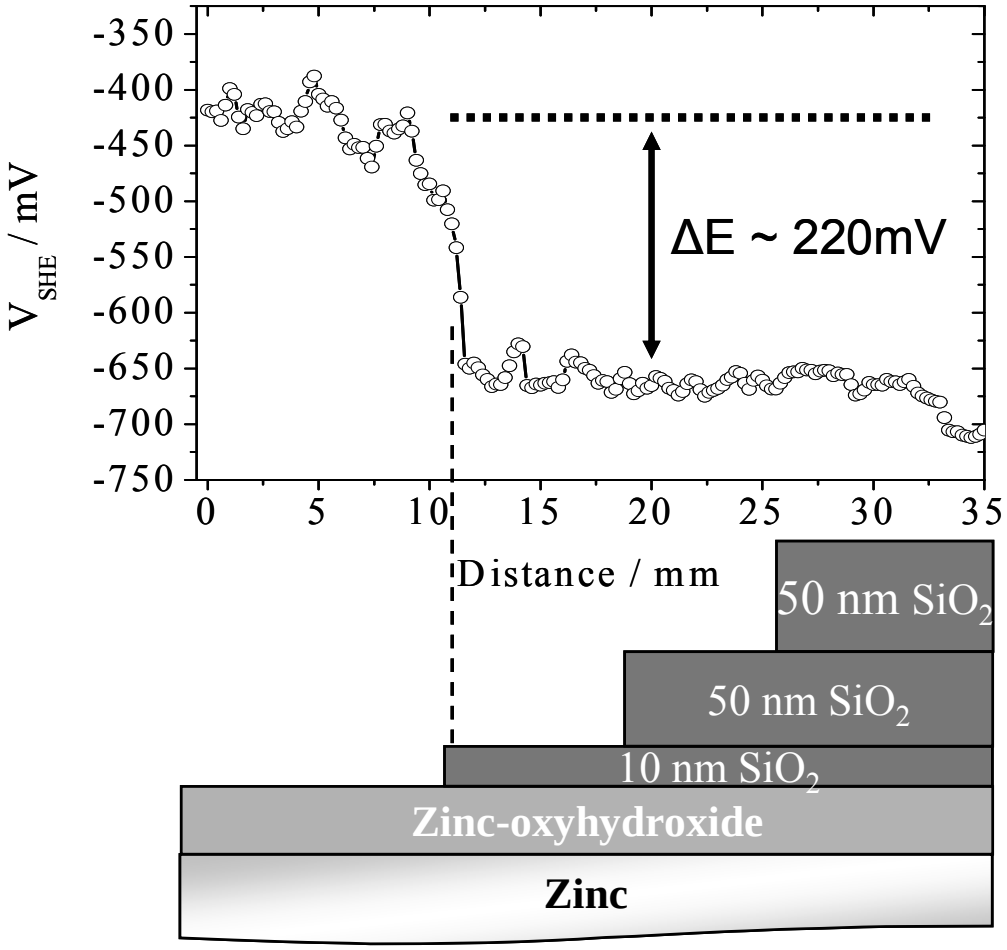


*Figure 30: Ex-situ height regulated scanning Kelvin probe line scan of HDG surface with thickness step-gradient of $SiO_2$-like film measured in $O_2$ atmosphere with high humidity (95% r.h.).*

After 10 nm $SiO_2$-like film deposition, the surface potential was shifted 175 mV cathodically in comparison to the native surface and thereby 675 mV cathodically in comparison to the just plasma oxidised surface. By increasing the $SiO_2$ film thickness to 60 or 110 nm, no further decrease of the surface potential could be observed as shown in Figure 30, as the potential stayed constant for film thickness values of 10, 60 and 110 nm.

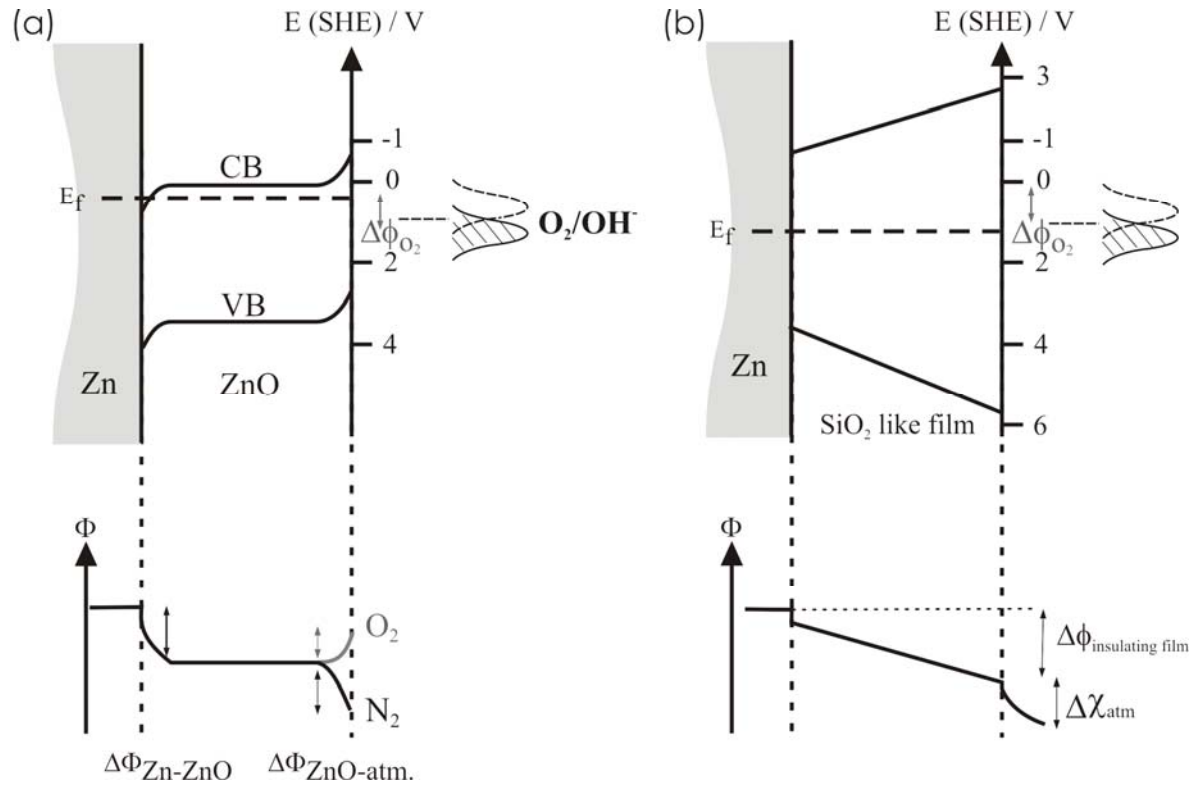


*Figure 31: Schematic band structure of a Zn surface covered with the corresponding n-semiconducting oxide (a) or an insulating $SiO_2$-like film (b) (following [92, 93]).*

The oxygen reduction at the surface of the zinc oxide leads to a band bending of the valence band due to the depletion of the electrons at the surface in oxygen containing environments. This depletion is already completely inhibited by the insulating properties of the 10 nm $SiO_2$-like film and leads to the cathodic shift of the Volta potential.

Figure 31 illustrates the experimentally observed potential distributions and the particular Galvani potential differences at the interfaces of the metal/metal oxide structures. The electronic properties of the oxides are either n-semiconducting for the ZnO layer or insulating for the $SiO_2$-like film. In the case of the n-semiconducting ZnO layer and for the electronic equilibrium between the metallic zinc and its oxide, the Galvani potential differences at the interfaces between metal/metal oxide and metal oxide/humid atmosphere are strongly determined by the presence of molecular oxygen [92]. In the case for the zinc oxide, the relative position of the energy levels of the conduction band and the electronic terms of oxygen allows an electron transfer to reduce oxygen at the surface and to form surface states which shifts the potential distribution at the outermost interface.

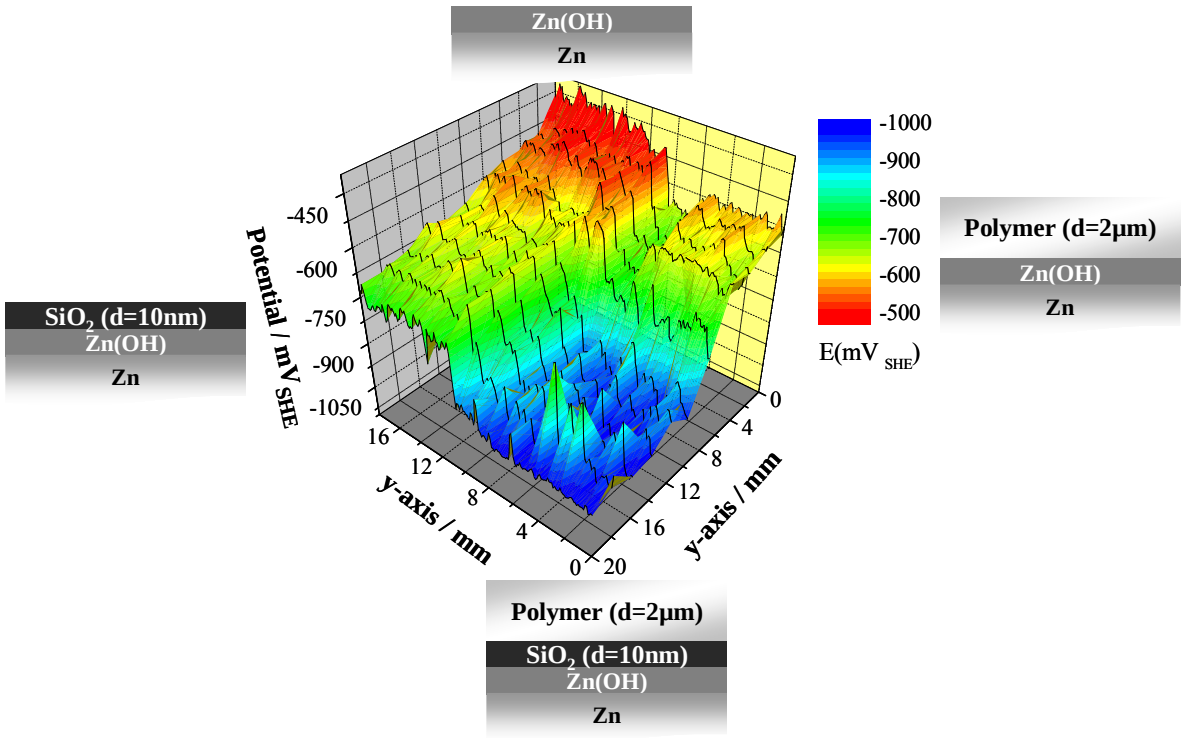


*Figure 32: Ex-situ height regulated scanning Kelvin probe potential mapping of an alkaline cleaned HDG sample with four different surface configurations in oxygen atmosphere (95% r.h.).*

$SiO_2$ is an insulating material with a band gap $E_g$ of about 9.0eV [94] which inhibits the electron transfer to the oxygen states located at the $SiO_2$ surface. For perfect barrier films in the ideal case, the calibrated Volta potential difference $\Delta\Psi_{Ref}^{SiO_2}$ between the sample covered with the insulating $SiO_2$-like film and the reference probe is expected to be independent from the prevailing atmosphere and very close to the electrode potential of the $Zn/Zn^{2+}$ electrode.

According to the hypothesis that the applied interfacial potential, due to the electrolytic connection between the polymer/metal interface and the corroding defect, drives the interfacial oxygen reduction kinetics and thereby the cathodic de-adhesion process [2] it is interesting to measure the adjusted interfacial potentials after the coverage of the modified surfaces with an organic film.

Therefore, a sample with four different surface configurations was prepared. The Volta potential mapping of the surface of measurement of such a sample in humid oxygen containing atmosphere (95% relative humidity) by means of the height regulated scanning Kelvin probe is displayed in Figure 32. The respective potentials as a function of the interface chemistry can be directly observed by comparing the four quadrants of the sample.

By applying the organic polymer film, the resulting interface potential is shifted cathodically. As the possibility to reduce oxygen correlates with the measured Volta potential, the occupation of possible oxygen reduction sites by polymer chains results in a decreased oxygen reduction at the zinc oxide/polymer interface. Moreover, the micrometer thick polymer film decreases the activity of oxygen at the interface. This leads to the cathodic shift of the Volta potential in comparison to the bare zinc oxide surface. Due to the insulating $SiO_2$-like film, the combination of the $SiO_2$-like film with the organic polymer system leads to the strongest cathodic shift of the Volta potential as the oxygen reduction is synergistically minimized.

### 5.4.2 Corrosion processes and kinetics during the de-adhesion processes in corrosive environments

Cathodic delamination in oxygen containing humid atmosphere is based on the de-adhesion of polymer films from iron or zinc substrates [46, 95-99]. Oxygen reduction at the polymer/oxide interface leads to an oxidative degradation of the polymer and increased interfacial pH-values. This local cathode is electrolytically connected to the corresponding anodic metal dissolution in the defect area, which is the local anode. To compensate the generated negative interfacial charge, hydroxide ions are transported to the defect whereas cations from the defect electrolyte enter the polymer/oxide/metal interface and are transported to the front of de-adhesion [100, 101].

Figure 33a shows the averaged line scan of the cathodic delamination for the zinc surface of the HDG samples coated with a 2 µm polymeric coating and a defect filled with 0.5M NaCl as electrolyte. The x-axis represents the distance to the filled defect. After 3 hours the delamination front is detected in the line scans as a potential difference between the intact area (interface potential = -650 mV) and the defect coupled potential (-1100 mV) and propagates along the zinc oxide/polymer interface. The speed of this propagating delamination front is about 800 µm/h and slows down with increasing distance from the defect.

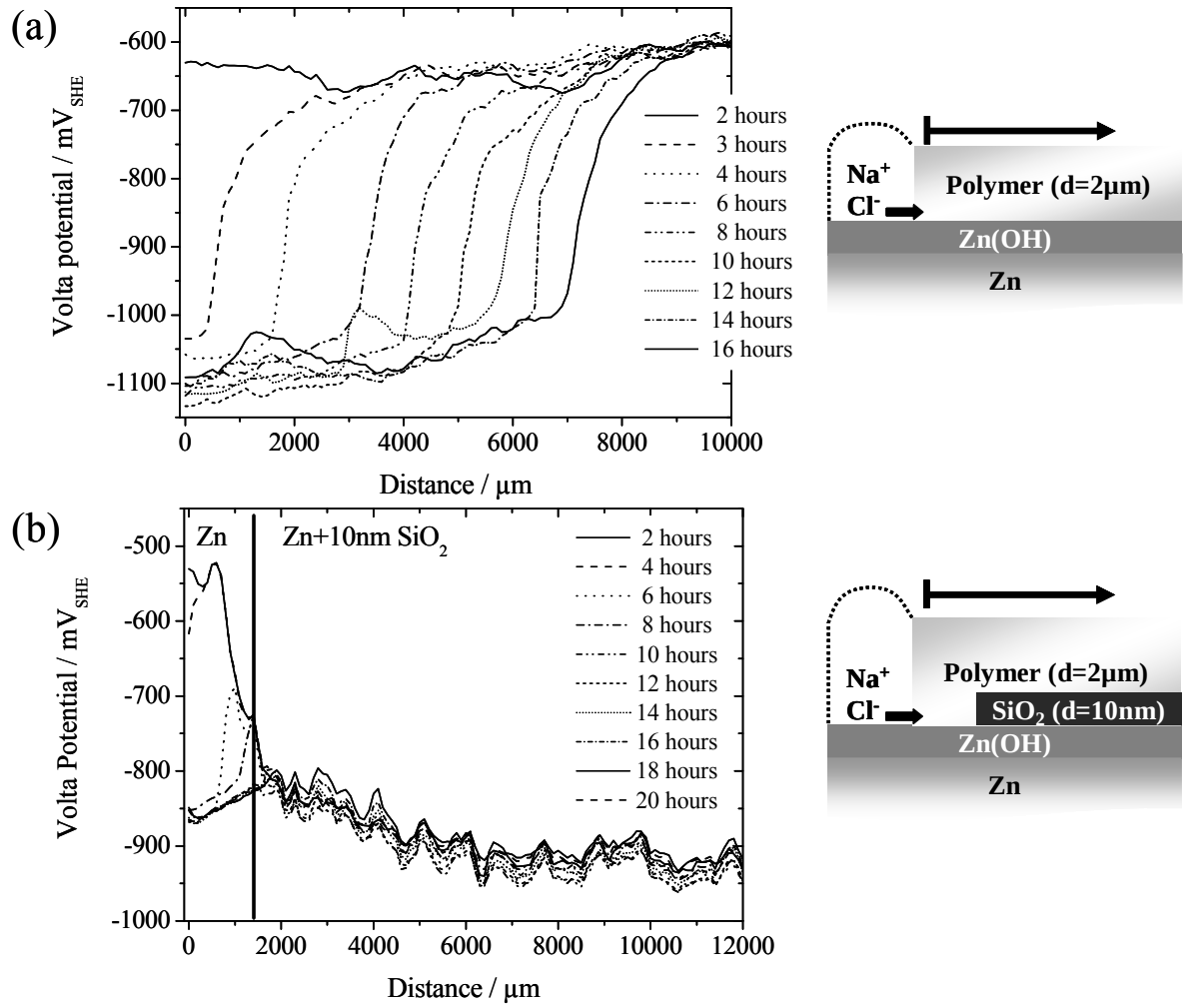


*Figure 33: Height regulated scanning Kelvin probe line profiles of corrosive de-adhesion on (a) alkaline cleaned HDG and (b) with 10 nm $SiO_2$ coating for x > 1600 µm.*

In Figure 33b the averaged line scans for a sample with a 10 nm interfacial $SiO_2$-like film is shown. The $SiO_2$-like film was deposited on the sample for distances to the defect larger than 1600 µm. The anodic shift (-350 mV) caused by the deposition of the $SiO_2$-like film is clearly visible in comparison to the uncovered zinc surface for distances to the defect smaller than 1600 µm. When the cathodic delamination on zinc reaches the $SiO_2$-like film the de-adhesion process stopped and the potential step vanished, as the potential difference between the defect and the $SiO_2$ coated area becomes nearly zero. As shown by the HR-SKP measurement, the effective inhibition of the oxygen reduction at the intact oxide/$SiO_2$/polymer interfaces leads to a strong inhibition of the cathodic de-adhesion process and to a diminishing potential difference between the intact area and the corroding defect which could act as a driving force for the de-adhesion process.

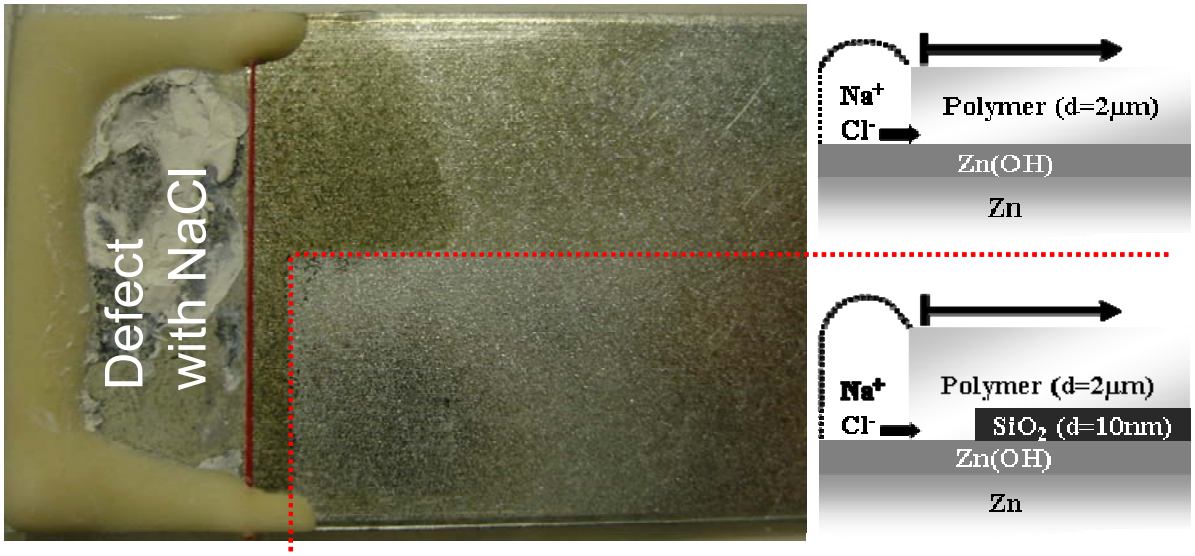


*Figure 34: Microscopic picture of an alkaline cleaned HDG sample partially covered with 10 nm $SiO_2$ after 38 hours delamination.*

Figure 34 shows the microscopic picture of an alkaline cleaned HDG sample with partial coverage of a 10 nm $SiO_2$-like film in the lower half and a polymeric top coating on the whole sample after 38 hours with activated defect (left part). The corrosive de-adhesion propagating away from the defect in the upper part on the pure zinc surface can be clearly seen due to the darkening of the surface due to the formation of zinc corrosion products. In the lower part the step between the pure zinc surface and the $SiO_2$ covered part is clearly visible as sharp edge, with no colour change on the intact $SiO_2$ surface as no zinc corrosion products are formed. Moreover, peel tests proved that no de-adhesion of the polymer film from the $SiO_2$-surface occurred.

### 5.4.3 Influence of $SiO_2$-like films on the cathodic protection of iron by zinc coatings

A very fast corrosive de-adhesion of the polymer was observed for zinc coated steel in the previous chapter. In that case the local anode for the corrosive de-adhesion was formed by the dissolution of zinc in the defect area. On HDG steel not only the zinc surface but also the iron of the steel can be exposed to corrosive environments.

The cathodic protection of iron is based on the formation of a galvanic element between zinc and iron if the surfaces are exposed to corrosive environments [31]. The iron is protected by

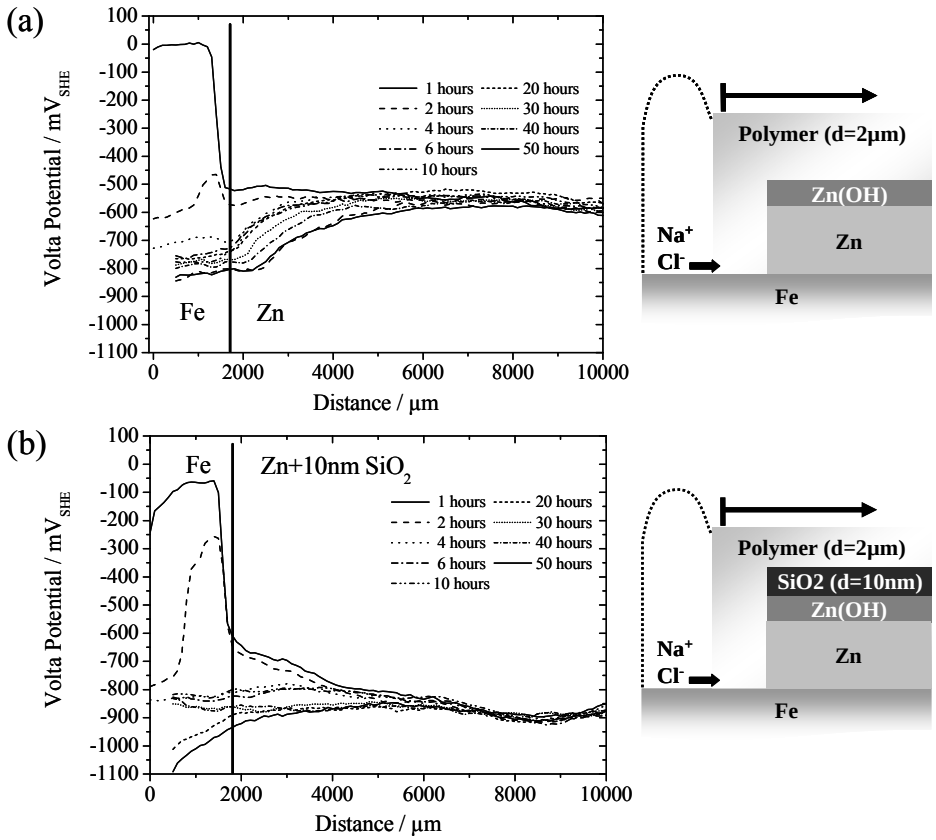


*Figure 35: Height regulated scanning Kelvin probe line profiles of corrosive de-adhesion on (a) alkaline cleaned HDG with the zinc coating etched down to steel and (b) with 10 nm $SiO_2$ coating on the remaining zinc surface for x > 1900 µm.*

the zinc coating due to a barrier effect (intact zinc coating) and the galvanic element in which zinc serves as sacrificial anode while steel acts as cathode.

A defect in the zinc coating was created by etching the zinc in the defect area with hydrochloric acid. Similar to the measurement in Chapter 5.4.2 the sample was coated with the organic polymer and partially coated with a 10 nm $SiO_2$-like film. Figure 35 shows the scanning Kelvin probe line profiles for both cases. In both cases, a galvanic element is formed between zinc and iron as the Volta potential shifts anodic (-800mV) when the corrosive de-adhesion front has reached the zinc coated surface. For the unprotected zinc surface a slow corrosive de-adhesion can be observed, whereas the $SiO_2$ covered zinc surfaces shows a stable interface between the $SiO_2$ and the organic layer.

Therefore, the barrier properties of the insulating $SiO_2$-like film stabilise the interface and slows the corrosive de-adhesion also for steel surfaces which have defects in the protective zinc coating.

## 5.5 Conclusions and model

Based on the presented results in this chapter, it became possible to establish a structure-property relationship that explains why highly corrosion resistant interfaces between polymeric films and zinc substrates can be achieved by means of plasma processes.
The barrier properties of the PE-CVD deposited $SiO_2$-like films correlate with the measured interface electrode potential, as the kinetics of oxygen reduction on the oxide surface determine the oxidation state of the oxide itself. Moreover, it is the Volta potential difference between an intact film and an active defect which reflects the driving force and therefore the rate for corrosive de-adhesion at the interphase of polymer coated $SiO_2$ film covered zinc surfaces.

The principal behaviour of the interfacial $SiO_2$-like film can be assumed to be representative for different highly crosslinked insulating films, e.g. such as Zr-oxide films.

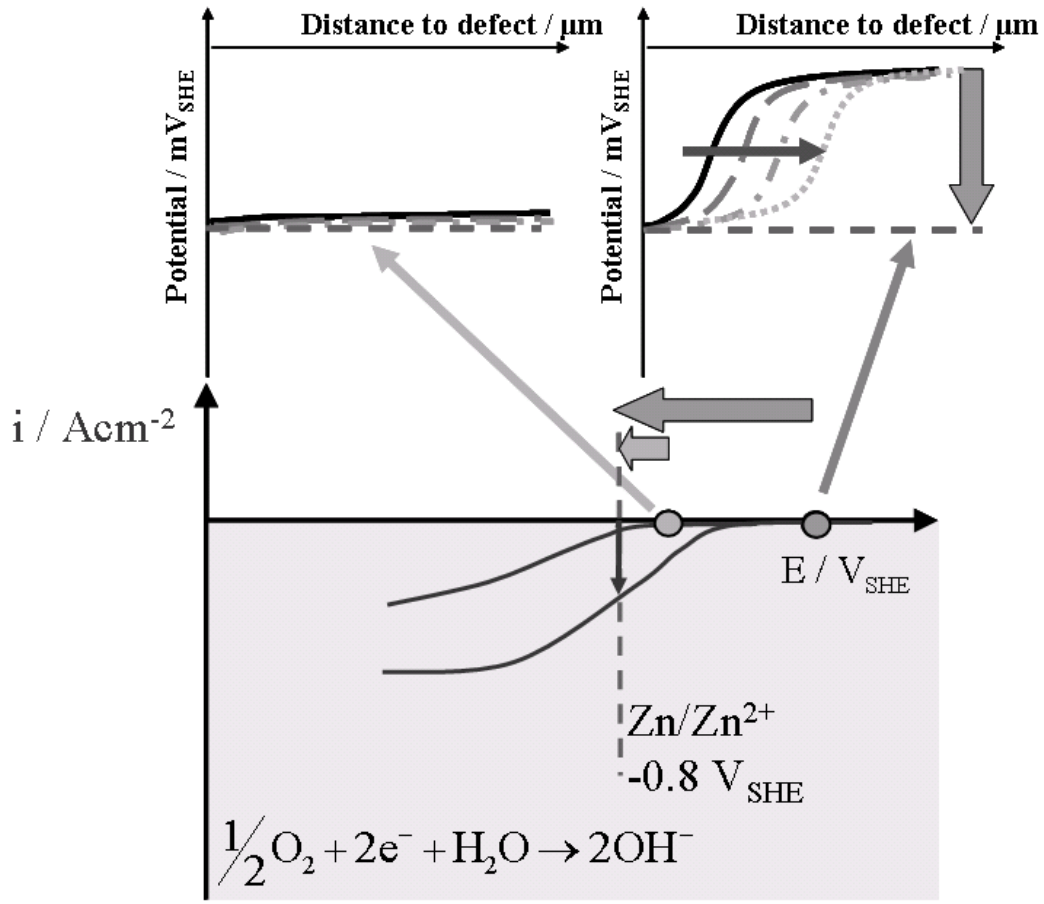


*Figure 36: Schematic principle of the oxygen reduction curve for the pure zinc and the $SiO_2$ covered zinc surface with a strongly reduced oxygen reduction current.*

Figure 36 illustrates the two different situations on the pure zinc surface and with the ultra-thin insulating 10 nm $SiO_2$-like film on top. Plotted are the current density curves for the oxygen reduction kinetics on zinc and the $SiO_2$-like film. The steady state for the oxygen reduction and oxide oxidation for the intact zinc oxide/polymer interface results in a large anodic overpotential in comparison to the potential of the active defect where zinc ions are dissolved. This overpotential represents the driving force for the cathodic delamination.

The insulating property of the $SiO_2$-like film effectively inhibits the oxygen reduction at the interface and therefore decreases the resulting current density which results in a very small overpotential. The measured potential difference between defect and intact area therefore gives direct information about the electron transfer reactions and as a consequence about the stability of the interface in corrosive environments.

# 6 Corrosion resistance of tensile formed plasma polymer films on HDG steel

In chapter 5 a correlation between the barrier properties of ultra-thin plasma polymer films and the corrosion resistance of hot-dip galvanised steel was established. Chapter 6 focuses on the influence of forming processes on the structure and functionality of interfacial ultra-thin $SiO_2$-like plasma polymer films on galvanised substrates.

Forming of thin film or organically coated metal sheets is one of the most important steps to generate functional products. The generation of forming induced defects is not only limited to defects in the protective inorganic [16-19] or organic [20] layers but also comprises defects in the galvanised substrates [21-24]. The formation of defects of brittle films on ductile substrates has been intensively studied both experimentally and theoretically [17, 25]. Usually, multiple sequential crack formation is observed for rather brittle films on ductile or high elongation substrates. By increasing the strain the number of cracks increases as well. This observation is explained by the so-called shear lag approximation presented in detail by Wojciechowski and Mendolia [16, 17].

Depending on the applied stress and strain different mechanism of the formed defects can be observed on pure zinc coated steel sheets [21-23]. Slip, twinning and cracking are the major deformation modes on zinc grains depending on the applied stress. Due to the hcp structure of zinc, basal slip is the easiest deformation mode in zinc and is therefore the predominant source for defects [26-28]. Twinning can be found on zinc grains if compressive and tension stress is applied simultaneously [21].

As it is well known from literature ceramic films can only be formed for less than 1% elongation. Plasma polymer films are intended to follow the deformation of the substrate due to their high cross-linking during plasma deposition [9-11, 29]. B. Baumert et al. reported that plasma polymer films show substrate induced defects for high forming degrees [24].

To acquire a deeper understanding of forming induced defects and to correlate the barrier properties of plasma polymer $SiO_2$-like films with the overall corrosion resistance, ex-situ and in-situ electrochemical measurements were combined with a miniature tensile testing device.

## 6.1 Forming of uncoated and coated HDG steel

### 6.1.1 Forming of uncoated HDG steel

Stretch forming of hot-dip galvanised steel leads to a grain orientation dependant change in the structure and orientation of the metal surface region. According to Lazik et al. slip, twinning and crack formation are the predominant modes to accommodate the strain states during forming of the zinc crystals and determine the structural changes of the crystal surfaces [21].

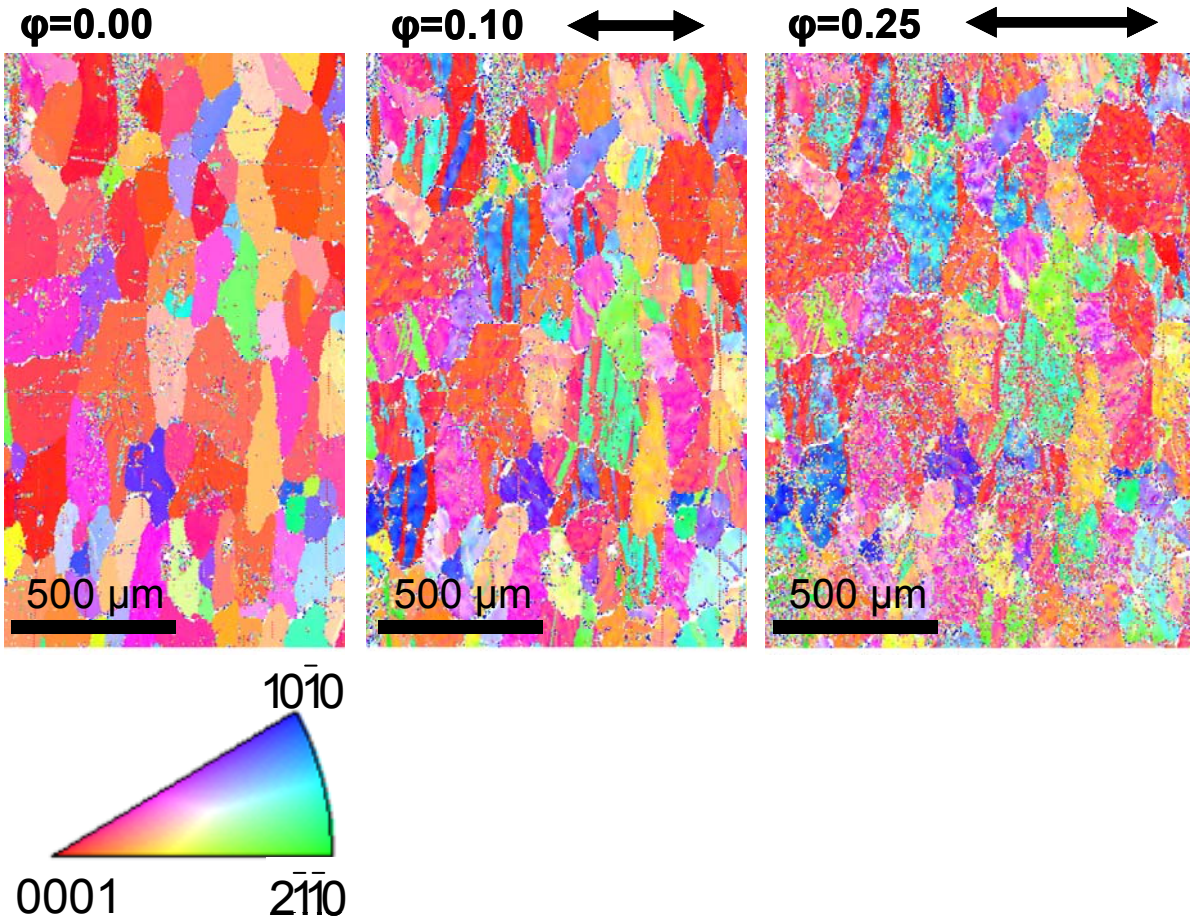


*Figure 37: EBSD grain orientation mapping before and after 0.1 and 0.25 uniaxial elongation of a HDG coated steel sheet. The uniaxial forming direction is indicated by the arrow. The grain orientation is indicated by the colours of the inverse pole figure. The lateral analysis spot size is 5µm.*

The EBSD analysis of the galvanised steel surface illustrates the different forming behaviour of the individual zinc grains (Figure 37). The typical grain size of the zinc coating is about 100 µm. Based on the hcp structure of the zinc grains, mechanical twinning and major basal slip planes could be identified as main forming effects for the grains with changed texture [21, 26-28]. The texture change of these grains is mainly perpendicular orientated to the strain direction. Further increase of the strain led to an enhanced turn over of the zinc crystal orientation.

### 6.1.2 Forming of thin $SiO_2$-like films on HDG steel

It can be expected from the structural change of the grains that a highly crosslinked thin $SiO_2$-like film is not able to follow elastically or plastically such a deformation but will lead to crack formation as shown by B. Baumert et al. for plasma polymer coatings on hot-dip galvanised steel according to the mechanism proposed by Wojciechoswski et al. [16, 17].
In Figure 38 the FE-SEM observation of the thin film coated substrate (film thickness: 50 nm) illustrates the typical cracking behaviour of the $SiO_2$ film on the surface of different grains and in the area of grain boundaries for different uniaxial forming levels. The orientation of the cracks inside the $SiO_2$ coating follows the orientation of slip bands.

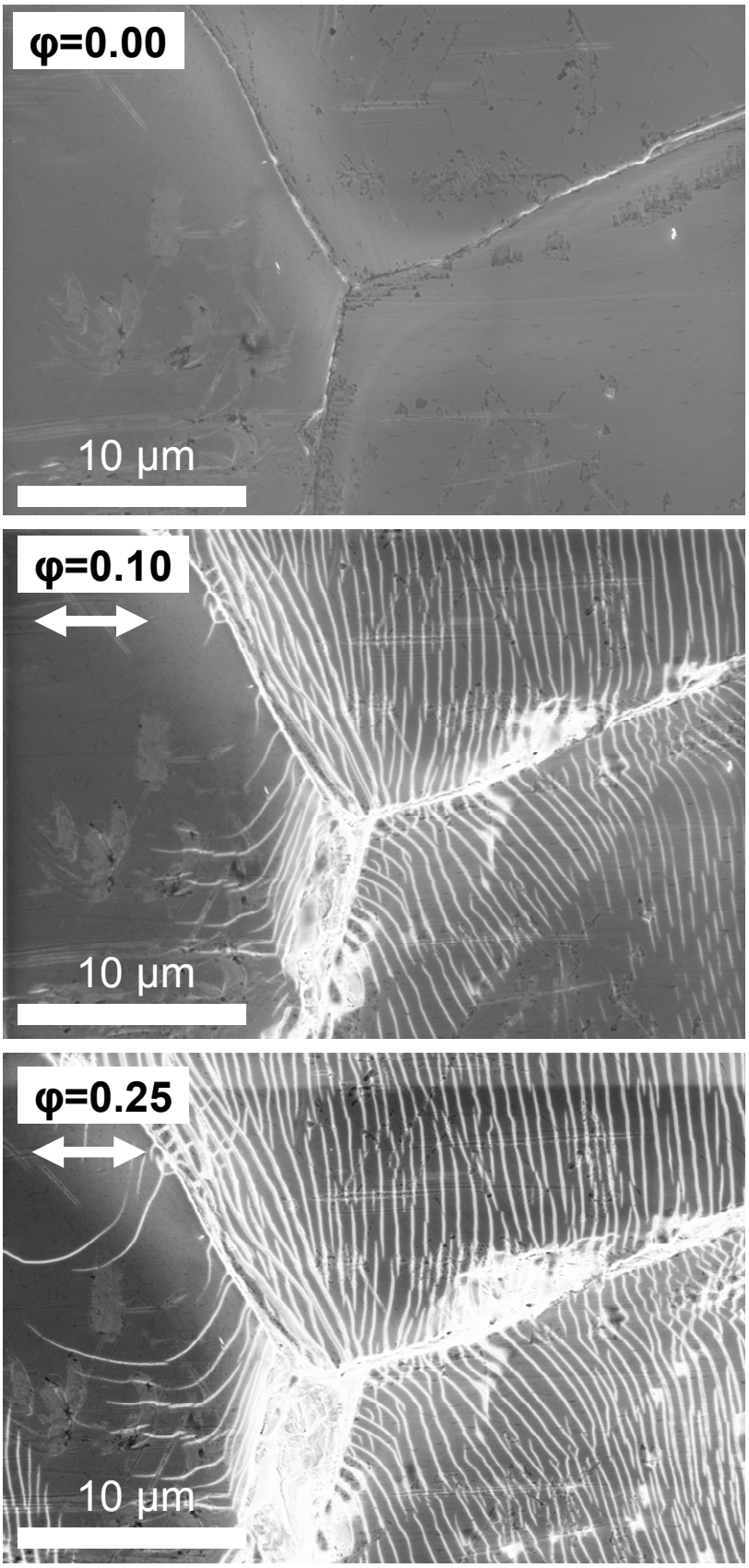


*Figure 38: FE-SEM pictures of a 50 nm $SiO_2$-like film on an alkaline cleaned HDG surface before and after 0.1 and 0.25 uniaxial forming. The uniaxial forming direction is indicated by the arrow.*

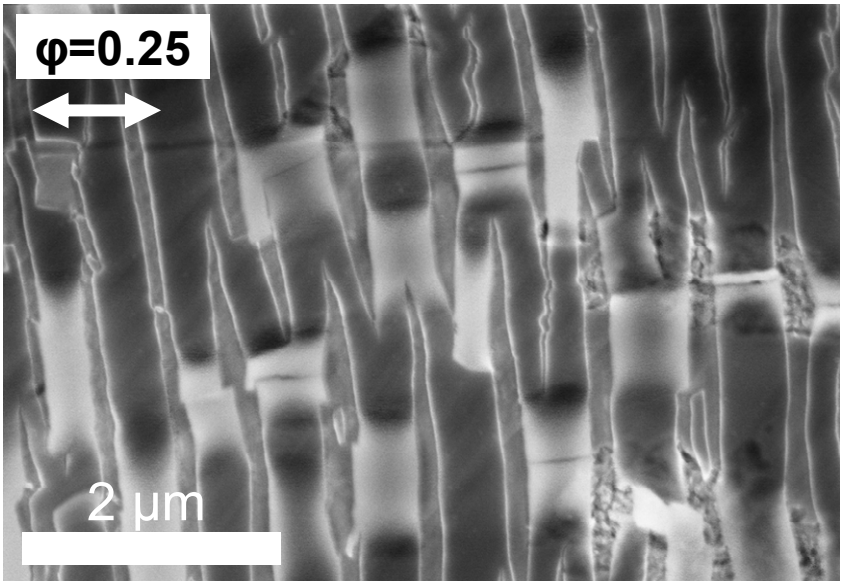


*Figure 39: FE-SEM pictures of a 50 nm $SiO_2$-like film on an alkaline cleaned HDG surface with 0.25 uniaxial forming. The uniaxial forming direction is indicated by the arrow.*

Close to the grain boundaries cracks tend to grow perpendicular to the grain boundary while the orientation changes to a common perpendicular orientation with regard to the direction of strain on the grain surface in several micrometer distance to the grain boundary. To compensate the strain between different grains, strain adjustment by activation of non-major slip planes takes place along the grain boundaries indicated by cracks with differing orientation [102].

According to the mechanism proposed by Kirk and Pilliar [72] the initial crack formation is strongly located at slip bands with an increase in crack density and an increase of the width of the cracks with increased strain. On fine gliding zinc grains with 50 nm $SiO_2$-like films, highly localised strains are distributed over the whole film thickness.
Figure 39 illustrates the situation in which the film with several tens of nanometres thickness only partly keeps adhered to the oxide covered substrate (dark areas) while de-adhesion occurs locally due to its cohesion strength (brighter areas). The approach of two neighbouring cracks stops at a certain distance which is in good agreement of the common crack theory because the local energy is not high enough to support both crack dissipations [17, 103].

### 6.1.3 Forming of ultra-thin $SiO_2$-like films on HDG steel

For smaller film thickness values of about 10 nm the de-adhesion process is less favourable compared to 50 or 100 nm thick $SiO_2$-like films, since less stress is built up inside the films before cracking occurs.

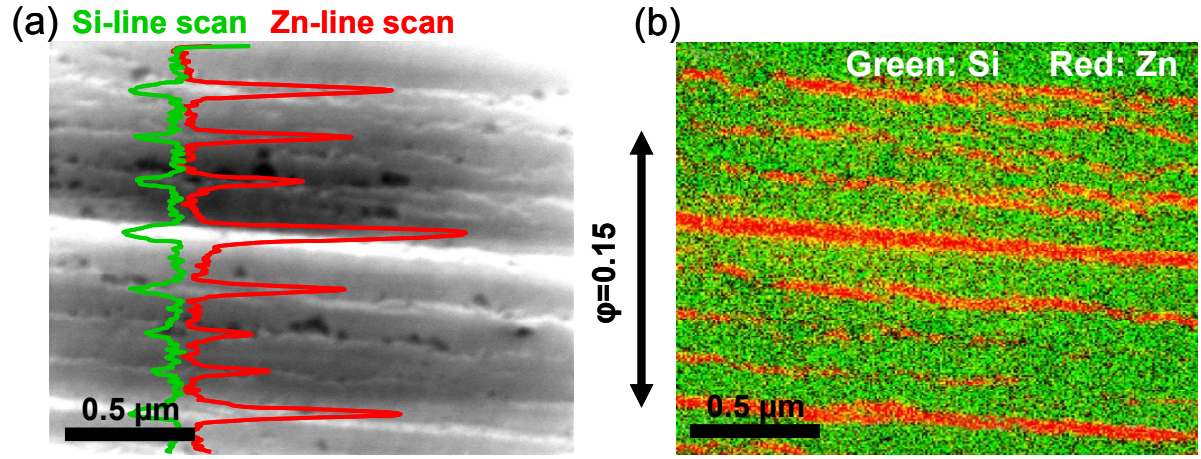


*Figure 40: (a) FE-SEM picture of a 10 nm $SiO_2$-like film after 0.15 uniaxial forming with a scanning Auger line scan overlay for Si (green) and Zn (red) and (b) with a scanning Auger colour overlay for Si (green) and Zn (red). The uniaxial forming direction is indicated by the arrow.*

For ultra-thin plasma polymer films Baumert et al. could show that small cracks are located at atomic scale slip lines [24]. Slip bands can be seen in Figure 40 for 10 nm thick $SiO_2$-like films with a spacing of 500 µm. Atomic scale slip lines can be observed between these major slip bands as thin parallel cracks inside the coating. The free zinc surface inside these cracks can be indentified by means of the scanning Auger electron spectroscopy surface mapping with colour overlay for Zn and Si. However, no de-adhered areas could be identified as contrast difference for the 10 nm film thickness by means of FE-SEM studies.

## 6.2 Barrier properties and corrosion resistance of $SiO_2$-like films after forming

### 6.2.1 In-situ cyclic voltammetry during stretch forming of thin film coated substrates

Ultra-thin plasma polymer films with film thickness of 10 nm in the unformed state strongly reduce the oxidation and reduction of the zinc surfaces as shown by cyclic voltammetric measurements in Chapter 5.3.1. Measurements which can provide information on the influence of forming on the electrochemical properties of ultra-thin films on HDG steel are usually very time consuming as each sample has to be formed individually.

By measuring in-situ cyclic voltammograms during the stretch forming process the full range of forming degrees can be covered in several ten minutes. Furthermore, statistical and measurement set-up errors are reduced since the measurement is performed on one single spot. The initial steps and the evolution of crack formation in ultra-thin plasma polymer films can be followed by calculating the free zinc surface as a function of the applied strain. The evaluation of the cyclic voltammograms was done based on the work of Schultze et al. [78, 79].

Figure 41a shows selected cyclic voltammetric measurements at different forming levels during stretching of the uncoated zinc surface. The zinc oxidation and reduction peak increases with increasing strain. As hydrogen evolution cannot be neglected for the zinc reduction peak, only the values of the maximum current density of the zinc oxidation peak were evaluated [78]. The measurement area itself was limited due to the capillary diameter and by this averages several grains and grain boundaries. The maximum current density of the zinc oxidation peak ($\max i_{ox}(Zn \mid ZnO)$) reached saturation values for $\varphi > 0.05$ as shown in Figure 41b.

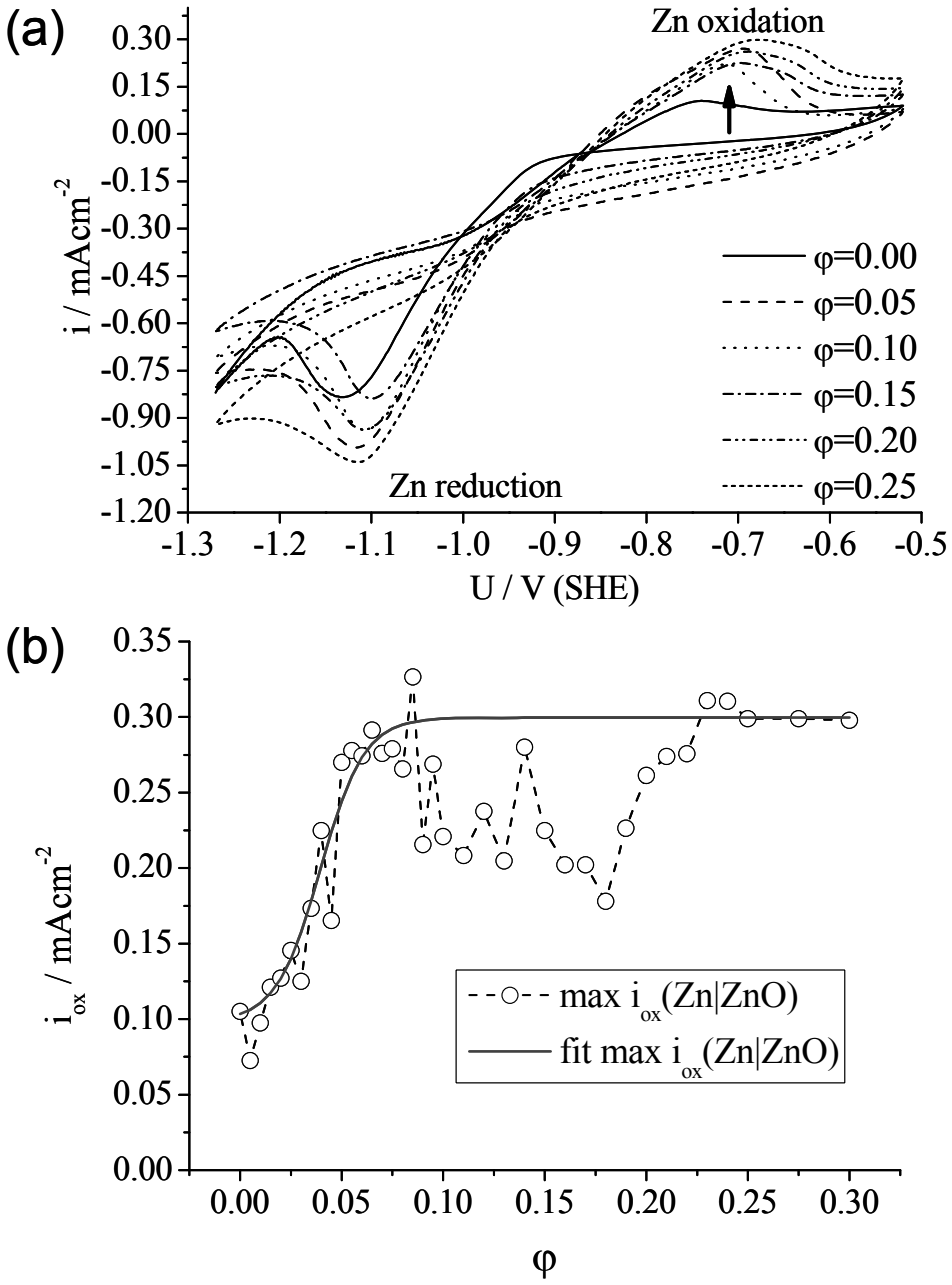


*Figure 41: (a) In-situ CV measurement of uncovered alkaline cleaned HDG steel during uniaxial forming. (b) Maximum oxidation current densities of zinc plotted versus the forming level.*

The increase of the maximum oxidation current density for the uncovered zinc is based on the creation of fresh zinc surface due to the forming induced increase of the surface. The large increase can be explained by the change of the smooth and planar surface in a 3-dimensional surface with atomic height steps, surface roughening and morphological changes especially at the grain boundaries.

Figure 42a shows selected cyclic voltammetric measurements at different forming levels during stretching of a 30 nm $SiO_2$-like film on the zinc surface of the HDG steel. Without forming ($\varphi$ = 0) no oxidation or reduction peak of zinc is measured due to the blocking character of the $SiO_2$-like film. The zinc oxidation and reduction peak of the cyclic voltammograms increases with increasing forming level. Forming induced cracks in the $SiO_2$ film at slip bands and morphologic changes especially at the grain boundaries increase the free zinc surface which is directly correlated with the current densities of the oxidation and reduction of zinc. The maximum current densities for the uncovered zinc oxide surface ($\max i_{ox}(Zn \mid ZnO)$) and for a 30 nm $SiO_2$-like film surface ($\max i_{ox}(Zn \mid ZnO \mid SiO_2)$) are plotted in Figure 42b.

By comparing the maximum oxidation current densities of the uncovered and the film covered surface, the film surface area $\Theta_{film}$ was calculated as follows:

$$\Theta_{film}(\varphi) = 1 - \frac{\max i_{ox(Zn|ZnO|SiO_2)}(\varphi)}{fit\ \max i_{ox(Zn|ZnO)}(\varphi)} \tag{22}$$

For the calculation the curve of the maximum oxidation current densities of the uncovered zinc surface is idealized by a fit.

A strong reduction of the $SiO_2$ film covered surface of the insulating ultra-thin 30 nm thick $SiO_2$-like film can be measured already at small forming degrees with only 40% film coverage at φ = 0.10 (Figure 42c). The film coverage further decreases with increasing strain. For high strains due to the large area of uncovered zinc after forming, the barrier function of the $SiO_2$-like film seems to be almost reduced to the value of the unprotected surface. Only 20% of the surface is still blocked by the $SiO_2$ film.

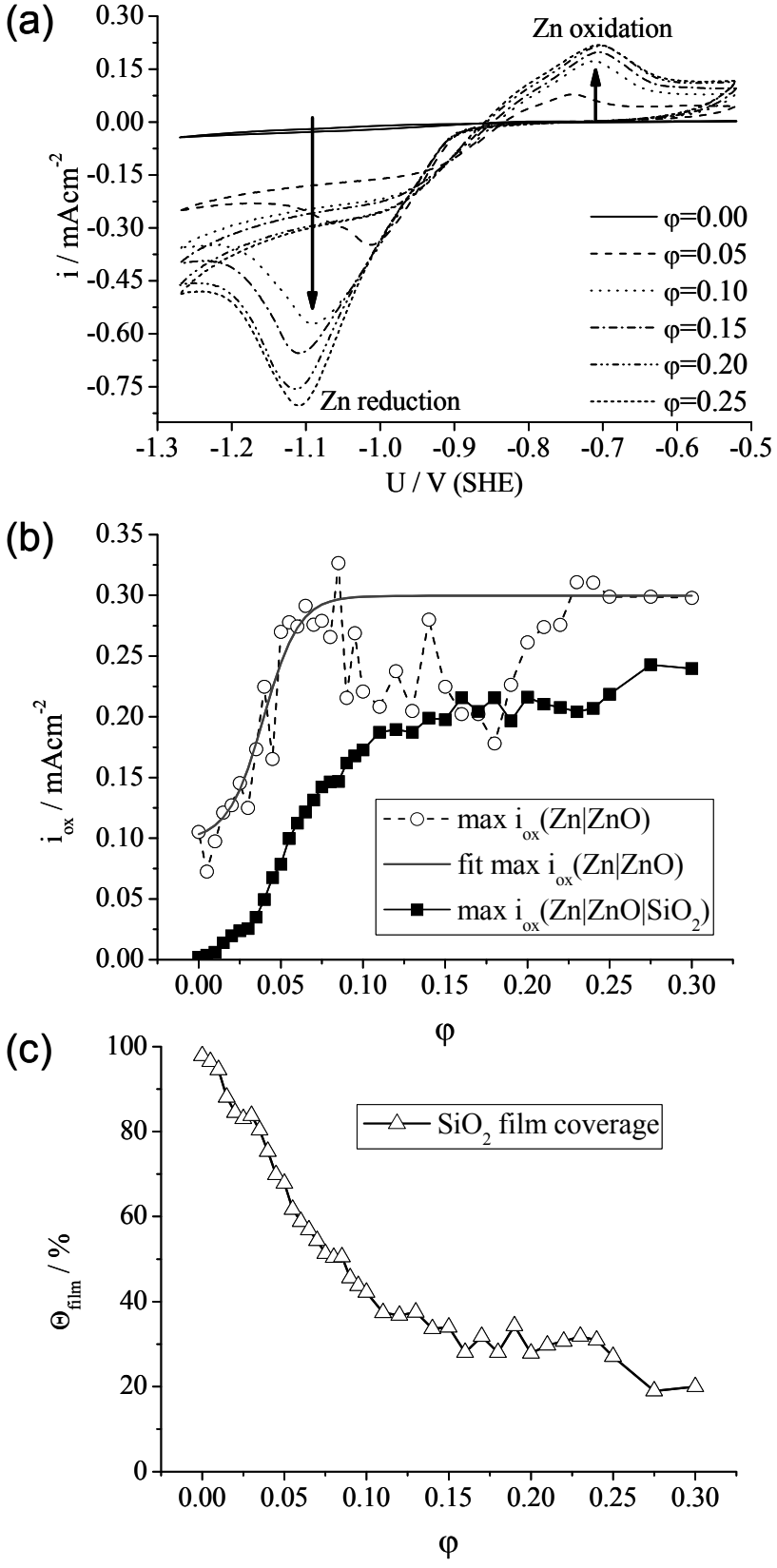


*Figure 42: (a) In-situ CV measurement of alkaline cleaned HDG steel with 30nm $SiO_2$-like film during uniaxial forming. (b) Maximum oxidation current densities for HDG steel without and with 30nm $SiO_2$-like film plotted versus the forming level. (c) Decrease of the $SiO_2$-like film coverage with increasing forming level.*

### 6.2.2 Micro- and nanoscopic Kelvin probe studies of defects and interfacial corrosive de-adhesion

In the past 20 years the interfacial corrosive de-adhesion processes of thin and thick polymer films on iron and zinc substrates was studied by integral and local electrochemical methods [104-106]. Especially the scanning Kelvin probe was established as a method to measure non-destructively the corrosion potential at the buried polymer/metal interface [2, 100, 101, 107].
In Chapter 5 it is shown that the corrosive de-adhesion on organically coated zinc is almost completely inhibited by interfacial 10 nm $SiO_2$-like plasma polymer films. The effective inhibition of the oxygen reduction at the intact oxide/$SiO_2$/polymer interfaces leads to a strong inhibition of the cathodic de-adhesion process. Moreover, the potential difference between the intact area and the corroding defect which could act as a driving force for the de-adhesion process also diminishes. The typical line profiles obtained by the HR-SKP are shown in Figure 43 with no detectable corrosive de-adhesion for the intact $SiO_2$-like film and with the fast propagating delamination front for non-modified polymer/zinc interfaces. The corrosive de-adhesion of the polymer film starts at the defect and propagates in the direction of the intact zinc oxide/$SiO_2$/polymer interface.

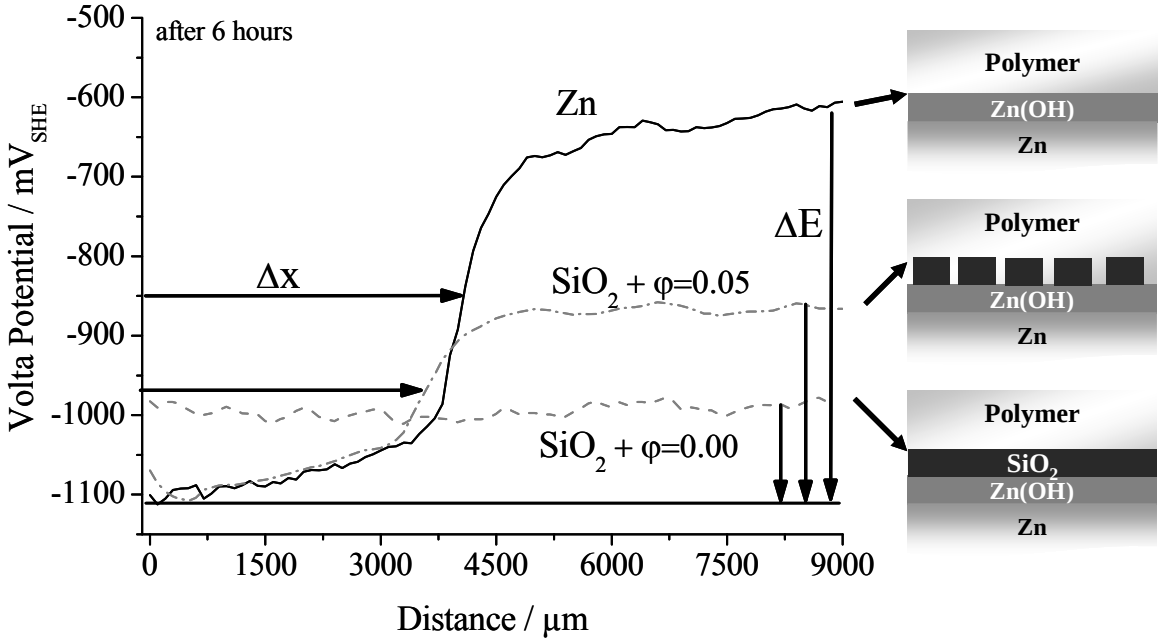


*Figure 43: Typical height regulated scanning Kelvin probe line profiles after 6 hours for bare zinc, defect free $SiO_2$ coated HDG and defect containing $SiO_2$ coatings after forming ($\varphi$ = 0.05). The thickness of the $SiO_2$ like films was 10nm.*

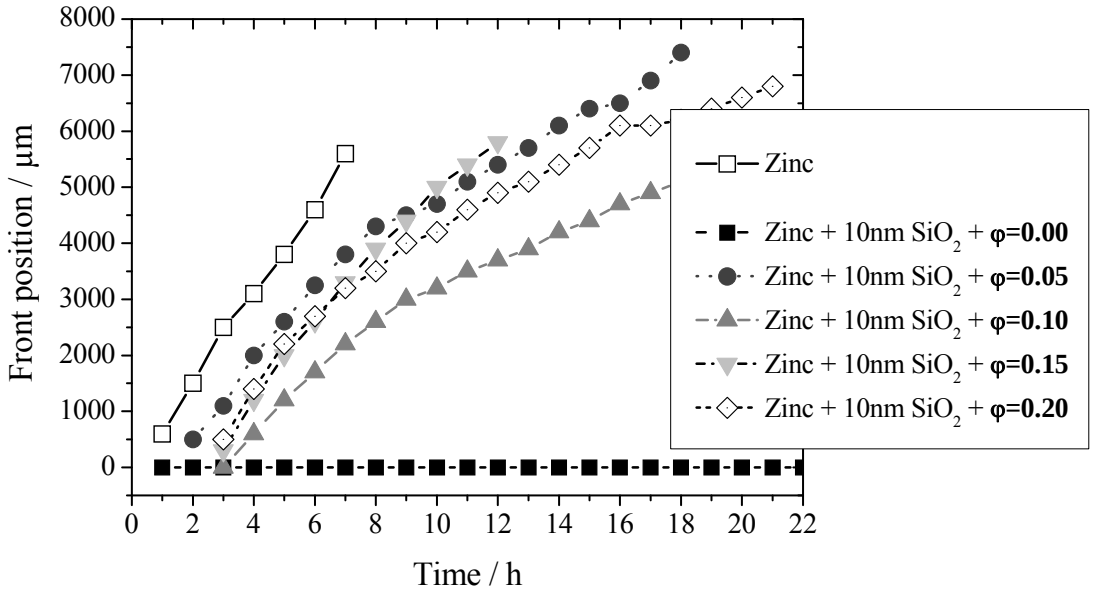


*Figure 44: Comparison of the position of the delamination front for zinc without and with 10 nm $SiO_2$-like film and different uniaxial forming degrees.*

The in-situ cyclic voltammetry measurements showed the strong decrease of the $SiO_2$ film covered zinc surface area during stretch forming of the samples. Therefore, corrosive de-adhesion is also observed on the stretch formed samples with similar kinetics as for the samples with no interfacial plasma polymer film.

To compare the delamination kinetics of the different formed samples in detail, the turning points of the potential-transitions were plotted versus time in Figure 44. For the intact $SiO_2$ film no propagating delamination front could be observed. For the non-modified interface and the stretch formed samples with interfacial plasma polymer film a fast delamination was observed. The corresponding delamination rates were not constant for longer times, as the delamination process is strongly transport limited for large distances between the defect and the delamination front.

To compare the delamination rates only the linear propagation within the first 7 hours was evaluated. In Figure 45a the delamination rates are plotted versus the respective forming degree. In Figure 45b the delamination rates are further plotted versus the potential difference between the defect potential and the potential of the intact area. In both cases the delamination rates show a step like increase with the formation of cracks in the plasma polymer film.

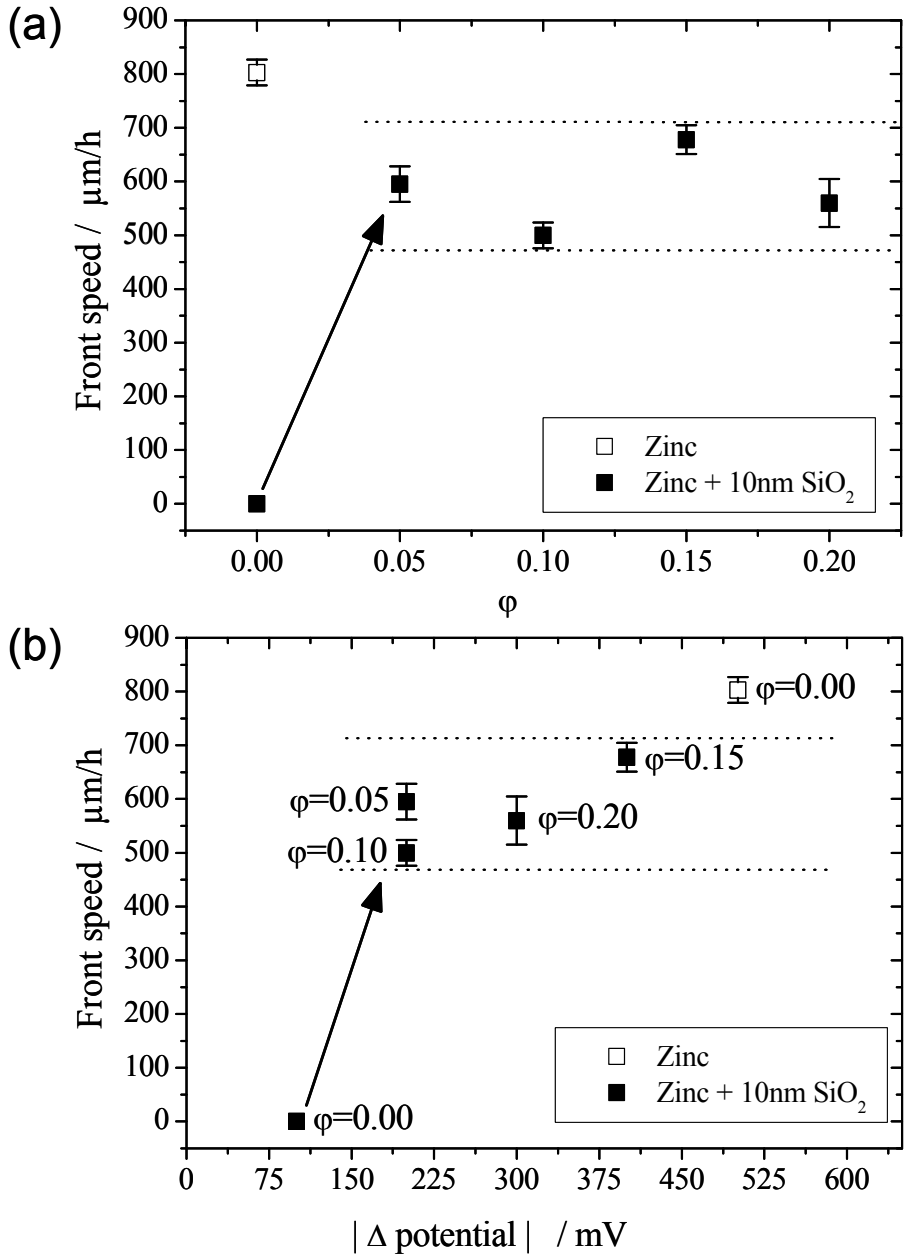


*Figure 45: Comparison of the delamination speed for zinc without and with 10 nm $SiO_2$-like film and different uniaxial forming degrees in relation to (a) the forming degree and (b) the Volta potential difference between the delaminated and the intact area.*

Microscopic FT-IRRAS measurements after the removal of the delaminated organic coating still confirm the existence of the $SiO_2$ spectrum of the 10 nm thick film. Therefore, it could be concluded that the organic coating was de-adhered from the defect containing $SiO_2$ surface film and the oxide covered zinc areas while the $SiO_2$-like film still stays adhered to the substrate.

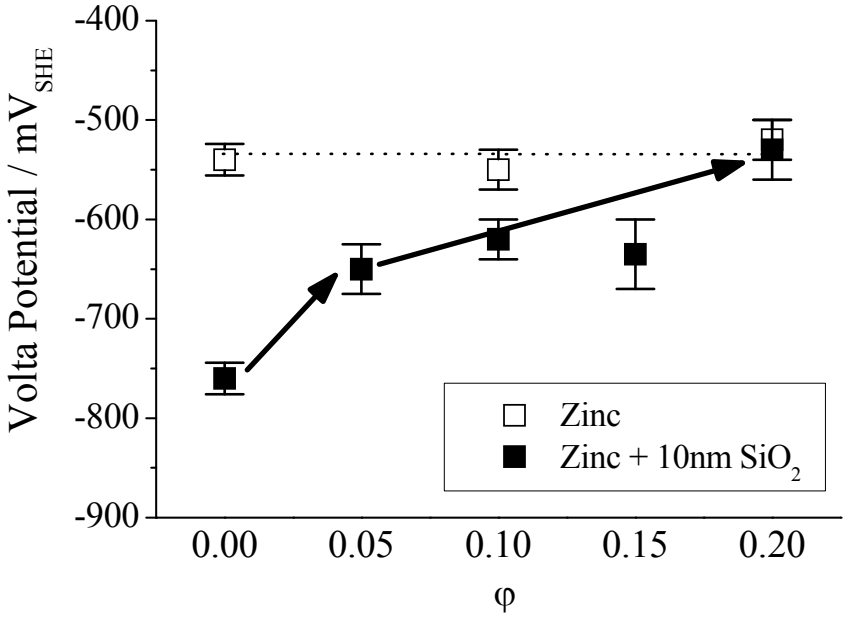


*Figure 46: Mean Volta potential of HDG surface without and with 10 nm $SiO_2$-like film after different uniaxial forming degrees measured in $O_2$ atmosphere with high humidity (95% r.h.).*

The influence of forming on the measured Volta potential is plotted for different forming degrees in Figure 46. The uncovered zinc surface showed a stable anodic Volta potential, as the bare zinc surface is immediately oxidised under atmospheric conditions. For the $SiO_2$ film protected zinc surface the measured Volta potential increased with increasing forming degree. The strong increase of the potential for small forming values correlates very well with the strong decrease of the $SiO_2$ film coverage based on the in-situ cyclic voltammetry measurements.

It should be noted that for standard Kelvin probe measurements the used SKP tip diameter is 500 times larger than typical crack widths in the $SiO_2$ film and therefore the SKP studies always present a laterally averaged interface potential.

SKP-FM measurements were performed to overcome this averaging effect and to correlate the microscopically measured potential of the HR-SKP with the nanoscopic defects. On an intact and insulating 10 nm $SiO_2$ film a constant potential level could be detected without an indication of topography artefacts (see Figure 47).

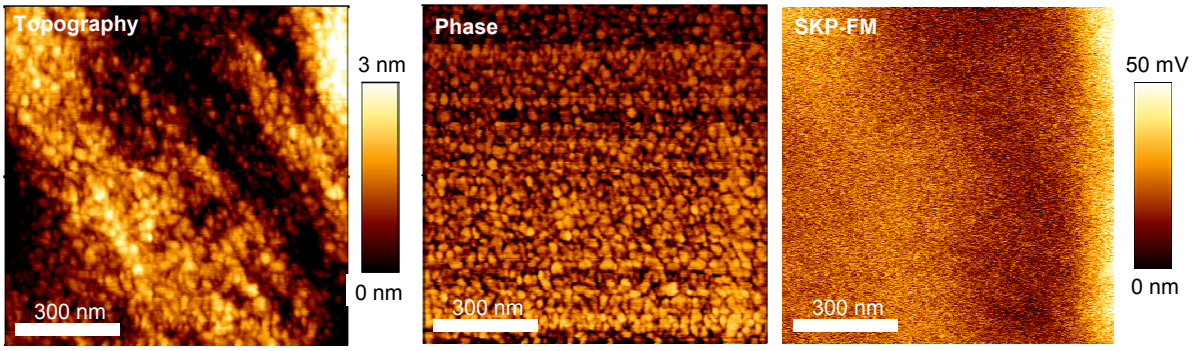


*Figure 47: AFM topography, phase and SKP-FM measurement of an alkaline cleaned HDG surface with 10 nm $SiO_2$-like film.*

Figure 48 shows for instance a formed sample with cracks in a 50 nm $SiO_2$ film which are orientated vertical in the picture. Due to the high surface roughening small cracks in the $SiO_2$-like film are difficult to measure topographically However, distinct potential differences between the intact and adhering $SiO_2$ film and the uncovered zinc surface areas could be

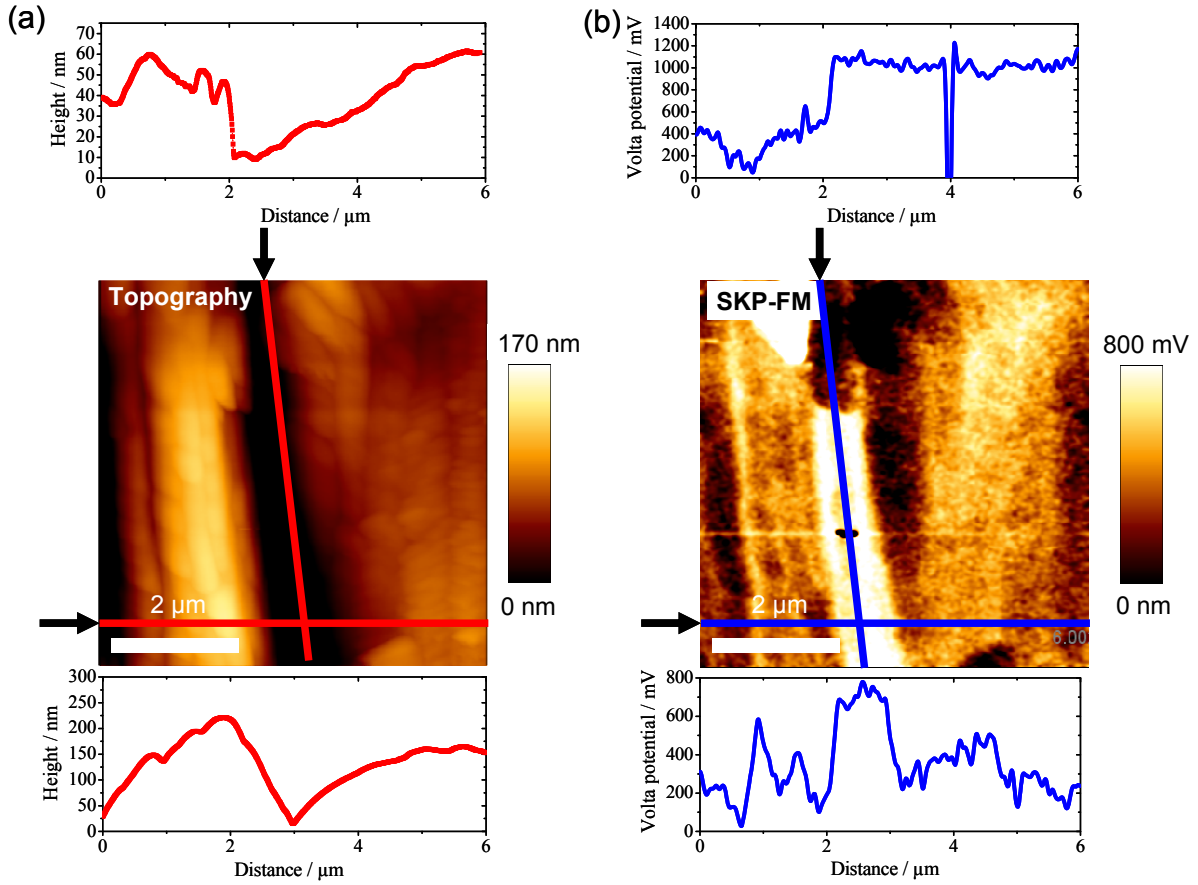


*Figure 48: (a) AFM topography and (b) SKP-FM measurement of an alkaline cleaned HDG surface with 50 nm $SiO_2$-like film after 0.2 uniaxial forming. In the centre of the pictures a part of the 50 nm $SiO_2$ film is peeled off after forming.*

detected easily in the centre of the scan area where a part of the 50 nm thick $SiO_2$ film was de-adhered. A 40-50 nm step in the $SiO_2$ coating could be observed in the topography line scan as well as the corresponding jump of the potential of 600mV between the bare zinc and the insulating $SiO_2$-like film. This value is three times larger as it would be expected from previous Kelvin probe measurements. But it should be noted that the absolute potential contrast of the $SiO_2$ and free zinc surface does not necessarily represent the true potential value in SKP-FM measurements but indicates well in this case the existence of intact and non-intact areas [48].

## 6.3 Conclusions and model

The microscopic and electrochemical studies illustrates that the formation of line shaped defects with a distance of some hundred nanometre and a width of several tens of nanometres after stretch forming leads to an almost complete loss of the barrier properties of the interfacial 10 nm thick $SiO_2$-like films with regard to the cathodic de-adhesion process. In-situ cyclic voltammetry during forming is a valuable method to monitor the increase in uncovered zinc during such a forming process. Due to the formation of the cracks in the $SiO_2$ coating, the interfacial oxygen reduction densities are significantly increased to values which are comparable to those of organically coated zinc surfaces without an interfacial plasma polymer film. Since still a large part of the surface is covered with the adhering $SiO_2$-like film this can be explained by the formation of a microelectrode array.

SKP-FM and HR-SKP studies show that the cathodic interfacial potential shift caused by the $SiO_2$ film is increased by the formation of cracks and that the integral potential is a superposition of the interfacial potentials in those areas where the $SiO_2$-like film is still adhering and those areas where the surface is uncovered or where the $SiO_2$ film is de-adhered. In such cases the oxygen adsorption and reduction on the zinc oxide surface is not fully inhibited any more.

The SKP studies of the cathodic de-adhesion process of the organic primer on the formed thin film coated substrate show, that as for the electrochemical studies of immersed samples the interfacial oxygen reduction and thereby the cathodic disbondment process under the organic coating is comparable to the non thin film coated substrate as soon as cracks are formed in the ultra-thin film.

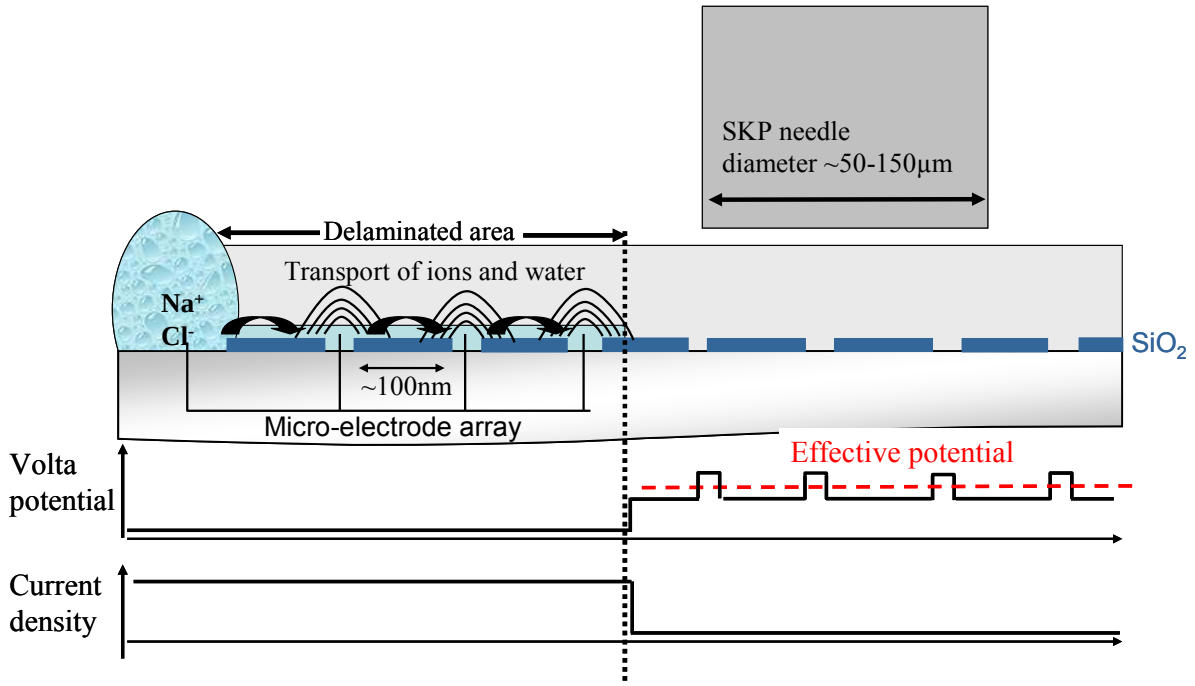


*Figure 49: Mechanistic picture of the correlation between forming of insulating film, corrosion protection and SKP Volta potential values.*

Figure 49 shows the proposed mechanistic picture of the cathodic de-adhesion process on the crack containing interfacial thin interfacial films. The oxygen reduction density in the de-adhered area of the organic coating with an ultra-thin interfacial electrolyte layer is not limited by the $SiO_2$ film covered areas due to the micro-electrode array. In the intact area the adhering $SiO_2$ film is leading to a cathodic shift of the effective interfacial potential depending on the ratio between thin $SiO_2$ film covered and uncovered zinc surface. The applied organic coating is not able to reduce the interfacial oxygen reduction density and the correlated potential as effectively as the $SiO_2$ film due to its higher free volume at the interface to the oxide covered zinc.

At the front of electrochemical de-adhesion, the oxygen reduction process is occurring in the cracks and the small distance between the defects of few hundred nanometres enables a fast transport of hydrated ions from the front of the de-adhered area to the next crack. Even for small interfacial transport rates with an effective mobility of some micrometers per hour it would take only minutes for hydrated ions to migrate from one defect to the next one [101]. After reaching the next defect the oxygen reduction density in this local area is increasing to the value comparable to the one for the system without the interfacial $SiO_2$-like film. This explains why the increase of the corrosive de-adhesion velocity is valid already for quite small strains of about 0.05.

# 7 General conclusions

The scope of this thesis was to modify the passive film on zinc with ultra-thin barrier plasma polymer films and to correlate the structure and physical properties of the surface layer with the inhibition of the interfacial oxygen reduction kinetics in humid and corrosive environments. Especially the influence of forming of the ultra-thin barrier plasma polymer coated substrates and the decrease of the corrosion protection was investigated in detail by using a combination of a tensile testing device and an electrochemical capillary cell. This set-up allowed monitoring in-situ the formation of free metallic surface during stretch forming of the plasma polymer coated HDG substrate and therefore enables the correlation of the forming degree with the loss of the corrosion resistance during tensile forming. Hot-dip galvanised steel was used as a technical material of high industrial relevance.

The corrosion resistance of PE-CVD deposited $SiO_2$-like films is based on the barrier properties of the inorganic coating by inhibition of the oxygen reduction at the metal/polymer interface in corrosive environments. Kelvin probe measurements reveal, that the Volta potential difference between an intact film and an active defect on zinc reflects the driving force for the cathodic corrosive de-adhesion of the polymer top-coat and therefore the rate for corrosive de-adhesion at the interphase of the polymer coated $SiO_2$ film covered zinc surfaces. Even the insulating properties of the 10nm thick $SiO_2$-like film effectively inhibit the oxygen reduction and therefore decrease the resulting current density which results in a very small overpotential.

Electrochemical impedance and cyclic voltammetry measurements showed that the oxygen reduction kinetics were strongly inhibited even for the 10nm thick $SiO_2$-like films. From the

viewpoint of thin film engineering, it is the aim to achieve functional properties at extremely low thickness values. It can be assumed from the measurements that the principal behaviour of the interfacial $SiO_2$-like film as corrosion protection is representative for different highly crosslinked insulating films, e.g. such as Zr-oxide films.

Chapter 6 focussed on the influence of the forming processes on the structure and functionality of the interfacial ultra-thin $SiO_2$-like plasma polymer films on zinc galvanised substrates. The low flexibility of such thin films leads to characteristic defects during forming of coated substrates which lead to a partial loss of the achieved functional properties. Stretch forming of galvanised steel coated with $SiO_2$-like plasma polymer films with a thickness of 10 to 50 nm was performed to study the formation of defects in the films and their relevance for the corrosion protection properties of the coated substrate. For ultra-thin films surface induced defects like atomic slip lines and slip bands on the zinc surface lead to crack formation in the $SiO_2$-like films, whereas the film adheres very well to the surface. If the film thickness is larger than 50nm the induced stress by the surface defects of the zinc surface leads to a partial flaking off of the $SiO_2$ coating.

Microscopic, electrochemical and spectroscopic methods were combined to correlate the size and distribution of these nanoscopic defects with the corrosive de-adhesion mechanisms and kinetics for organically coated substrates. Cyclic voltammetric and scanning Kelvin probe measurements showed that oxygen reduction occurs due to the 3-dimensional increased zinc surface in the nanoscopic defects in between completely insulating areas of $SiO_2$ film acting as microelectrode arrays for the cathodic de-adhesion process.

In-situ cyclic voltammetry during forming is a valuable method to monitor the increase of the uncovered zinc area during such a forming process. SKP-FM and HR-SKP studies showed that the cathodic interfacial potential shift caused by the $SiO_2$ film is increased by the formation of cracks and that the integral potential is a superposition of the interfacial potentials in those areas where the $SiO_2$-like film is still adhering and those areas where the surface is uncovered or where the $SiO_2$ film is de-adhered. In such cases the oxygen adsorption and reduction on the zinc oxide surface is not fully inhibited any more.

# 8 Outlook

In future studies the existence of forming induced defects is the most limiting factor in the development of formable functional barrier coatings.

Besides the restricted possibility to increase the elastic properties of ceramic or ductile plasma polymer films further investigations should focus on the possibility to influence the electrochemical activity of the forming induced nanosized defects within the insulating plasma polymer films.

Electrochemical measurements used in-situ during forming allows the improved investigation of functional coatings and the use of this combination should therefore be expanded.

As corrosion protected galvanised steel consists of different layers, plasma polymer films should be combined with other established and new experimental concepts to form systems with superior corrosion protection properties.

The galvanised steel could be protected by an enhanced zinc/magnesium coating as base substrate which is proposed in various publications [108]. But up to now, no knowledge of the Volta potential after forming of such enhanced coatings and therefore about a possible change of the driving force of the cathodic delamination is available.

The combination of such enhanced coatings with ultra-thin insulating plasma polymer films could probably form a very effective corrosion protection.

After forming and creation of defects in these kinds of substrates the cathodic delamination processes are mainly limited by the strength of the bonding of the organic top coat and the oxygen reduction in the formed defects at the metal surface. Therefore, adhesion promoting molecules like gamma-aminopropyltriethoxysilane between the organic lacquer and the plasma polymer films should increase the strength of the multi layer system and therefore stabilise the system.

The electrochemical activity of nanosized defects after forming could be influenced by highly mobile lacquer additives which are able to migrate to the substrate/plasma polymer/lacquer interfaces and inhibit or reduce the oxygen reduction of water molecules by inhibition of the electron transfer from the free metallic surface to intermolecular water.

The combination of versatile in-situ tensile testing devices with electrochemical methods like cyclic voltammetry or even Kelvin probe measurements offer a very effective way to further test these complex systems.

# 9 Literature

[1] N. Fink, B. Wilson and G. Grundmeier, Formation of ultra-thin amorphous conversion films on zinc alloy coatings Part 1. Composition and reactivity of native oxides on ZnAl (0.05%) coatings, Electrochimica Acta 51 (2006) 2956-2963.

[2] G. Klimow, N. Fink and G. Grundmeier, Electrochemical studies of the inhibition of the cathodic delamination of organically coated galvanised steel by thin conversion films, Electrochimica Acta 53 (2007) 1290-1299.

[3] C. Stromberg, P. Thissen, I. Klueppel, N. Fink and G. Grundmeier, Synthesis and characterisation of surface gradient thin conversion films on zinc coated steel, Electrochimica Acta 52 (2006) 804-815.

[4] B. Wilson, N. Fink and G. Grundmeier, Formation of ultra-thin amorphous conversion films on zinc alloy coatings - Part 2: Nucleation, growth and properties of inorganic-organic ultra-thin hybrid films, Electrochimica Acta 51 (2006) 3066-3075.

[5] H. Nagel, A.G. Aberle and R. Hezel, Optimised antireflection coatings for planar silicon solar cells using remote PECVD silicon nitride and porous silicon dioxide, Progress in Photovoltaics 7 (1999) 245-260.

[6] B.S. Richards, Comparison of $TiO_2$ and other dielectric coatings for buried-contact solar cells: a review, Progress in Photovoltaics 12 (2004) 253-281.

[7] H. Yasuda, Glow-Discharge Polymerization, Macromolecular Reviews Part D-Journal of Polymer Science 16 (1981) 199-293.

[8] H. Yasuda, *Plasma Polymerization*. 1985, Orlando: Academic Press Inc.

[9] H.K. Yasuda, T.H.F. Wang, D.L. Cho and T.J. Lin, Corrosion protection of cold-rolled steel by low temperature plasma interface engineering .2. Effects of oxides on corrosion performance of E-coated steels, Progress in Organic Coatings 30 (1997) 31-38.

[10] G. Grundmeier and M. Stratmann, Plasma polymerization - a new and promising way for the corrosion protection of steel, Materials and Corrosion-Werkstoffe Und Korrosion 49 (1998) 150-160.

[11] G. Grundmeier, P. Thiemann, J. Carpentier and V. Barranco, Tailored thin plasma polymers for the corrosion protection of metals, Surface & Coatings Technology 174 (2003) 996-1001.

[12] T.J. Lin, J.A. Antonelli, D.J. Yang, H.K. Yasuda and F.T. Wang, Plasma treatment of automotive steel for corrosion protection - a dry energetic process for coatings, Progress in Organic Coatings 31 (1997) 351-361.

[13] W.J. Vanooij, D. Surman and H.K. Yasuda, Plasma-Polymerized Coatings of Trimethylsilane Deposited on Cold-Rolled Steel Substrates .2. Effect of Deposition Conditions on Corrosion Performance, Progress in Organic Coatings 25 (1995) 319-337.

[14] G. Grundmeier and M. Stratmann, Influence of oxygen and argon plasma treatments on the chemical structure and redox state of oxide covered iron, Applied Surface Science 141 (1999) 43-56.

[15] V. Barranco, P. Thiemann, H.K. Yasuda, M. Stratmann and G. Grundmeier, Spectroscopic and electrochemical characterisation of thin cathodic plasma polymer films on iron, Applied Surface Science 229 (2004) 87-96.

[16] P.H. Wojciechowski and M.S. Mendolia, On the Multiple Fracture of Low-Elongation Thin-Films Deposited on High-Elongation Substrates, Journal of Vacuum Science & Technology A: Vacuum, Surfaces, and Films 7 (1989) 1282-1288.

[17] P.H. Wojciechowski and M.S. Mendolia, *Physics of Thin Films. Thin Films for Emerging Applications*, ed. M.H. Francombe and J.L. Vossen. 1992, New York: Academic Press.

[18] Y. Leterrier, Durability of nanosized oxygen-barrier coatings on polymers, Progress in Materials Science 48 (2003) 1-55.

[19] A.P. McGuigan, G.A.D. Briggs, V. Burlakov, M. Yanaka and Y. Tsukahara, An elastic-plastic shear lag model for fracture of layered coatings, Thin Solid Films 424 (2003) 219-223.

[20] A.C. Bastos and A.M.P. Simoes, Effect of uniaxial strain on the protective properties of coil-coatings, Progress in Organic Coatings 46 (2003) 220-227.

[21] S. Lazik, C. Esling and J. Wegria, Cracking in Zinc Layers on Continous Galvanized Sheets, Textures and Microstructures 23 (1995) 131-147.

[22] R. Parisot, S. Forest, A. Pineau, F. Grillon, X. Demonet and J.M. Mataigne, Deformation and damage mechanisms of zinc coatings on hot-dip galvanized steel sheets: Part 1. Deformation modes, Metallurgical and Materials Transactions A 35A (2004) 797-811.

[23] R. Parisot, S. Forest, A. Pineau, F. Nguyen, X. Demonet and J.M. Mataigne, Deformation and damage mechanisms of zinc coatings on hot-dip galvanized steel sheets: Part II. Damage modes, Metallurgical and Materials Transactions A 35A (2004) 813-823.

[24] B. Baumert, M. Stratmann and M. Rohwerder, Formability of ultra-thin plasma-polymer films deposited on metal sheet: mesoscopic and nanoscopic aspects of defect formation, Zeitschrift für Metallkunde 795 (2004) 257-262.

[25] H.L. Cox, The Elasticity and Strength of Paper and Other Fibrous Materials, British Journal of Applied Physics 3 (1952) 72-79.

[26] R.L. Bell and R.W. Cahn, The Dynamics of Twinning and the Interrelation of Slip and Twinning in Zinc Crystals, Proceedings of the Royal Society of London. Series A, Mathematical and Physical Sciences 239 (1957) 494-521.

[27] P.G. Partridge, The crystallography and deformation modes of hexagonal close-packed metals, Metallurgical and Materials Transactions A 12 (1957) 169-194.

[28] E.J. Stofel and D.S. Wood, *Fracture of Solids*. Vol. 20. 1963, New York: Interscience. 521-39.

[29] G. Grundmeier, M. Brettmann and P. Thiemann, In situ spectroscopic and corrosion studies of ultra-thin gradient plasma polymer layers on zinc, Applied Surface Science 217 (2003) 223-232.

[30] A.R. Marder, The metallurgy of zinc-coated steel, Progress in Materials Science 45 (2000) 191-271.

[31] X.G. Zhang, Galvanic corrosion of zinc and its alloys, Journal of the Electrochemical Society 143 (1996) 1472-1484.

[32] T.H. Muster, A.K. Neufeld and I.S. Cole, The protective nature of passivation films on zinc: wetting and surface energy, Corrosion Science 46 (2004) 2337-2354.

[33] H. Yasuda, B.H. Chun, D.L. Cho, T.J. Lin, D.J. Yang and J.A. Antonelli, Morphology of phosphate layer investigated by vacuum depositing a parylene C film, Corrosion 52 (1996) 584-591.

[34] H. Yasuda, B.H. Chun, D.L. Cho, T.J. Lin, D.J. Yang and J.A. Antonelli, Interface-engineered parylene C coating for corrosion protection of cold-rolled steel, Corrosion 52 (1996) 169-176.

[35] N.J. Shirtcliffe, M. Stratmann and G. Grundmeier, In situ infrared spectroscopic studies of ultrathin inorganic film growth on zinc in non-polymerizing cold plasmas, Surface & Interface Analysis 35 (2003) 799-804.

[36] G. Grundmeier and M. Stratmann, Adhesion and De-adhesion mechanisms at polymer/metal interfaces: Mechanistic understanding based on in situ studies of buried interfaces, Annual Review of Materials Research 35 (2005) 571-615.

[37] H.S. Wroblowa and S.B. Qaderi, The Mechanism of Oxygen Reduction on Zinc, Journal of Electroanalytical Chemistry and Interfacial Electrochemistry 295 (1990) 153-161.

[38] H.S. Wroblowa and S.B. Qaderi, Mechanism and Kinetics of Oxygen Reduction on Steel, Journal of Electroanalytical Chemistry and Interfacial Electrochemistry 279 (1990) 231-242.

[39] H.S. Wroblowa, Intermediate Products of Atmospheric Oxygen Reduction and the Integrity of Metal Organic Coating Interface, Journal of Eectroanalytical Chemistry and Interfacial Electrochemistry 339 (1992) 31-40.

[40] A. Leng, H. Streckel and M. Stratmann, The delamination of polymeric coatings from steel. Part 1. Calibration of the Kelvin probe and basic delamination mechanism, Corrosion Science 41 (1999) 547-578.

[41] W. Fürbeth and M. Stratmann, The delamination of polymeric coatings from electrogalvanised steel - a mechanistic approach. Part 1: delamination from a defect with intact zinc layer, Corrosion Science 43 (2001) 207-227.

[42] R. d'Agostino, *Plasma Deposition, Treatment, and Etching of Polymers*. 1990, Boston: Academic Press.

[43] S. Eufinger, W.J. van Ooij and K.D. Conners, DC-plasma polymerization of hexamethyldisiloxane .2. Surface and interface characterization of films deposited on stainless-steel substrates, Surface and Interface Analysis 24 (1996) 841-855.

[44] W.J. vanOoij, S. Eufinger and S.Y. Guo, DC plasma polymerization of hexamethyldisiloxane, Plasma Chemistry and Plasma Processing 17 (1997) 123-154.

[45] W. Michaeli, S. Gobel and R. Dahlmann, The influence of strain on the properties of plasma polymerized permeation barriers, Journal of Polymer Engineering 24 (2004) 107-122.

[46] M. Stratmann and H. Streckel, On the Atmospheric Corrosion of Metals Which Are Covered with Thin Electrolyte Layers .1. Verification of the Experimental-Technique, Corrosion Science 30 (1990) 681-696.

[47] M. Stratmann, K.T. Kim and H. Streckel, New Experimental-Techniques for Investigating the Atmospheric Corrosion of Metals Covered by Thin Electrolyte Layers, Zeitschrift für Metallkunde 81 (1990) 715-725.

[48] M. Rohwerder and F. Turcu, High-resolution Kelvin probe microscopy in corrosion science: Scanning Kelvin probe force microscopy (SKPFM) versus classical scanning Kelvin probe (SKP), Electrochimica Acta 53 (2007) 290-299.

[49] G. Grundmeier, E. Matheisen and M. Stratmann, Formation and stability of ultrathin organosilane polymers on iron, Journal of Adhesion Science and Technology 10 (1996) 573-588.

[50] T.F. Wang and H.K. Yasuda, Modification of Wettability of a Stainless-Steel Plate by Cathodic Plasma Polymerization of Trimethylsilane Oxygen Mixtures, Journal of Applied Polymer Science 55 (1995) 903-909.

[51] N. Shirtcliffe, P. Thiemann, M. Stratmann and G. Grundmeier, Chemical structure and morphology of thin, organo-silicon plasma-polymer films as a function of process parameters, Surface and Coatings Technology 142-144 (2001) 1121-1128.

[52] G. Grundmeier, P. Thiemann, J. Carpentier, N. Shirtcliffe and M. Stratmann, Tailoring of the morphology and chemical composition of thin organosilane microwave plasma polymer layers on metal substrates, Thin Solid Films 446 (2004) 61-71.

[53] G.R. Prasad, S. Daniels, D.C. Cameron, B.P. McNamara, E. Tully and R. O'Kennedy, PECVD of biocompatible coatings on 316L stainless steel, Surface and Coatings Technology 200 (2005) 1031-1035.

[54] H. Chatham, Oxygen diffusion barrier properties of transparent oxide coatings on polymeric substrates, Surface and Coatings Technology 78 (1996) 1-9.

[55] U. Moosheimer and C. Bichler, Plasma pretreatment of polymer films as a key issue for high barrier food packagings, Surface and Coatings Technology 116-119 (1999) 812-819.

[56] M. Deilmann, M. Grabowski, S. Theiss, N. Bibinov and P. Awakowicz, Permeation mechanisms of pulsed microwave plasma deposited silicon oxide films for food packaging applications, Journal of Physics D: Applied Physics 41 (2008) 135207 (7pp).

[57] V.S. Nguyen, J. Underhill, S. Fridmann and P. Pan, Plasma Organo-Silicon Polymers - Deposition, Characterization, and Application in Multilayer Resist, Journal of the Electrochemical Society 132 (1985) 1925-1932.

[58] F. Fracassi, R. Dagostino and P. Favia, Plasma-Enhanced Chemical Vapor-Deposition of Organosilicon Thin-Films from Tetraethoxysilane-Oxygen Feeds, Journal of the Electrochemical Society 139 (1992) 2636-2644.

[59] D. Hegemann, U. Vohrer, C. Oehr and R. Riedel, Deposition of SiOx films from O-2/HMDSO plasmas, Surface & Coatings Technology 119 (1999) 1033-1036.

[60] S. Sahli, Y. Segui, S. Ramdani and Z. Takkouk, Rf Plasma Deposition from Hexamethyldisiloxane Oxygen Mixtures, Thin Solid Films 250 (1994) 206-212.

[61] G. Grundmeier and A. Stratmann, Nucleation and Growth of Plasma-Polymerised Hexamethyldisilazane on Iron -Substrates, Berichte der Bunsen-Gesellschaft für Physikalische Chemie 99 (1995) 1387-1392.

[62] C. Rau and W. Kulisch, Mechanisms of Plasma Polymerization of Various Silico-Organic Monomers, Thin Solid Films 249 (1994) 28-37.

[63] C.T. Lin, F. Li and T.D. Mantei, Low-temperature plasma deposition of dielectric coatings from organosilicon precursors, Journal of Vacuum Science & Technology A: Vacuum, Surfaces, and Films 17 (1999) 735-740.

[64] A.J. Beaudoin and A. Acharya, A model for rate-dependent flow of metal polycrystals based on the slip plane lattice incompatibility, Materials Science & Engineering. A, Structural Materials : Properties, Microstructure and Processing 309 (2001) 411-415.

[65] A.J. Beaudoin, A. Acharya, S.R. Chen, D.A. Korzekwa and M.G. Stout, Consideration of grain-size effect and kinetics in the plastic deformation of metal polycrystals, Acta Materialia 48 (2000) 3409-3423.

[66] Z. Marciniak, J.L. Duncan and S.J. Hu, *Mechanics of Sheet Metal Forming*. Second edition ed. 2002, Oxford: Butterworth-Heinemann.

[67] K. Lange, *Umformtechnik*. Second edition ed. 2002, Berlin Heidelberg New York: Springer.

[68] E. Döge and B.-A. Behrens, *Handbuch Umformtechnik: Grundlagen, Technologien, Maschinen*. 2007, Berlin Heidelberg New York: Springer.

[69] R. Parisot, S. Forest, A.F. Gourgues, A. Pineau and D. Mareuse, Modeling the mechanical behavior of a multicrystalline zinc coating on a hot-dip galvanized steel sheet, Computational Materials Science 19 (2000) 189-204.

[70] D. Raabe, M. Sachtleber, H. Weiland, G. Scheele and Z.S. Zhao, Grain-scale micromechanics of polycrystal surfaces during plastic straining, Acta Materialia 51 (2003) 1539-1560.

[71] R. Becker, Effects of strain localization on surface roughening during sheet forming, Acta Materialia 46 (1998) 1385-1401.

[72] P.B. Kirk and R.M. Pilliar, The deformation response of sol-gel-derived zirconia thin films on 316L stainless steel substrates using a substrate straining test, Journal of Materials Science 34 (1999) 3967-3975.

[73] K. Wapner and G. Grundmeier, Scanning Kelvin probe measurements of the stability of adhesive/metal interfaces in corrosive environments, Advanced Engineering Materials 6 (2004) 163-167.

[74] K. Wapner, B. Schoenberger, A. Stratmann and G. Grundmeier, Height-regulating scanning Kelvin probe for simultaneous measurement of surface topology and electrode potentials at buried polymer/metal interfaces, Journal of the Electrochemical Society 152 (2005) E114-E122.

[75] J. Raacke, M. Giza and G. Grundmeier, Combination of FTIR reflection absorption spectroscopy and work function measurement for in-situ studies of plasma modification of polymer and metal surfaces, Surface & Coatings Technology 200 (2005) 280-283.

[76] F. Mansfeld, Use of electrochemical impedance spectroscopy for the study of corrosion protection by polymer coatings - Reply, Journal of Applied Electrochemistry 25 (1995) 1145-1145.

[77] C.H. Hammann and W. Vielstich, *Elektrochemie*. 2003, Weinheim, Germany: Wiley-VCH.

[78] E. Klusmann, U. Konig and J.W. Schultze, Electrochemical Characterization of Phosphate Layers on Zinc Coated Steel, Werkstoffe Und Korrosion - Materials and Corrosion 46 (1995) 83-91.

[79] A. Losch, J.W. Schultze and H.D. Speckmann, A New Electrochemical Method for the Determination of the Free-Surface of Phosphate Layers, Applied Surface Science 52 (1991) 29-38.

[80] I. Klüppel, B. Schinkinger and G. Grundmeier, In-Situ Electrochemical Studies of Forming Induced Defects of Organic Coatings on galvanised steel, Electrochimica Acta 54 (2009) 3553-3560.

[81] V.P. Tolstoy, V.I. Chernyshova and S.V. A., *Handbook of infrared spectroscopy of ultrathin films*. 2003: John Wiley & Sons.

[82] J.F. Moulder, W.F. Stickle, P.E. Sobol and K.D. Bomben, *Handbook of X-ray Photoelectron Spectroscopy*. 1992, Eden Prairie, USA: Perkin-Elmer Corporation, Physical Electronics Division.

[83] H. Fujiwara, *Spectroscopic ellipsometry: principles and applications*. 2007, Chichester, England: John Wiley and Sons.

[84] S.L. Flegler, J.W. Heckman and K.L. Klomparens, *Scanning and Transmission Electron Microscopy: An Introduction*. 1993, Cary, U.S.A: Oxford University Press.

[85] A.J. Schwartz, M. Kumar and A.B. L., *Electron backscatter diffraction in materials science*. 2000: Springer.

[86] N. Shirtcliffe, P. Thiemann, M. Stratmann and G. Grundmeier, Chemical structure and morphology of thin, organo-silicon plasma-polymer films as a function of process parameters, Surface & Coatings Technology 142 (2001) 1121-1128.

[87] A.K. Neufeld and I.S. Cole, Using Fourier transform infrared analysis to detect corrosion products on the surface of metals exposed to atmospheric conditions, Corrosion Science 53 (1997) 788-799.

[88] D. Lin-Vien, N.B. Colthup, W.G. Fateley and J.G. Grasselli, *The Handbook of Infrared and Raman Spectroscopy Chracteristic Frequencies of Organic Molecules*. 1991, San Diego: Academic Press Inc.

[89] D. Eisenberg and W. Kauzmann, *The Structure and Properties of Water*. 1969, London: Oxford University Press.

[90] N. Cabrera and N.F. Mott, Theory of the Oxidation of Metals, Reports on Progress in Physics 12 (1948) 163-184.

[91] K. Fukui, H. Miyauchi and Y. Iwasawa, Highly sensitive detection of adsorbed species on a $SiO_2$ surface by reflection-absorption infrared spectroscopy, Chemical Physics Letters 274 (1997) 133-139.

[92] C. Stromberg, P. Thissen, I. Klüppel, N. Fink and G. Grundmeier, Synthesis and characterisation of surface gradient thin conversion films on zinc coated steel, Electrochimica Acta 52 (2006) 804-815.

[93] J.W. Schultze and M.M. Lohrengel, Stability, reactivity and breakdown of passive films. Problems of recent and future research, Electrochimica Acta 45 (2000) 2499-2513.

[94] A.J. Bard, M. Stratmann and G.S. Frankel, *Encyclopedia of Electrochemistry, Volume 4, Corrosion and Oxide Films*. Encyclopedia of Electrochemistry. Vol. 4. 2003, Weinheim: Wiley-VCH. 755.

[95] A. Leng, H. Streckel and M. Stratmann, The delamination of polymeric coatings from steel. Part 1. Calibration of the Kelvinprobe and basic delamination mechanism, Corrosion Science 41 (1999) 547-578.

[96] M. Stratmann, K.T. Kim and H. Streckel, New Experimental-Techniques for Investigating the Atmospheric Corrosion of Metals Covered by Thin Electrolyte Layers, Zeitschrift Fur Metallkunde 81 (1990) 715-725.

[97] M. Stratmann, A. Leng, W. Furbeth, H. Streckel, H. Gehmecker and K.H. GrosseBrinkhaus, The scanning Kelvin probe; A new technique for the in situ analysis of the delamination of organic coatings, Progress in Organic Coatings 27 (1996) 261-267.

[98] M. Stratmann and H. Streckel, The Investigation of the Corrosion of Metal-Surfaces, Covered with Thin Electrolyte Layers - a New Experimental-Technique, Berichte Der Bunsen-Gesellschaft-Physical Chemistry Chemical Physics 92 (1988) 1244-1250.

[99] M. Stratmann, H. Streckel and R. Feser, A New Technique Able to Measure Directly the Delamination of Organic Polymer-Films, Corrosion Science 32 (1991) 467-470.

[100] R. Posner, K. Wapner, M. Stratmann and G. Grundmeier, Transport processes of hydrated ions at polymer/oxide/metal interfaces: Part 1. Transport at interfaces of polymer coated oxide covered iron and zinc substrates, Electrochimica Acta 54 (2009) 891-899.

[101] R. Posner, T. Titz, K. Wapner, M. Stratmann and G. Grundmeier, Transport processes of hydrated ions at polymer/oxide/metal interfaces: Part 2. Transport on oxide covered iron and zinc surfaces, Electrochimica Acta 54 (2009) 900-908.

[102] J.G. Sevillano, P. Vanhoutte and E. Aernoudt, Large Strain Work-Hardening and Textures, Progress in Materials Science 25 (1980) 71-412.

[103] M.H. Zhao, R. Fu, D. Lu and T.Y. Zhang, Critical thickness for cracking of Pb(Zr0.53Ti0.47)O3 thin films deposited on Pt/Ti/Si(100) substrates, Acta Materialia 50 (2002) 4241-4254.

[104] M. Stratmann, A. Leng, W. Fürbeth, H. Streckel, H. Gehmecker and K.H. GrosseBrinkhaus, The scanning Kelvin probe; A new technique for the in situ analysis of the delamination of organic coatings, Progress in Organic Coatings 27 (1996) 261-267.

[105] K. Ogle, S. Morel and N. Meddahi, An electrochemical study of the delamination of polymer coatings on galvanized steel, Corrosion Science 47 (2005) 2034-2052.

[106] K. Wapner, M. Stratmann and G. Grundmeier, In situ infrared spectroscopic and scanning Kelvin probe measurements of water and ion transport at polymer/metal interfaces, Electrochimica Acta 51 (2006) 3303-3315.

[107] G. Grundmeier, K.-M. Jüttner and M. Stratmann, *Novel Electrochemical Techniques in Corrosion Research*. Materials Science and Technologies, ed. R.W. Cahn, P. Haasen, and E.J. Kramer. 2000, Weinheim: Wiley-VCH. 285–381.

[108] R. Hausbrand, M. Stratmann and M. Rohwerder, Delamination resistant zinc alloys: Simple concept and results on the system zinc-magnesium, Steel Research International 74 (2003) 453-458.

# 10 Publications related to this work

**Peer-reviewed articles:**

G. Grundmeier, M. Giza and T. Titz, Analysis of corrosion resistant plasma polymer films on metals, Vakuum in Forschung und Praxis 18 (2006) 32–36.

R. Posner, T. Titz, K. Wapner, M. Stratmann and G. Grundmeier, Transport processes of hydrated ions at polymer/oxide/metal interfaces: Part 2. Transport on oxide covered iron and zinc surfaces, Electrochimica Acta 54 (2009) 900-908.

T. Titz, F. Hörzenberger, K. Van den Bergh and G. Grundmeier, Correlation of interfacial electrode potential and corrosion resistance of plasma polymer coated galvanised steel. Part 1: Ultra-thin plasma polymer films of varying thickness, Corrosion Science 52 (2010) 369–377.

T. Titz, F. Hörzenberger, K. Van den Bergh and G. Grundmeier, Correlation of interfacial electrode potential and corrosion resistance of plasma polymer coated galvanised steel. Part 2: Influence of forming induced defects, Corrosion Science 52 (2010) 378–386.

**Conference presentations:**

T. Titz, K. Wapner, and G. Grundmeier, Structure and properties of ultra-thin $SiO_2$ plasma polymer films at polymer/metal interfaces, $11^{th}$ European Conference on Applications of Surface and Interface Analysis, Vienna, Austria, (2005).

T. Titz, K. Wapner, and G. Grundmeier, Structure and properties of ultra-thin $SiO_2$ plasma polymer films at polymer/metal interfaces, American Vacuum Society 53rd International Symposium, San Francisco, USA, (2006).

T. Titz and G. Grundmeier, Correlation of structure and corrosion resistance of ultra-thin $SiO_2$ plasma polymer films at polymer/metal interfaces, 13. Bundesdeutsche Fachtagung Plasmatechnologie, Bochum, Germany, (2007).

T. Titz, M. Giza and G. Grundmeier, Modification of Passive Films on Metals in Vacuum and Atmospheric Pressure Plasmas, 16th International Colloquium on Plasma Processes, Toulouse, France, (2007).

**Poster presentations:**

T. Titz, K. Wapner and G. Grundmeier, Struktur und Eigenschaften ultradünner $SiO_2$-Plasmapolymer Schichten an Polymer/Metall-Grenzflächen, 12. Bundesdeutsche Fachtagung Plasmatechnologie, Braunschweig, Germany, (2005).

M. Giza, T. Titz and G. Grundmeier, Modification of passive layers on ZnMg-alloys by means of oxidising and reducing plasmas, Deutsche Physikalische Gesellschaft: Plasmaphysik, Augsburg, (2006).

T. Titz and G. Grundmeier, Correlation of structure and corrosion resistance of ultra-thin $SiO_2$ plasma polymer films at polymer/metal interfaces, 12th European Conference on Applications of Surface and Interface Analysis, Brussels, Belgium, (2007).